WEIZMANN
INSTITUTE
OF SCIENCE
Rehovot, Israel

מכון
ויצמן
למדע

Dynamics and predictability of ENSO

a study using a hybrid-coupled model and the adjoint method

Thesis for the degree

Doctor of Philosophy

by

Eli Galanti

September 2002

submitted to the Scientific Council of the Weizmann Institute of Science

WEIZMANN
INSTITUTE
OF SCIENCE
Rehovot, Israel

מכון
ויצמן
למדע

דינמיקה וחיזוי של אל-ניניו

מחקר באמצעות מודל אוקיאני-אטמוספרי מצומד

חבור לשם קבלת התואר

דוקטור לפילוסופיה

מאת

אלי גלנטי

תשרי תשס"ג

מוגש למועצה המדעית של מכון ויצמן למדע

רחובות, ישראל

Abstract

One of the major causes of natural global climate variability is the El Niño Southern Oscillation (ENSO) phenomenon. During the last two decades, scientists have made major steps toward an understanding of the physical mechanism behind ENSO, and in developing prediction systems, some of which are being used operationally for forecasting ENSO. Nevertheless, there are still some major issues concerning the dynamics of ENSO, as well as the ability to predict ENSO, that remain unresolved. In this study I apply the adjoint method of sensitivity studies and data assimilation to a hybrid coupled model of the Indo-Pacific, in order to get new insights into the dynamics of ENSO, and in order to make the first steps toward developing a new ENSO prediction model.

In the first part of the thesis, I investigate the physical mechanism underlying ENSO's phase locking to the seasonal cycle within the framework of a simple ordinary differential equation (ODE) model. I study the locking mechanism in three ENSO parameter regimes: the fast SST limit, the fast wave limit, and the mixed SST - wave dynamics regime. I find that in all three parameter regimes, the seasonal variations in the ocean-atmosphere coupling strength force the events to peak toward the end of the calendar year. The phase locking mechanism in the mixed mode and fast SST regimes relies on the seasonal excitation of the Kelvin and the Rossby waves by wind stress anomalies in the central Pacific basin. The peak time of the events is set by the dynamics to allow a balance between the warming and cooling trends due to downwelling Kelvin and upwelling Rossby waves. This balance is obtained because the warming trend due to the large amplitude Kelvin waves, amplified by a weak northern hemisphere winter-time ocean-atmosphere coupling strength, balances the cooling trend due to weak Rossby waves, amplified by a strong summer-time coupling strength. The difference between the locking mechanisms in the mixed mode regime and in the fast SST regime is used to understand the effect of the SST adjustment time on the timing of the phase locking. Finally, in the less realistic fast wave regime, a different physical mechanism for ENSO's phase locking is revealed through the SST adjustment time and the interaction between the east Pacific and the central Pacific.

In the second part I use the adjoint method for sensitivity studies to again analyze the stability of the coupled instability in the hybrid coupled model. I find that the seasonal changes in the ocean-atmosphere instability strength in this model are significantly affected by the seasonal outcropping of the thermocline in the east equatorial Pacific. From summer to early autumn, when the thermocline outcrops over a wide area in the East Pacific, there is a strong surface-thermocline connection and anomalies that arrive as Kelvin waves from the west along the thermocline can reach the surface and affect the SST and thus the coupled system. Conversely, from late winter to early spring, when the thermocline outcropping is minimal, the surface de-couples from the thermocline and temperature anomalies in the thermocline depth range do not affect the surface and dissipate within the thermocline. It is therefore suggested that the seasonal ocean-atmosphere instability strength in the equatorial Pacific is strongly influenced by the thermocline outcropping and its seasonal modulation, a physical mechanism that can be represented properly only in models that employ the full dynamics of the mixed-layer as well as resolve the thermocline itself and its seasonal motions.

The possibility of generating decadal ENSO variability via an ocean teleconnection to the mid-latitude Pacific is studied in the third part of the thesis. This is done by analyzing the sensitivity of the equatorial stratification to mid-latitude processes using an ocean GCM, the adjoint method, and a QG normal mode stability analysis. It is found that, on time scales of 2 to 15 years, the equatorial Pacific is most sensitive to mid-latitude planetary Rossby waves traveling from the mid-latitudes toward the western boundary and then to the equator. Those waves that propagate through baroclinically unstable parts of the sub-tropical gyre are amplified by the baroclinic instability, and therefore dominate the mid-latitude signal arriving at the equator. This implies that decadal variability in the mid-latitude Pacific would be efficiently transmitted to the equatorial Pacific from specific areas of the mid-latitude pacific, that are baroclinically unstable, such as the near-equatorial edges of the sub-tropical gyres (15°N and 12°S). The Rossby waves that propagate via the baroclinically unstable areas are of the advective mode type which follow the gyre circulation to some degree, and arrive from as far as 25°N and 30°S in the east Pacific. It is shown that the baroclinic instability involves critical layers due to the vertical shear of the sub-tropical gyre circulation, at depths of 150-200 meters.

The forth part of the thesis is devoted to the development of an experimental ENSO prediction system, based on an ocean GCM coupled to a statistical atmosphere, and the adjoint method of 4D variational data assimilation. The adjoint method is used to initialize the coupled model, and predictions are performed for the period of 1980 to 1999. The coupled model is also initialized using two simpler assimilation techniques: forcing the ocean model with observed SST and surface fluxes, and a 3D variational assimilation method, similar to that used by NCEP for operational ENSO prediction. The prediction skill of the coupled model initialized by the three assimilation methods is then analyzed and compared. The effect of the assimilation period used in the adjoint method is studied by using 3,6 and 9 months assimilation periods. Finally, the possibility of assimilating only the anomalies with respect to observed climatology, in order to circumvent systematic model biases is examined. I find that the adjoint method outperforms the other assimilation schemes, leading to the hope that it may provide an alternative operational prediction approach once tested and proved superior also in higher resolution models.

Acknowledgment

During the last 6 years I had to honor of studying and researching under the wonderful guidance of Prof. Eli Tziperman. Eli is not only an outstanding scientist, but even more important, a caring and loving human being who was always there to lift up my spirit during difficult times. Thank you Eli.

I would like to thank Matt Harrison and Tony Rosati from GFDL, with whom I collaborated, for their help and guidance throughout the research. Thanks also to Ralf Giering who provided the powerful adjoint compiler tool and optimization scheme, and Ziv Sirkes who helped with generating the adjoint code and setting up the data assimilation scheme. I also thank Ron Pacanowski and Steve Griffies from GFDL, for providing the pre-alpha version of MOM4 and helping with the adjoint code generation.

I thank the members of the department of Environmental Sciences at the Weizmann Institute, students, faculty, and administrative stuff, for creating a pleasant and supporting working environment.

Finally, I would like to thank my parents, Yehuda and Yehudit, who raised me to be honest, modest, and open minded, and to wife Shlomit who is the reason for everything I do.

Table of Contents:

Chapter 1:
Thesis introduction

1. Forward

Much progress has been made in the past decade both in developing a variety of models for El Niño-Southern Oscillation (ENSO) studies (Neelin et al. 1998), and in the development of data assimilation methods for the initialization of ENSO predictions (Latif et al. 1998). Still, there are some basic characteristics of ENSO that are not fully understood, such as its tendency to peak toward the end of the year, the mechanisms governing the Pacific ocean-atmosphere instability strength, and the decadal variability ENSO exhibits. Furthermore, our ability to predict El Niño is less than satisfactory, and a reliable prediction for about a year in advance, as needed by the affected countries, is yet out of reach. In this thesis, I address some questions regarding the dynamics of ENSO, and make the first step toward the building of new prediction model that is based on a sophisticated data assimilation technique applied to a coupled ocean-atmosphere model.

This chapter begins with a review of the relevant scientific background, and then the main goals of the thesis and the main findings and conclusions are presented.

2. Scientific Background

The second strongest climate variability signal after the seasonal cycle is the El Niño Southern Oscillation (ENSO) phenomenon (Philander 1990). ENSO refers to the interannual variability (Fig. 1) of the ocean and atmosphere system, mainly in the tropical Pacific region. It is characterized mainly by the irregularity of the events (Fig. 1), and by a partial locking to the seasonal cycle (Fig. 2). ENSO-related atmospheric teleconnections affect weather and climate worldwide. Therefore, a clearly important scientific and practical goal is to understand the dynamics and predictability limits of ENSO.

The major factor determining the strength and extent of ENSO events, is the instability state of the equatorial Pacific coupled ocean-atmosphere system. An unstable state enhances the growth of anomalous conditions that can then evolve to become an El Niño event.

The instability strength in the equatorial Pacific region undergoes seasonal variations (e.g. Battisti and Hirst 1989; Hirst 1986; Philander 1983), along with variations whose time scale ranges from a few years to decades (e.g. Gu and Philander 1995, 1997). Understanding the physical factors determining the strength and seasonal variability of the coupled instability is an important task because it has implications for both El Nino's predictability (Chen et al. 1995; Moore and Kleeman 1996; Torrence and Webster 1998; Webster and Yang 1992; Weiss and Weiss 1999; Xue et al. 1994), as well as for ENSO's irregularity (Chang et al. 1994; Jin et al. 1994; Tziperman et al. 1994, 1995) and phase locking (Galanti and Tziperman 2000; Tziperman et al. 1998).

Philander (1983) suggested that the key element determining the seasonality of the coupled instability strength is the seasonal movement of the Pacific Inter Tropical Convergence Zone (ITCZ) and its effect on the atmospheric heating. Other seasonal climatological factors that might enhance the coupled ocean-atmosphere instability are large zonal gradients of mean SST, shallow thermocline, strong zonal winds, high SST (Hirst 1986) and strong upwelling (Battisti 1988). Battisti and Hirst (1989) found that setting the basic state in a simplified model to different monthly climatologies affects the rate of anomaly growth. Analyzing separately the effect of each seasonal variable in an intermediate model, Tziperman et al. (1997) suggested that the seasonal wind convergence (i.e. the ITCZ location) and the seasonal climatological SST are the dominant factors in determining the strength of the ocean-atmosphere instability in the Cane-Zebiak model (Zebiak and Cane 1987). All the above works used simplified models, ranging from low-order models to intermediate ones such as the CZ-model, which all lack the ability to explicitly resolve the mixed layer and the thermocline structure.

In chapter 3 (Galanti et al. 2002a), I show that the seasonal outcropping of the east Pacific thermocline plays an important role in setting the seasonality of the coupled ocean-atmosphere instability.

One of the predominant characteristics of ENSO is its tendency to peak towards the end of the calendar year (Rasmusson and Carpenter 1982). The East Pacific basin-wide warming anomaly (with respect to the monthly mean state) in most recorded events reaches its maximum within the months November-January (Fig. 2). Although the above works, dealing with the instability strength, point at possible seasonal climatological variables that affect El Niño's development and dynamics, they do not explain the specific physical mechanism by which the seasonal cycle causes El Niño to peak towards the end of the calendar year. Tziperman et al. (1998) examined this mechanism in a heuristic delayed oscil-

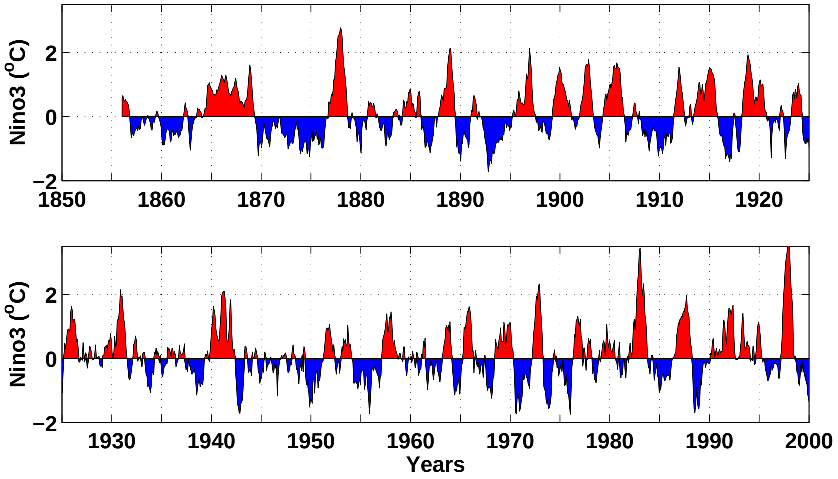

FIG. 1. Anomalous sea surface temperature averaged over the equatorial east Pacific (Nino3). El Niño events are shaded in red, and La Niña events are shaded in blue.

lator model (Battisti 1988; Cane et al. 1990; Munnich et al. 1991; Suarez and Schopf 1988) and suggested that the locking may be explained by a seasonal amplification of Kelvin and Rossby waves by wind stress anomalies in the central Pacific basin. The peak time of the events was proposed to be set by the dynamics to allow a balance between the warming and cooling trends due to downwelling Kelvin and upwelling Rossby waves. This balance is obtained because the warming trend due to the large amplitude Kelvin waves, amplified by a weak ocean-atmosphere coupling at boreal winter, balances the cooling trend due to weak Rossby waves, amplified by a strong boreal summer-time coupling. However, while heuristic idealized models such as that of T98 can be quite illuminating, it is both necessary and possible to use more rigorously derived idealized models at different parameter regimes, that are still simple enough to allow exploring the physical mechanisms of ENSO's phase locking.

In chapter 2 (Galanti and Tziperman 2000), I examine the physical mechanism leading to ENSO's phase locking to the seasonal cycle in more rigorously derived simple ENSO models. I examine this issue in the 3 main ENSO parameter regimes: the fast wave regime, fast SST regime, and mixed mode regime (Jin and Neelin 1993a, b; Neelin and Jin 1993).

Another important characteristic of ENSO is its decadal variability (Fig. 1). This characteristic of ENSO has been a subject of quite a few studies during the past decade (e.g. An and Wang 2000; Trenberth and Hurrell 1994). Because typical time scales at the equator are relatively short, a strong candidate for this equatorial decadal variability is the slower mid-latitude ocean which somehow affects the equatorial ocean (e.g. Gu and Philander 1997; Jin 2001; Kleeman et al. 1999). Gu and Philander (1997) suggested that the decadal variability in the Equatorial Pacific is a result of surface mid-latitude water sinking along isopycnals toward the central Pacific equatorial thermocline base, where it upwells to the surface to affect the SST. The warmer SST, in turn, aside from changing the characteristics of ENSO (strength, period, etc.) also affects the mid-latitude westerlies through the tropics-extratropics temperature gradient. The stronger westerlies in the mid-latitudes enhance evaporative cooling, and create colder water that sinks and is advected toward the equator by the ocean general circulation, to later cool the SST there. The result is an interdecadal oscillation with an amplitude of about $1°C$ SST anomaly.

This scenario was modified in various ways by other studies. Some focused on pure oceanic pathways between the mid-latitude and the equatorial region via long isopycnal advection (Harper 2000; Zhang et al. 2001) or via planetary waves that propagate from mid-latitudes to the tropics (Capotondi and Alexander 2001; Jin 2001; Lysne et al. 1997). Repeat hydrography observations show eddy motions that may perhaps be interpreted as planetary waves (e.g. Roemmich and Gilson 2001). Some other studies seemed to find that oceanic teleconnections are not efficient (Hazeleger et al. 2001), and others that the oceanic teleconnection is mostly active in the southern hemisphere (Schneider et al. 1999). An alternative atmospheric bridge via which atmospheric influence propagates to the tropics has also been suggested (Barnett et al. 1999). The influence of the trop-

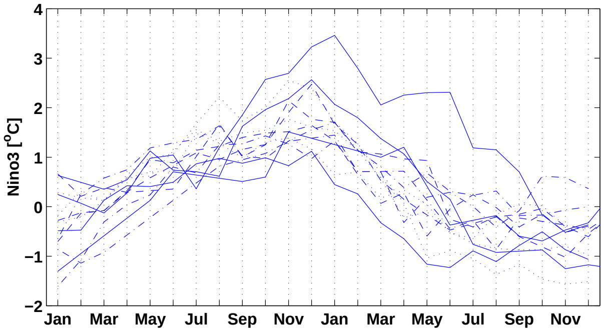

FIG. 2. Several El Niño events from Fig. 1 superimposed to show how most events reach their peak toward the end of the calendar year.

ical SST on the mid-latitude atmosphere is proposed by Kleeman et al. (1999) to be via effects on the subtropical gyre circulation rather than via evaporative cooling.

The question of what is the relative importance of the two oceanic teleconnection mechanisms (subduction vs. waves) in transferring decadal signals from the mid-latitudes to the equator, is still unanswered. Another unresolved issue in these works is what selects the particular mid-latitude areas from which Rossby waves arrive to influence the equatorial Pacific

In chapter 4 (Galanti and Tzipermann 2002), I show that the equatorial thermal structure is most sensitive to mid-latitude Rossby waves. Baroclinic instability at the south (north) edge of the northern (southern) hemisphere sub-tropical gyre, amplifies those Rossby waves that affect the tropical Pacific and selects the latitude from which the waves travel to the equator.

In addition to the goal of improving our understanding of ENSOs dynamics, it is clearly of great importance to try and predict future El Niño and La Niña events. The models used for studying ENSO prediction range from statistical models to coupled ocean-atmosphere general circulation models. Statistical models use as a predictor the ocean surface level pressure (Barnett 1983; Graham et al. 1987), the southern oscillation index of pressure differences between Darwin and Tahiti (Kepenne et al. 1992) or the heat content (Latif and Graham 1992; White et al. 1987). As a predictand, statistical models usually use a SST index such as NINO3. Intermediate coupled dynamical models such as the CZ-model rely on simplified ocean dynamics and a simple atmospheric model that is usually assumed to be in a steady state with the SST at any given time, thus assuming an immediate atmospheric equilibration. Next are the Hybrid coupled models, i.e. models that consist of an ocean intermediate model (Balmaseda et al. 1994; Graham et al. 1992) or a general circulation model coupled to a statistical atmospheric model (Barnett et al. 1993; Syu et al. 1995). At the top of the hierarchy are the coupled general circulation models (CGCM) which consist of an ocean GCM coupled to an atmospheric GCM. These models aim to capture most of the ocean-atmosphere dynamics and thermodynamics (Kirtman et al. 1997; Latif et al. 1993; Rosati et al. 1997).

Data assimilation methods used in tropical ocean models range from simple nudging techniques to sophisticated optimization methods like the Kalman filtering and the 4D variational schemes (Ghil and Malanotte-Rizzoli 1991). Earlier works (Moore et al. 1987) tried to investigate the potential of the assimilation of sparse data into oceanic models, and the relative importance of each assimilated field. Data insertion was used successfully in the CZ-model, for example, where the observed winds were used to drive the ocean model (Cane et al. 1986). Next is the nudging method, where the model fields are nudged towards the observed value with a time scale depending on the assumed model and data errors (Chen et al. 1995). Optimal Interpolation (3D variational assimilation) (Derber and Rosati 1989), is currently used operationally in NCEP (Behringer et al. 1998). Finally, there are the Kalman filter and smoother (Cane et al. 1996; Fukumori and Malanotte-Rizzoli 1995; Miller and Cane 1989), and the 4D variational assimilation technique (adjoint method) that avoids some of the computational difficulties by not calculating the error covariance matrices.

Adjoint models are now commonly used for the study of oceanic and atmospheric sensitivities to initial conditions and model parameters (Errico and Vukicevic 1992; Hall and Cacuci 1983; Van-Oldenborgh et al. 1999), as well as for 4D variational data assimilation method in intermediate and complex models (Bennett and McIntosh 1982; Bennett et al. 1998; Kleeman et al. 1995; Thacker and Long 1988; Tziperman and Thacker 1989). Another use of adjoint models is in calculating optimal growth structures (Chen et al. 1997; Farrell and Ioannou 1996; Moore and Kleeman 1996; Penland and Sardeshmukh 1995), in which the optimal structures, which arise due to the non-normality of the linearized dynamics, may be efficiently calculated using the tangent linear model and its adjoint.

As far as I am aware, the adjoint method of data assimilation has still not been applied to an ENSO prediction model based on an ocean GCM. Furthermore, most adjoint models have been constructed to either simple coupled models, or to ocean-only models. It is both natural and important to try and apply the adjoint method to a hybrid-coupled model based on a full ocean GCM, in order to make progress towards an ENSO prediction system based on such a state of the art model and data assimilation method. This is precisely the goal of chapter 5 (Galanti et al. 2002b), in which I explore the application of the adjoint method to the ENSO prediction problem.

3. Main goals of the research

The main goal of this study is to improve our understanding of both ENSO dynamics and predictability, using the tool of adjoint sensitivity studies and data assimilation, applied to a hybrid coupled model of the Indo-Pacific.

The first goal of this study is to apply the adjoint method for sensitivity studies to the investigation of ENSO dynamics, especially the seasonal nature of the ocean-atmosphere instability strength, and the possible influence of the Pacific Mid-latitude region on the Pacific equatorial thermal structure on decadal time scale.

The second goal of the study is to setup an experimental ENSO prediction system based on the hybrid-coupled model and the adjoint method of 4Dvar data assimilation, and to study its predictability characteristics.

These two goals required the very significant effort of building a hybrid-coupled model (combined from an ocean GCM coupled to a statistical atmosphere) of the Indo-Pacific region that will accurately simulate ENSO, together with its adjoint model that will be used for the study of both ENSO dynamics (sensitivity studies) and for 4Dvar data assimilation. The setting up of the model, adjoint, and data assimilation tools were therefore also a technical yet critical goal of this work.

4. Main findings and central conclusions

1. *ENSO phase locking to the seasonal cycle*- I explain how the seasonal variations in the ocean-atmosphere coupling strength force the ENSO events to peak toward the end of the calendar year. The phase locking mechanism relies on the seasonal excitation of the Kelvin and the Rossby waves by wind stress anomalies in the central Pacific basin, and is examined in carefully derived models of 3 ENSO parameter regimes: fast wave, fast SST, and mixed mode regimes (chapter 2, Galanti and Tziperman 2000).

2. *The east Pacific thermocline outcropping and ENSO*- The seasonal changes in the ocean-atmosphere instability strength are shown to be related to the outcropping of the thermocline in the east equatorial Pacific. From July to December, when the thermocline outcrops over a wide area in the East Pacific, there is a strong surface-thermocline connection and anomalies that arrive as Kelvin waves from the west along the thermocline can reach the surface and affect the SST and thus the coupled system. Conversely, from February to June, when the thermocline outcropping is minimal, the surface decouples from the thermocline and temperature anomalies in the thermocline depth range do not affect the surface and dissipate within the thermocline. The role of vertical mixing rather than upwelling in linking vertical thermocline movements to SST changes is emphasized. The above physical mechanism is often neglected in intermediate coupled models and that can be represented properly only in models that employ the full dynamics of the mixed-layer (chapter 3, Galanti et al. 2002a).

3. *A mid-latitude – ENSO teleconnection mechanism*- It is found that on time scales of 2 to 15 years, the thermocline structure in the equatorial East Pacific is most sensitive to mid-latitude long Rossby waves that originate from latitudes 25°N and 30°S in the east Pacific, travel westward mostly along 15°N and 12°S, and affect the equatorial temperature structure by initiating equatorial Kelvin and Rossby waves. It is shown that these waves are amplified along their path by baroclinic instability that involves critical layers at depths of 150-200 meters Galanti and Tzipermann (chapter 4, 2002).

4. *ENSO prediction based on adjoint initialization*- An experimental ENSO prediction system is presented, based on an ocean GCM coupled to a statistical atmosphere, and the adjoint method of 4D variational data assimilation. The adjoint method is used to initialize the coupled model and predictions are performed for the period of 1980 to 1999. The adjoint method is found to have the potential to improve upon presently used assimilation techniques (chapter 5, Galanti et al. 2002b).

REFERENCES

An, S. I., and B. Wang, 2000: Interdecadal change of the structure of the enso mode and its impact on the enso frequency. *Journal of Climate*, **13**(12), 2044–2055.

Balmaseda, M. A., D. L. T. Anderson, and M. K. Davey, 1994: ENSO prediction using a dynamical ocean model coupled to statistical atmospheres. *Tellus*, **46A**(4), 497–511.

Barnett, T., D. Pierce, M. Latif, D. Dommenget, and R. Saravanan, 1999: Interdecadal interactions between the tropics and midlatitudes in the pacific basin. *GRL*, **26**(5), 615–618.

Barnett, T. P., 1983: Interaction of the monsoon and Pacific trade wind system at interannual time scales. 1: The equatorial zone. *Mon. Weath. Rev.*, **111**, 756–773.

Barnett, T. P., M. Latif, N. Graham, M. Flugel, S. Pazan, and W. White, 1993: ENSO and ENSO related predictability, i, prediction of equatorial pacific sea surface temperature with a hybrid coupled ocean atmosphere model. *J. Climate*, **6**, 1545–1566.

Battisti, D. S., 1988: The dynamics and thermodynamics of a warming event in a coupled tropical atmosphere/ocean model. *J. Atmos. Sci.*, **45**, 2889–2919.

Battisti, D. S., and A. C. Hirst, 1989: Interannual variability in the tropical atmosphere-ocean system: Influence of the basic state and ocean geometry. *J. Atmos. Sci.*, **45**, 1687–1712.

Behringer, D. W., M. Ji, and A. Leetmaa, 1998: An improved coupled model for enso prediction and implications for ocean initialization. part i: The ocean data assimilation system. *Monthly Weather Review*, **126**(4), 1013–1021.

Bennett, A. F., and P. C. McIntosh, 1982: Open ocean modelling as an inverse problem: tidal theory. *J. Phys. Oceanogr.*, **12**, 1004–1018.

Bennett, A. F., B. S. Chua, D. E. Harrison, and M. J. McPhaden, 1998: Generalized inversion of tropical atmosphere-ocean data and a coupled model of the tropical Pacific. *J. Climate*, **11**, 1768–1792.

Cane, M. A., S. E. Zebiak, and S. C. Dolan, 1986: Experimental forecasts of El Niño. *Nature*, **321**, 827–832.

Cane, M. A., M. Münnich, and S. E. Zebiak, 1990: A Study of Self-Excited Oscillations of the Tropical Ocean-Atmosphere System. Part I: Linear Analysis. *J. Atmos. Sci.*, **47**(13), 1562–1577.

Cane, M. A., A. Kaplan, R. N. Miller, B. Tang, E. Hackert, and A. J. Busalacchi, 1996: Mapping tropical Pacific sea level: Data assimilation via a reduced state space kalman filter. *J. Geophys. Res.*, **101**, 22,599–22,617.

Capotondi, A., and M. A. Alexander, 2001: Rossby waves in the tropical north pacific and their role in decadal thermocline variability. *Journal of Physical Oceanography*, **31**(12), 3496–3515.

Chang, P., B. Wang, T. Li, and L. Ji, 1994: Interactions between the seasonal cycle and the southern oscillation — frequency entrainment and chaos in a coupled ocean-atmosphere model. *Geophys. Res. Lett.*, **21**, 2817–2820.

Chen, D., S. E. Zebiak, A. J. Busalacchi, and M. A. Cane, 1995: An improved procedure for El Niño forecasting: Implications for predictability. *Science*, **269**, 1699–1702.

Chen, Y. Q., D. S. Battisti, T. N. Palmer, J. Barsugli, and E. S. Sarachik, 1997: Study of the predictability of tropical Pacific sst in a coupled atmosphere-ocean model using singular vector analysis: The role of the annual cycle and the ENSO cycle. *Mon. Weath. Rev.*, **125**(5), 831–845.

Derber, J., and A. Rosati, 1989: A global oceanic data assimilation system. *J. Phys. Oceanogr.*, **19**, 1333–1347.

Errico, R. M., and T. Vukicevic, 1992: Sensitivity analysis using an adjoint of the psu-ncar mesoscale model. *Mon. Weath. Rev.*, **120**, 1644–1660.

Farrell, B. F., and P. J. Ioannou, 1996: Generalized stability theory part i: autonomous operators. *J. Atmos. Sci.*, **53**, 2025–2040.

Fukumori, I., and P. Malanotte-Rizzoli, 1995: An approximate Kalman Filter for ocean data assimilation: an example with an idealized Gulf-Stream model. *Journal of Geophysical Research-oceans*, **100**(C4), 6777–6793.

Galanti, E., and E. Tziperman, 2000: ENSO's phase locking to the seasonal cycle in the fast sst, fast wave, and mixed mode regimes. *J. Atmos. Sci.*, **57**, 2936–2950.

Galanti, E., and E. Tzipermann, 2002: A mid-latitude enso teleconnection mechanism via long rossby waves. *J. Phys. Oceanogr.*. Submitted.

Galanti, E., E. Tziperman, M. Harrison, A. Rosati, R. Giering, and Z. Sirkes, 2002a: The equatorial thermocline outcropping - a seasonal control on the tropical Pacific ocean-atmosphere instability strength. *J. Climate*, **15**(19), 2721–2739.

Galanti, E., E. Tziperman, M. Harrison, A. Rosati, and Z. Sirkes, 2002b: A study of enso prediction using a hybrid-coupled model and the adjoint method for data assimilation. *Mon. Weath. Rev.*. Submitted.

Ghil, M., and P. Malanotte-Rizzoli, 1991: Data assimilation in meteorology and oceanography. *Advances in Geophysics*, **33**, 141–266.

Graham, N. E., J. Michaelson, , and T. P. Barnett, 1987: The investigation of the El Niño-southern oscillation cycle with statistical models, i, precursor field characteristics. *J. Geophys. Res.*, **92**, 14,251–14,270.

Graham, N. E., T. P. Barnett, and M. Latif, 1992: Considerations of the predictability of ENSO with a low-order coupled model. *TOGA notes*, **7**, 11–15.

Gu, D., and S. Philander, 1995: Secular changes of annual and interannual variability in the tropics during the past century. *J. Climate*, **8**(4), 864–876.

Gu, D., and S. G. H. Philander, 1997: Interdecadal climate fluctuations that depend on exchanges between the tropics and extratropics. *Science*, **275**(7), 805–807.

Hall, M. C. B., and D. G. Cacuci, 1983: Physical interpretation of the adjoint functions for sensitivity analysis of atmospheric models. *J. Atmos. Sci.*, **40**, 2537–2546.

Harper, S., 2000: Thermocline ventilation and pathways of tropical-subtropical water mass exchange. *Tellus*, **52A**(3), 330–345.

Hazeleger, W., M. Visbeck, M. Cane, A. Karspeck, and N. Naik, 2001: Decadal upper ocean temperature variability in the tropical pacific. *Journal of Geophysical Research-oceans*, **106**(C5), 8971–8988.

Hirst, A. C., 1986: Unstable and damped equatorial modes in simple coupled ocean-atmosphere models. *J. Atmos. Sci.*, **43**, 606–630.

Jin, F. F., 2001: Low-frequency modes of tropical ocean dynamics. *Journal of Climate*, **14**(18), 3874–3881.

Jin, F.-F., and D. Neelin, 1993a: Models of interannual tropical ocean-atmosphere interaction - a unified view. part i: numerical results. *J. Atmos. Sci.*, **50**, 3477–3503.

Jin, F.-F., and D. Neelin, 1993b: Models of interannual tropical ocean-atmosphere interaction - a unified view. part iii: analytical results in fully coupled cases. *J. Atmos. Sci.*, **50**, 3523–3540.

Jin, F.-F., D. Neelin, and M. Ghil, 1994: ENSO on the devil's staircase. *Science*, **264**, 70–72.

Kepenne, C. L., , and M. Ghil, 1992: Adaptive filtering and the southern oscillation index. *J. Geophys. Res.*, **97**, 20,449–20,454.

Kirtman, B. P., J. Shukla, B. Huang, Z. Zhu, and E. K. Schneider, 1997: Multiseasonal predictions with a coupled tropical ocean/global atmosphere system. *Mon. Weath. Rev.*, **125**, 789–808.

Kleeman, R., A. M. Moore, and N. R. Smith, 1995: Assimilation of subsurface thermal data into an intermediate tropical coupled ocean-atmosphere model. *Mon. Weath. Rev.*, **123**, 3103–3113.

Kleeman, R., J. P. Mccreary, and B. A. Klinger, 1999: A mechanism for generating enso decadal variability. *Geophysical Research Letters*, **26**(12), 1743–1746.

Latif, M., and N. E. Graham, 1992: How much predictive skill is obtained in the thermal structure of an ogcm? *J. Phys. Oceanogr.*, **22**, 951–962.

Latif, M., A. Sterl, E. Maier-Reimer, and M. M. Junge, 1993: Structure and predictability of the El Niño/southern oscillation phenomenon in a coupled ocean-atmosphere general circulation model. *J. Climate*, **6**, 700–708.

Latif, M., et al., 1998: A review of the predictability and prediction of ENSO. *J. Geophys. Res.*, **103**(C7), 14,375–14,393.

Lysne, J., P. Chang, and B. Giese, 1997: Impact of the extratropical pacific on equatorial variability. *Geophysical Research Letters*, **24**(21), 2589–2592.

Miller, R. N., and M. A. Cane, 1989: A Kalman filter analysis of sea level heights in the Tropical Pacific. *J. Phys. Oceanogr.*, **19**, 773–790.

Moore, A. M., and R. Kleeman, 1996: The dynamics of error growth and predictability in a coupled model of ENSO. *Q. J. R. Meteor. Soc.*, **122**, 1405–1446.

Moore, A. M., N. S. Cooper, and D. Anderson, 1987: Data assimilation in models of the Indian Ocean. *J. Phys. Oceanogr.*, **17**, 1965–1977.

Munnich, M., M. A. Cane, and S. E. Zebiak, 1991: A study of self-excited oscillations of the tropical ocean-atmosphere system. *J. Atmos. Sci.*, **48**, 1238–1248.

Neelin, J. D., and F.-F. Jin, 1993: Models of interannual tropical ocean-atmosphere interaction - a unified view. part ii: analytical results in the weak-coupling limit. *J. Atmos. Sci.*, **50**, 3504–3522.

Neelin, J. D., D. S. Battisti, A. C. Hirst, F.-F. Jin, Y. Wakata, T. Yamagata, and S. Zebiak, 1998: ENSO theory. *Special Joint issue of J. Geophys. Res. Atmospheres and J. Geophys. Res. Oceans*, **103**(C7), 14,261–14,290.

Penland, C., and P. D. Sardeshmukh, 1995: The optimal-growth of tropical sea-surface temperature anomalies. *J. Climate*, **8**(8), 1999–2024.

Philander, S. G., 1983: El Niño southern oscillation phenomena. *Nature*, **302**, 295–301.

Philander, S. G. H., 1990: *El Niño, La Niña, and the Southern Oscillation.*. Academic Press.

Rasmusson, E. M., and T. H. Carpenter, 1982: Variations in tropical sea surface temperature and surface wind fields associated with the Southern Oscillation/El Niño. *Mon. Weath. Rev.*, **110**, 354–384.

Roemmich, D., and J. Gilson, 2001: Eddy transport of heat and thermocline waters in the north pacific: A key to interannual/decadal climate variability? *Journal of Physical Oceanography*, **31**(3), 675–687.

Rosati, A., K. Miyakoda, and R. Gudgel, 1997: The impact of ocean initial conditions on ENSO forecasting with a coupled model. *Mon. Weath. Rev.*, **125**, 752–772.

Schneider, N., S. Venzke, A. J. Miller, D. W. Pierce, T. P. Barnett, C. Deser, and M. Latif, 1999: Pacific thermocline bridge revisited. *Geophysical Research Letters*, **26**(9), 1329–1332.

Suarez, M. J., and P. S. Schopf, 1988: A delayed action oscillator for ENSO. *J. Atmos. Sci.*, **45**, 3283–7.

Syu, H.-H., J. Neelin, and D. Gutzler, 1995: Seasonal and interannual variability in a hybrid coupled gcm. *J. Climate*, **8**, 2121–2143.

Thacker, W. C., and R. B. Long, 1988: Fitting dynamics to data. *J. Geophys. Res.*, **93**, 1227–1240.

Torrence, C., and P. J. Webster, 1998: The annual cycle of persistence in the El Nino southern oscillation. *Q. J. R. Meteorol. Soc.*, **124**(550), 1985–2004.

Trenberth, K. E., and J. W. Hurrell, 1994: Decadal atmosphere-ocean variations in the Pacific. *Climate Dynamics*, **9**(6), 303–319.

Tziperman, E., and W. C. Thacker, 1989: An optimal-control adjoint-equations approach to studying the oceanic general-circulation. *J. Phys. Oceanogr.*, **19**(10), 1471–1485.

Tziperman, E., L. Stone, M. A. Cane, and H. Jarosh, 1994: El-nino chaos: Overlapping of resonances between the seasonal cycle and the pacific ocean-atmosphere oscillator. *Science*, **264**(5155), 72–74.

Tziperman, E., M. A. Cane, and S. E. Zebiak, 1995: Irregularity and locking to the seasonal cycle in an ENSO prediction model as explained by the quasi-periodicity route to chaos. *J. Atmos. Sci.*, **52**(3), 293–306.

Tziperman, E., S. E. Zebiak, and M. A. Cane, 1997: Mechanisms of seasonal: ENSO interaction. *J. Atmos. Sci.*, **54**(1), 61–71.

Tziperman, E., M. A. Cane, S. E. Zebiak, Y. Xue, and B. Blumenthal, 1998: Locking of El Nino's peak time to the end of the calendar year in the delayed oscillator picture of ENSO. *J. Climate*, **11**(9), 2191–2199.

Van-Oldenborgh, G. J., G. Burgers, S. Venzke, C. Eckert, and R. Giering, 1999: Tracking down the ENSO delayed oscillator with an adjoint ogcm. *Mon. Weath. Rev.*, **127**(7), 1477–1495.

Webster, P. J., and S. Yang, 1992: Monsoon and enso: Selectively interactive systems. *Q. J. R. Meteorol. Soc.*, **118**(507), 877–926.

Weiss, J. P., and J. B. Weiss, 1999: Quantifying persistence in ENSO. *J. Atmos. Sci.*, **56**(16), 2737–2760.

White, W. B., S. E. Pazan, and M. Inoue, 1987: Hindcast/forecasts of ENSO events based upon the redistribution of observed and model heat content in the western tropical Pacific, 1964-1986. *J. Phys. Oceanogr.*, **17**, 264–280.

Xue, Y., M. A. Cane, S. E. Zebiak, and M. B. Blumenthal, 1994: On the prediction of ENSO: a study with a low order Markov model. *Tellus*, **46A**, 512–528.

Zebiak, S. E., and M. A. Cane, 1987: A model El Niño-Southern Oscillation. *Mon. Weath. Rev.*, **115**, 2262–2278.

Zhang, R. H., T. Kagimoto, and S. E. Zebiak, 2001: Subduction of decadal north pacific thermal anomalies in an ocean gcm. *Geophysical Research Letters*, **28**(12), 2449–2452.

Chapter 2:
ENSO's phase locking to the seasonal cycle in the fast SST, fast wave, and mixed mode regimes

ELI GALANTI AND ELI TZIPERMAN

Environmental Sciences, Weizmann Institute, Rehovot 76100, Israel

ABSTRACT

The physical mechanism underlying ENSO's phase locking to the seasonal cycle is examined in three parameter regimes: the fast SST limit, the fast wave limit, and the mixed SST - wave dynamics regime. The seasonal cycle is imposed on simple ordinary differential equation (ODE) models for each physical regime as either a seasonal ocean-atmosphere coupling strength obtained from the CZ-model, or as a climatological seasonal upwelling. In all three parameter regimes, the seasonal variations in the ocean-atmosphere coupling strength force the events to peak toward the end of the calendar year, whereas the effect of upwelling is shown to be less important. The phase locking mechanism in the mixed mode and fast SST regimes relies on the seasonal excitation of the Kelvin and the Rossby waves by wind stress anomalies in the central Pacific basin. The peak time of the events is set by the dynamics to allow a balance between the warming and cooling trends due to downwelling Kelvin and upwelling Rossby waves. This balance is obtained because the warming trend due to the large amplitude Kelvin waves, amplified by a weak northern hemisphere winter-time ocean-atmosphere coupling strength, balances the cooling trend due to weak Rossby waves, amplified by a strong summer-time coupling strength. The difference between the locking mechanisms in the mixed mode regime and in the fast SST regime is used to understand the effect of the SST adjustment time on the timing of the phase locking. Finally, in the less realistic fast wave regime, a different physical mechanism for ENSO's phase locking is revealed through the SST adjustment time and the interaction between the east Pacific region and the central Pacific region.

1. Introduction

One of the predominant characteristics of ENSO is its tendency to peak towards the end of the calendar year (Rasmusson and Carpenter 1982). The East Pacific basin-wide warming anomaly (with respect to the monthly mean state) in most recorded events reaches its maximum within the months November-January (see Fig. 1 of Tziperman et al. (1998), hereafter T98). Philander (1983) suggested that the key element in the dynamics of the interaction between El Niño and the seasonal cycle is the seasonal movement of the Pacific Inter Tropical Convergence Zone (ITCZ) and its effect on the atmospheric heating and hence on the coupled ocean-atmosphere instability. Other seasonal climatological factors that might enhance the coupled ocean-atmosphere instability possibly leading to ENSO events, are large zonal gradients of mean SST, shallow thermocline, strong zonal winds, high SST (Hirst 1986), and strong upwelling (Battisti 1988). Battisti and Hirst (1989) found that setting the basic state in a simplified model to different monthly climatologies affects the rate of anomaly growth. The effects of the above seasonal factors on ENSO's dynamics and phase locking was also attributed to a non-linear resonance between a nonlinear ENSO oscillator and the periodic seasonal forcing (Chang et al. 1995; Jin et al. 1994; Tziperman et al. 1994, 1995).

Although the above works point at possible seasonal climatological variables that affect El Niño's development and dynamics, they do not explain the specific physical mechanism by which the seasonal cycle causes El Niño to peak towards the end of the calendar year. T98 examined this mechanism in a heuristic delayed oscillator model (Battisti 1988; Cane et al. 1990; Munnich et al. 1991; Suarez and Schopf 1988) and suggested that the locking may be explained by a seasonal amplification of Kelvin and Rossby waves by wind stress anomalies in the central Pacific basin. The peak time of the events was proposed to be set by the dynamics to allow a balance between the warming and cooling trends due to downwelling Kelvin and upwelling Rossby waves. This balance is obtained because the warming trend due to the large amplitude Kelvin waves, amplified by a weak ocean-atmosphere coupling at boreal winter, balances the cooling trend due to weak Rossby waves, amplified by a strong boreal summer-time coupling. However, while heuristic idealized models such as that of T98 can be quite illuminating, it is both necessary and possible to use more rigorously derived idealized models at different parameter regimes, that are still simple enough to allow exploring the physical mechanisms of ENSO's phase locking.

Various such idealized models have been used to examine ENSO's dynamics in the absence of the seasonal cycle. Neelin (1991), Jin and Neelin (1993a), Neelin and Jin (1993), and Jin and Neelin (1993b) (hereafter JN93) defined three parameter regimes for ENSO's dynamics (see also Neelin et al. (1998)): the fast SST regime in which the response of the SST to thermocline depth changes is instantaneous, the fast wave limit in which the speed of ocean waves (Kelvin and Rossby) is taken to be infinite, i.e. instantaneous adjustment of the thermocline to wind stress anomalies (Hao et al. 1993; Neelin 1991), and the mixed mode regime in which both SST response time and oceanic wave propagation are important (Jin 1997a, b). Other ENSO paradigms focus on different oceanic characteristics and processes such as the displacement of the Pacific warm pool and zonal advection of SST (Picaut et al. 1997), or the role of the Hadley and Walker circulations in the formation of a stationary SST mode (Li and Tianming 1997).

In this work, we investigate the interaction between ENSO-like oscillations and the seasonal cycle using several idealized yet carefully derived models. The models are all based on the dynamics and thermodynamics of the coupled ocean-atmosphere model of Zebiak and Cane (1987) (hereafter CZ-model). We consider seasonal variations in the strength of the response of the wind stress anomalies to SST anomalies, which - at least in the frame work of Zebiak and Cane (1987) - is sensitive to the mean wind convergence and mean SST (Tziperman et al. 1997). Both the mean atmospheric convergence and mean SST determine the strength of the CZ model atmospheric heating due to a given SST anomaly, and thus determine the strength of the wind stress anomalies (Zebiak and Cane 1987). Thus, the same SST anomaly can results in different winds stress anomalies in different months due to the variation of the climatological SST and wind convergence from month to month. We also consider the role of the seasonal variations in the mean upwelling in ENSO's phase locking. The phase locking of ENSO events is analyzed in the fast SST limit, fast wave limit and the mixed mode regime (JN93). Simplified ordinary differential equation (ODE) models are derived for each regime and the interaction between El Niño and the seasonal cycle is interpreted in terms of physical processes such as wave propagation, SST adjustment time etc. While the mixed mode regime is the more realistic of the three, it will be seen below that investigating the less realistic fast SST and fast wave regimes significantly helps in illuminating the role of the different mechanisms acting in the more realistic mixed mode regime.

Our interpretation of the El Niño's phase locking mechanism for the mixed mode and fast SST regimes is, in general, similar to that of T98, but provides a more physical and quantitative picture, revealing the robust as well as uncertain aspects of the locking mechanism. In the fast wave regime, a totally different interpretation of the locking is required, due to the fact that the SST adjustment time rather than the ocean wave travel time is the source of the oscillatory ENSO-like behavior.

The paper is organized as follows: in section 2 we derive a simple ODE in the mixed mode regime, into which the seasonal cycle in introduced. The derivation follows Jin (1997b) physical assumptions, yet uses a different analytical approach, based on integration along wave characteristics. Results are analyzed both for the nonlinear and linear cases, and the physical mechanism for phase locking is presented. In section 3 a model for the fast SST limit is derived out of the mixed mode model of the previous section, and the role of SST adjustment time in the locking mechanism is explored. Section 4 is devoted to the fast wave regime, in which a different ODE model is constructed, following the partial differential equations (PDE) model of Hao et al. (1993). Again, a similar analysis of the phase locking is applied and the phase locking mechanism is explained. In section 5 we first analyze the seasonal ocean-atmosphere coupling strength in the CZ-model to provide a basis for the seasonal coupling strength used in our idealized models. We conclude in Section 6.

2. The mixed mode regime

a. Model equations

Our mixed SST-wave dynamics model is mostly based on the "recharge oscillator" model of Jin (1997a, b), in which model variables are evaluated at an equatorial strip and at an off-equatorial strip and in which the oceanic basin is divided into two zonal boxes. In Jin (1997a, b), thermodynamics are governed by mean upwelling and thermal damping, and Kelvin waves are filtered from the equations, leaving off-equatorial Rossby waves to determine the ocean dynamics time scale. In contrast, we retain the Kelvin waves, and furthermore, derive the model as a delayed oscillator equation for SST in the east Pacific. Both oceanic wave time scales and thermodynamic time scale play a role in the model, hence it is in the mixed wave dynamics - SST regime of JN93. Following the two-strip approximation of Jin (1997b), the equations for the ocean dynamics are solved for the equatorial strip and for the off equatorial strip along wave characteristics.

1) OCEAN DYNAMICS

The model of Jin (1997a, b) is derived from CZ-like ocean dynamics, of a shallow water anomaly model on an equatorial β-plane. Further simplification is achieved by neglecting the meridional damping ($-\varepsilon_m v$) and the meridional wind stress ($\tau_y/\rho H$) terms. The resulting set of equations is

$$\begin{aligned} \frac{\partial u}{\partial t} - \beta y v + g'\frac{\partial h}{\partial x} &= -\varepsilon_m u + \frac{\tau_x}{\rho H}, \quad (a) \\ \beta y u + g'\frac{\partial h}{\partial y} &= 0, \quad (b) \\ \frac{\partial h}{\partial t} + H\left[\frac{\partial u}{\partial x} + \frac{\partial v}{\partial y}\right] &= -\varepsilon_m h, \quad (c) \end{aligned} \tag{1}$$

where u and v are the zonal and meridional anomaly velocities, h is the thermocline depth departure from its mean state, g' is the reduced gravity acceleration, ε_m is the oceanic damping coefficient and H is the mean thermocline depth.

Eliminating u and v from (1), a single equation for h can be obtained,

$$\begin{aligned} \beta y^2(\partial_t + \varepsilon_m)h + \frac{g'H}{\beta}\left[\frac{2}{y}\partial_y - \partial_{yy}\right](\partial_t + \varepsilon_m)h \\ -g'H\partial_x h + \frac{1}{\rho}(\tau_x - y\partial_y\tau_x) = 0. \end{aligned} \tag{2}$$

Following Jin (1997b) we wish to evaluate the equation at the equator ($y = 0$), and at a zonal band off the equator ($y = y_n$). This "two-strip" approximation assumes that the ocean dynamics in the equatorial region is well represented by a combination of equatorial Kelvin waves and off-equatorial long Rossby waves, both well represented by the two strips at latitudes $y = 0$ and y_n.

A Kelvin wave solution of the form

$$h(x,y,t) = h_e(x,t)\exp(-\frac{\beta}{2C_o}y^2), \tag{3}$$

where $C_o = \sqrt{g'H}$, satisfies equation (2), and therefore, taking advantage of the known meridional structure, we get an equation at $y = 0$ of the form

$$-C_o\partial_x h_e + (\partial_t + \varepsilon_m)h_e = \frac{1}{C_o\rho}\tau_{ex}, \tag{4}$$

where τ_{ex} is the wind stress at the equator. In Jin (1997a) the second term on the lhs of (4) is neglected, leaving the east-west thermocline tilt to be in a balance with the wind stress, thus omitting the Kelvin wave propagation. We differ from this strategy by retaining the Kevin waves. Next, rather than using Jin (1997a) two box model along the x-axis, we integrate (4) over the trajectory of an eastward propagating Kelvin wave that starts from the western boundary at a time $t - \tau_2$ and reaches the eastern boundary at a time t, where $\tau_2 = L/C_o$ is the Kelvin crossing time of a basin of length L. The wave is assumed to be excited by the wind stress in the central part of the basin, from $x = x_W + .25L$ to $x = x_W + .75L$. The wind stress is evaluated at the middle of the basin, $x = x_w + L/2$, at a time $t - \tau_2/2$, which is the time when the Kelvin wave crosses the middle of the basin. We denote the thermocline depth anomaly at the western (eastern) edge of the basin by h_{eW} (h_{eE}), and the solution to (4) is then

$$\begin{aligned} h_{eE}(t) = h_{eW}(t - \tau_2)e^{-\varepsilon_m\tau_2} \\ + \frac{1}{\rho C_o}dt\tau_2\tau_{ex}(\frac{L}{2}, t - \frac{\tau_2}{2})e^{-\varepsilon_m\frac{\tau_2}{2}}, \end{aligned} \tag{5}$$

where $dt = 0.5$ is the fraction of crossing time during which the wind stress affects the oceanic waves.

Next, we wish to solve (2) at the off-equatorial band ($y = y_n$), in order to include the Rossby waves dynamics in the model. It can be shown that at $y_n \geq 2L_o$ (where L_o is the oceanic Rossby radius of deformation) the second term in (2) is negligible (Jin 1997b), resulting in the off-equatorial equation

$$-\frac{C_o^2}{\beta y_n^2}\partial_x h_n + (\partial_t + \varepsilon_m)h_n = \frac{1}{\beta\rho}\left[\frac{\partial}{\partial y}(\frac{\tau_x}{y})|_{y=y_n}\right]. \tag{6}$$

Solving (6) again along characteristics, for a Rossby wave that starts from the eastern boundary at time $t - \tau_1$, where $\tau_1 = Ly_n^2\beta/C_o^2$ is the Rossby crossing time of a basin length L, at a latitude y_n, we find

$$h_{nW}(t) = h_{nE}(t-\tau_1)e^{-\varepsilon_m \tau_1} - \frac{1}{\beta\rho} dt\tau_1 \left[\frac{\partial}{\partial y}(\frac{\tau_x}{y})|_{(y_n,\frac{L}{2},t-\frac{\tau_1}{2})}\right] e^{-\varepsilon_m \frac{\tau_1}{2}}. \tag{7}$$

The eastern and western boundary conditions represent the reflection of Kelvin waves into Rossby waves at the east, and the reflection of Rossby waves into Kelvin waves at the west. In terms of the thermocline depth at the boundaries, these boundary conditions are

$$h_{eW} = r_W h_{nW}, \qquad h_{nE} = r_E h_{eE}, \tag{8}$$

where r_W and r_E are reflection coefficients at the western and eastern boundaries, respectively. Using the above boundary conditions, (5) and (7) may be joined to give an expression for the equatorial thermocline depth anomaly at the eastern Pacific,

$$\begin{aligned} h_{eE}(t) = e^{-\varepsilon_m \tau_2} r_W [r_E h_{eE}(t-\tau_1-\tau_2)e^{-\varepsilon_m \tau_1} \\ -\frac{1}{\beta\rho} dt\tau_1 [\frac{\partial}{\partial y}(\frac{\tau_x}{y})|_{(y_n,\frac{L}{2},t-\tau_2-\frac{\tau_1}{2})}] e^{-\varepsilon_m \frac{\tau_1}{2}}] \\ +\frac{1}{\rho C_o} dt\tau_2 \tau_{ex}(\frac{L}{2}, t-\frac{\tau_2}{2})e^{-\varepsilon_m \frac{\tau_2}{2}}. \end{aligned} \tag{9}$$

This form of equation manifests clearly the delayed dependence of $h_{eE}(t)$ on the wave dynamics. The first term represents the Rossby wave that left the eastern boundary at a time $t-\tau_1-\tau_2$, was reflected as a Kelvin wave at time $t-\tau_2$ and arrived to the eastern Pacific at time t. The second term represents the Rossby waves excited at a time $t-\tau_2-\tau_1/2$ in the central Pacific, and the third represents the Kelvin waves excited at a time $t-\tau_2/2$. Note that while T98 described the influence of the wind stress on the ocean dynamics as *amplification* of the Kelvin and Rossby waves, the above more rigorously derived equations indicate that a more appropriate description is that the wind stress *excites* new such waves rather than amplify existing ones.

2) THERMODYNAMICS

The equation describing SST changes at the equator is based on that of Zebiak and Cane (1987). Following Jin (1997a), we only keep the time rate of change, the advection by the mean upwelling $\overline{w}$, and the damping terms,

$$\partial_t T = -\varepsilon_T T - \gamma \frac{\overline{w}}{H_1}(T - T_{sub}(h)), \tag{10}$$

where ε_T is a thermal damping coefficient, $T_{sub}(h)$ is the temperature anomaly at a depth H_1, and is a function of the thermocline depth anomaly h (Munnich et al. 1991; Zebiak and Cane 1987) (see appendix A). The parameter γ relates the temperature anomalies entrained into the surface layer to the deeper temperature variations due to $T_{sub}(h)$ (see Zebiak and Cane (1987)).

3) OCEAN-ATMOSPHERE INTERACTION

Following Gill (1980), Hao et al. (1993) and Jin (1997b), we take the wind stress to be a function of the SST at the equator (T_e)

$$\tau_x(x,y,t) = \mu A(T_e,x)\exp(-\frac{y^2\alpha}{2L_o^2}), \tag{11}$$

where $A(T_e,x)$ is a nonlocal function that relates the equatorial SST to wind stress, and μ serves as a relative coupling coefficient which we allow to change seasonally. The wind stress terms in (9) may thus be expressed as

$$\begin{aligned} \tau_{xe} = \mu A(T_e,x), \\ \partial_y(\tau_x/y)|_{y=y_n} = -\mu A^* A(T_e,x), \end{aligned} \tag{12}$$

where

$$A^* = \left[\frac{L_o^2 + \alpha y_n^2}{(y_n L_o)^2}\right] e^{-\frac{y_n^2\alpha}{2L_o^2}}, \qquad \alpha = (\frac{L_o}{L_a})^2,$$

and L_a is the atmospheric Rossby radius of deformation. $A(T_e,x)$ may be obtained by solving a Gill-type atmospheric model (Gill 1980) using a long wave approximation (see (Hao et al. 1993), or (B-1) in appendix B below), resulting in a linear relation between the wind stress and the equatorial SST. As in Jin (1997a), the function $A(T_e,x)$ for the wind stress in the central Pacific, appearing in (9), is now assumed to be proportional to the temperature in the eastern Pacific

$$A(T_e, x = x_w + L/2) = b_0 T_{eE}(t), \tag{13}$$

where b_0 is the annual mean coupling strength. The assumption embedded in (13) is that most of the SST variability is in the eastern part of the equatorial Pacific. The resulting wind stress, according the Gill model, will be in the central Pacific (Jin 1997a).

4) MIXED MODE MODEL

Equation (9) can be written, using (13) and (12), as

$$\begin{aligned} h_{eE}(t) = e^{-\varepsilon_m \tau_2} r_W r_E h_{eE}(t-\tau_1-\tau_2)e^{-\varepsilon_m \tau_1} \\ -e^{-\varepsilon_m \tau_2} r_W \frac{1}{\beta\rho} A^* dt\tau_1 \mu(t-\tau_2-\frac{\tau_1}{2}) \end{aligned}$$

$$\times b_0 T_{eE}(t-\tau_2-\frac{\tau_1}{2})e^{-\varepsilon_m\frac{\tau_1}{2}}$$

$$+\frac{1}{\rho C_o}dt\tau_2\mu(t-\frac{\tau_2}{2})b_0 T_{eE}(t-\frac{\tau_2}{2})e^{-\varepsilon_m\frac{\tau_2}{2}}, \qquad (14)$$

expressing $h_{eE}(t)$ as function of h_{eE} and T_{eE} at previous times. As before, the first term represents the free Rossby and Kevin waves, the second represents the excited Rossby wave, and the third represents the excited Kelvin wave. The thermodynamic equation (10) evaluated at the eastern side of the basin gives the dynamical equation in which $h_{eE}(t)$ is used

$$\partial_t T_{eE} = -\varepsilon_T T_{eE} - \gamma\frac{\overline{w}}{H_1}(T_{eE} - T_{sub}(h_{eE})). \qquad (15)$$

Equations (14) and (15) together with appendix A for T_{sub}, form our mixed mode model for the investigation of ENSO's tendency to peak toward the end of the calendar year. Hereafter we denote T_{eE} by T and h_{eE} by h. Note that the nonlinearity in the model is due to the nonlinear function $T_{sub}(h)$.

b. Results

The mixed mode delayed oscillator model (14,15) was solved numerically using NAG routine D02CBF (Numerical Algorithm Group). The values of all model parameters are specified in Table 1. In the absence of a seasonal cycle, model integration shows similar results to that of Jin (1997a). Events occur every 4.3 years with an averaged maximum of east Pacific warming amplitude around 2.5 degrees (not shown). As expected, there is no phase locking to the seasonal cycle as the latter is not represented in the model. In the next subsection we impose on the model a seasonally varying relation between the wind stress and the SST, as well as a seasonally varying climatological upwelling, and analyze their interaction with the ENSO-like oscillations.

1) SEASONALLY VARYING OCEAN-ATMOSPHERE COUPLING STRENGTH

The seasonal cycle may enter in our model via two different physical mechanisms. The first and most important is the ocean-atmosphere seasonal coupling coefficient μ in (14). The seasonal variation in this parameter was shown to be, at least in the CZ-model, a result of the seasonal cycle in both the mean SST and wind divergence (Tziperman et al. 1997). The influence of the mean SST and mean wind convergence on ocean-atmosphere interaction is through their effect on the atmospheric heating (Hirst 1986; Philander 1983; Tziperman et al. 1997). The other parameter that may vary seasonally is the mean upwelling ($\overline{w}$) in the eastern equatorial Pacific appearing in the SST equation.

parameter	value
mixed mode regime	
ε_T	$4 month^{-1}$
γ	0.75
$\overline{w}$	$45 m\cdot month^{-1}$
H_1	$75m$
ε_m	$30 month^{-1}$
C_o	$2.7m\cdot sec^{-1}$
L	$1.5\cdot 10^7 m$
L_o	$3.4\cdot 10^5 m$
α	0.1
y_n	$6.8\cdot 10^5 m$
β	$2.3\cdot 10^{-11} m^{-1} sec^{-1}$
ρ	$1000 kg\cdot m^{-3}$
τ_1	$2.1 month$
τ_2	$8.5 month$
b_0	$1.2\cdot 10^{-2} kg\cdot sec^{-2} m^{-1} C^{-1}$
r_W	0.75
r_E	0.9

TABLE 1. Summary of parameters in the mixed mode model.

For simplicity we take the relative coupling coefficient to vary in time as a cosine with a one year period. The phase is taken to be such that maximum coupling is reached in the middle of May and its minimum value in the middle of November,

$$\mu = 1 + \varepsilon\cos(w_a t - \phi), \qquad (16)$$

where ε is the strength of the seasonal cycle (taken to be 0.1), $w_a = 2\pi/12$ is the annual frequency, and $\phi = 5\pi/6$ is the phase. We base the seasonal variations in the coupling strength on the analysis of the CZ-model presented below in section 5, showing that the coupling strength reaches its maximum in May and its minimum in September.

Figs. 1a-c show the results for this case. The SST time

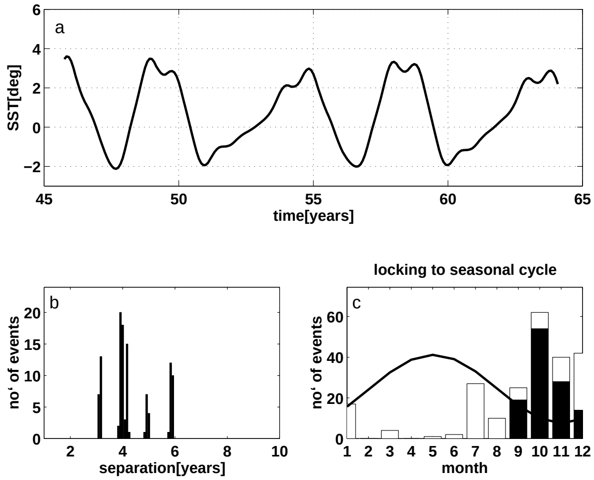

FIG. 1. The effect of a seasonally varying coupling strength in the mixed mode model equations (14) and (15): (a) A time series of the model eastern Pacific temperature; (b) histogram of the separation between events; (c) number of event peaks in each month of the calendar year (black bars are for El Niño events and white bars are for La Niña events).

series in Fig. 1a shows that events are not as regular as in the absence of a seasonal cycle (see Chang et al. 1995; Jin et al. 1994; Tziperman et al. 1994, 1995). Their amplitude now varies from 2 to 4 degrees, events occurrence is every 3-6 years (Fig. 1b), and the most pronounced finding, shown in Fig. 1c, is that events tend to peak in the months September-December, about 6 months after the coupling maximum strength, and when the coupling is reaching its minimum. This finding is in agreement with T98, although the model used here is very different.

Sensitivity tests show that the model displays ENSO-like variability in a parameter regime that is within about 10% of the model parameters specified in Table 1, with individual parameter sensitivity that allows for ENSO-like variability being from 5% to 20%. In any case, within the ENSO-like regime, the model phase locking is very robust, i.e. its tendency to peak toward the end of the calendar year persists even when the event's amplitude or frequency changes when model parameters are perturbed.

2) SEASONALLY VARYING UPWELLING

The influence of a seasonally varying upwelling was investigated by Tziperman et al. (1997) using the CZ-model. Their two main findings were that seasonal upwelling variations are of a second order significance to ENSO's locking to the seasonal cycle, and that in the absence of seasonal upwelling variations, the event amplitude rises fairly significantly.

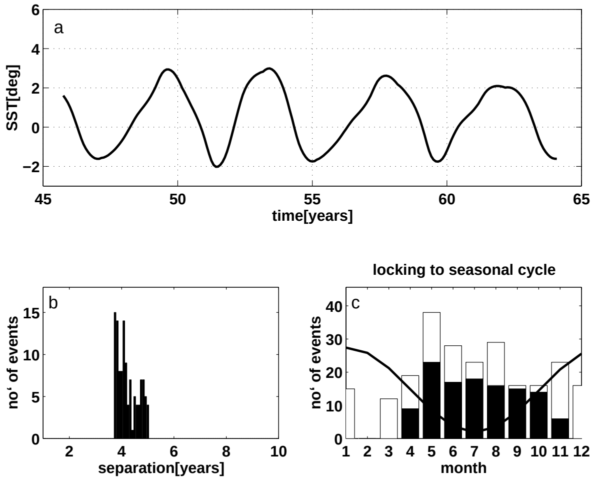

FIG. 2. As in Fig 1, for seasonal upwelling.

In our model, mean upwelling is a key parameter; changing its value influences the model behavior substantially. For instance, increasing its value by 20 percents causes events to be stronger (about 4 degrees at the peak) and less regular, and the separation between events to shortens from 4 to 3 years. A similar decrease in upwelling will affect the model in the opposite way.

The climatological seasonal upwelling used in the CZ-model varies in the east equatorial Pacific from around $60m/month$ at January to around $30m/month$ at June. We therefore take the climatological upwelling to be $\overline{w}[1+.25\cos(2\pi t/12)]$, where $t=0$ coincides with the beginning of January. In the run shown in Fig. 2, ocean-atmosphere coupling is set to its annual mean value, leaving only the upwelling to vary seasonally. In this case, events tend to peak in May-October when the upwelling reaches its minimum, and more significantly, the event peaks are less locked to the seasonal cycle than in the seasonally varying coupling strength case.

3) COMBINED EFFECT OF COUPLING STRENGTH AND UPWELLING

Next we wish to examine the event locking to the seasonal cycle when both the ocean-atmosphere coupling and the mean upwelling change seasonally (Fig. 3). In spite of the seasonally varying upwelling the events peak time remains confined to September-November, almost as in the case of seasonally varying coupling strength only (see Fig. 1). This result, together with those of Fig. 2, implies that the overall influence of upwelling is of a secondary importance in comparison with the influ-

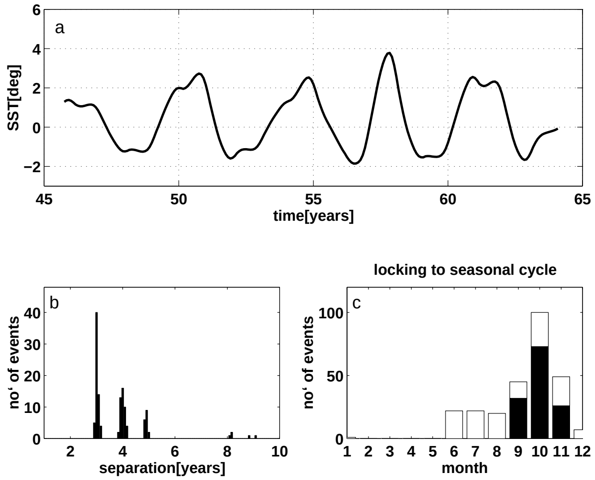

FIG. 3. As in Fig 1, for the combined case of seasonal coupling strength and seasonal upwelling.

ence of the ocean-atmosphere coupling coefficient (i.e. the influence of climatological seasonal SST and wind divergence). Another finding is that the averaged El Niño amplitude is now smaller than that of the standard case. Both findings are in a striking agreement with the experiments of Tziperman et al. (1997) using the fuller CZ-model, suggesting that the simplified model captures the essence of the CZ-model.

In all three runs of the model presented above, the phase locking of the weaker La Niña events is less robust than that of the El Niño events. This less robust locking is a result of the asymmetry in the function $T_{sub}(h)$, which results in a weaker feedback between thermocline movements and SST during La Niña events. This weaker feedback is also the reason for the La Niña events being weaker than the El Niño events. The phase locking of observed La Niña events to the seasonal cycle is, like in our model, less robust than that of the El Niño events, and we will therefore address in the followings only to the phase locking of El Niño events.

c. Physical mechanism for phase locking in the mixed mode regime

We now derive a linearized version of the model, in order to analyze the mechanism that controls El Niño's locking to the seasonal cycle in the mixed mode regime. The linearization of the model allows us to separate the different processes (Rossby and Kelvin waves, and upwelling) that affect the SST in the eastern equatorial Pacific, and to carefully analyze each term in a way that is not possible with the nonlinear model. It is shown below that this linearization does not affect the nature of the oscillations and its phase locking. Expanding T_{sub} in a Taylor series, with only the first term retained, we find

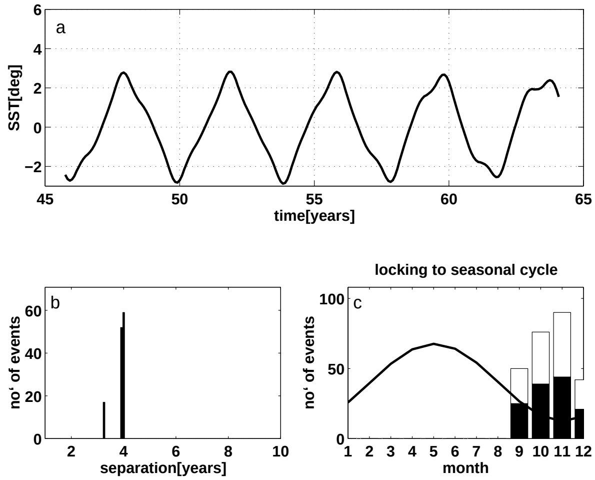

FIG. 4. As in Fig 1, for the linearized mixed mode model.

$$T_{sub} \cong \delta h, \tag{17}$$

where $\delta \equiv \partial_h T_{sub}|_{h=0} = 0.25[deg/m]$.

The solution of this linearized model is shown in Figs. 4a-c. It is very convenient to analyze the physical mechanism when the oscillations are exactly neutrally stable in between these two regimes, which occurs for $b_0 = 1.476 \cdot 10^{-2}$. This tuning of b_0 is needed as without the nonlinearity which limits the event amplitude, the linearized model can produce either exponentially growing or exponentially decaying oscillation. Events are still locked to the end of the year as in the nonlinear model, and therefore analyzing the linear model should reveal the physical mechanism of the nonlinear model as well.

In the fully nonlinear model, nonlinear phase locking to the external periodic seasonal forcing can drive different initial conditions to the same phase locked solution. In the linearized model, however, the phase information of the initial conditions is preserved during the model run. We therefore need to show that the phase locking in the linearized model does not depend on the initial conditions. Fig. 5 shows 12 superimposed SST time segments from the linear model, each corresponding to an integration that is initialized in the same way, yet at a different month. In spite of the fact that each integration has a different initial phase with respect to the seasonal cycle, events in all integrations reach their peak at the end of the year. Therefore, ENSO's phase locking in our simple model is not a result of its nonlinearity, but is a result of the seasonal modulation of the background model pa-

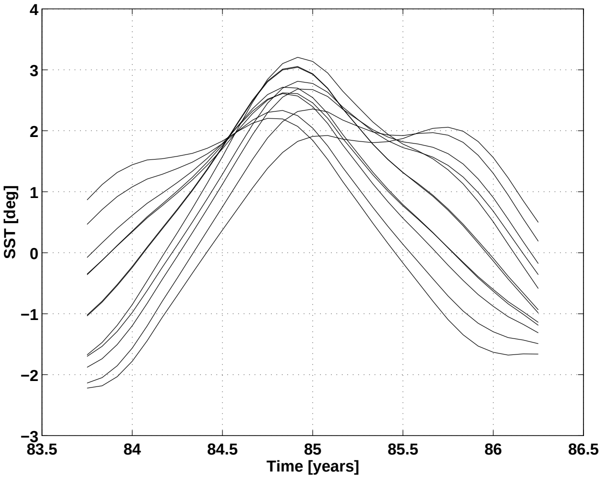

FIG. 5. Twelve time series of SST in the linearized mixed mode model, corresponding to integrations starting at twelve different months. Events tend to peak toward the end of the calendar year irrespectively of the initial conditions, like in the non-linear model.

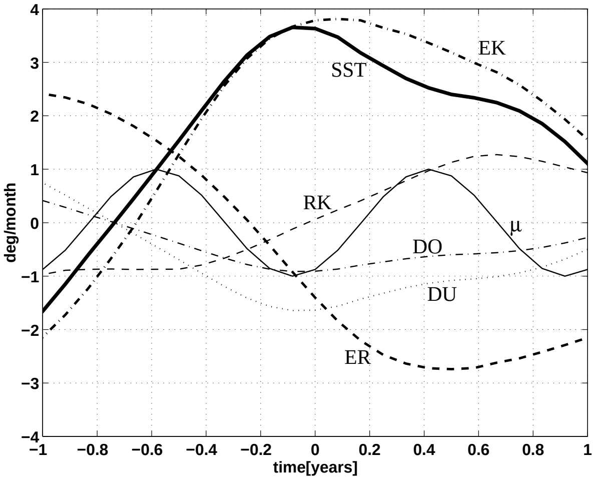

FIG. 6. A time series of the linearized mixed mode model, showing the terms in the SST tendency equation for one specific event: *DO* is the thermal damping of the SST, *DU* is damping due to the upwelling, *RK* is the free Rossby-Kelvin wave, *ER* is the excited Rossby wave, and *EK* is the excited Kelvin wave. *DO*, *DU*, *RK*, *ER* and *EK* are in $deg/month$, *SST* is in deg. Also shown is the seasonal coupling variation μ.

rameters. This behavior was also found by Battisti and Hirst (1989) in their simplified models. We can now proceed to understand the details of the physical locking mechanism in the linear model, with the understanding that it also applies to the nonlinear model for which the separation of terms cannot be done explicitly.

Substituting (17) in (15) results in

$$\partial_t T = -\varepsilon_T T - \gamma \frac{\overline{w}}{H_1}(T - \delta h), \tag{18}$$

where h is evaluated using (14). Time series of all terms (during a specific event) in (18) are shown in Fig. 6. The terms represent:

$$DO = -\varepsilon_T T \tag{19}$$

$$DU = -\gamma \frac{\overline{w}}{H_1} T \tag{20}$$

$$RK = +\delta\gamma \frac{\overline{w}}{H_1} e^{-\varepsilon_m \tau_2} r_W r_E h(t - \tau_1 - \tau_2) e^{-\varepsilon_m \tau_1} \tag{21}$$

$$\begin{aligned} ER = & -\delta\gamma \frac{\overline{w}}{H_1} e^{-\varepsilon_m \tau_2} r_W \frac{1}{\beta\rho} A^* dt \tau_1 \mu(t - \tau_2 - \frac{\tau_1}{2}) \\ & \times b_0 T(t - \tau_2 \frac{\tau_1}{2}) e^{-\varepsilon_m \frac{\tau_1}{2}} \end{aligned} \tag{22}$$

$$EK = +\delta\gamma \frac{\overline{w}}{H_1} \frac{1}{\rho C_o} dt \tau_2 \mu(t - \frac{\tau_2}{2}) b_0 T(t - \frac{\tau_2}{2}) e^{-\varepsilon_m \frac{\tau_2}{2}}, \tag{23}$$

so that

$$\delta h = RK + ER + EK. \tag{24}$$

DO is the thermal damping of the SST, *DU* is the part of the upwelling that depends on the SST. The first two terms depend on $T(t)$ with a negative coefficient, hence they always tend to diminish SST anomalies. *RK* represents the free Rossby wave that left the eastern boundary of the basin 10 months $(\tau_1 + \tau_2)$ before peak time, traveled to the western boundary for about 8 months and was reflected back as a Kelvin wave that reached the eastern boundary after two more months. The emanated wave was damped on its way due to oceanic momentum damping (ε_m) and due to imperfect reflection at the western boundary (r_W). *RK* depends only on $h(t - \tau_1 - \tau_2)$ and therefore is not influenced by the seasonal cycle. *ER* stands for the excitation of Rossby waves in the center of the basin due to the wind stress. The excitation is in opposite sign to the wind stress, since positive wind stress (westerlies) causes the shift of warm water towards the equator; thus exciting cold anomalies off the equator that travel westward as upwelling Rossby waves. This is the term that eventually terminates the events, or in other words, this term represents the system's 'memory' that maintains the oscillation. The fifth term, *EK*, represents the excitation of Kelvin waves in the mid-Pacific basin, again due to the wind stress, only this time the excitation has the same sign as the wind stress. As before, a positive wind stress anomaly causes warm water to shift from off-equator towards the equator; the warm water excess at the equator drives a thermocline deepening signal that travels eastward as a Kelvin wave, reaching the eastern boundary after about 1 month. Both ER and EK depend on the seasonal cycle through the seasonal sensitivity of wind stress anomalies to SST anomalies, and therefore are key elements in ENSO's interaction with the seasonal cycle.

Let us now examine the physical mechanism of an event phase locking, examining the different terms in the SST equation (Fig. 6) at the event peak time at $t \approx -0.1$ (i.e. December of year -1; time $t = 0$ is defined to be the January 1st nearest to the event's peak time). At that point all terms at the rhs of (18) cancel each other to give zero temperature time tendency ($\partial T/\partial t = 0$).

The main balance is between the warming Kelvin waves excited in the middle of the basin a month before peak time, EK, and the excited Rossby waves, ER, that cool the SST. The excited Kelvin waves are forced by the large wind stress that existed a month before the event peak time. Yet, these Kelvin waves' amplitude is affected at the time of excitation by the small coupling strength in the boreal winter, near the event peak time (μ in eq. 19). The excited Rossby waves, ER, are forced by the wind anomaly 6 months before their arrival to the eastern boundary as Kelvin waves. At that time, the event amplitude and thus the amplitude of the wind that has forced these waves is small. However, the coupling strength six months prior to the event peak time, during boreal spring and early summer, is large, resulting in a significant amplitude of the excited cold Rossby waves. Thus, exactly at the event peak time, the warm Kelvin waves excited by a strong wind stress and weak coupling balance the cold Rossby waves excited by a weaker wind stress but stronger coupling. This balance depends on the timing between the amplitudes of the seasonal coupling strength and of the ENSO event, and could not have occurred at summer time. After the peak time, the cold anomalies dominate the SST tendency equation, and eventually terminate the event.

3. The fast SST Limit

The purpose of this section is to understand the role of the SST adjustment time, which was ignored in section 2, in ENSO's phase locking by analyzing a parameter regime in which this time scale is neglected altogether.

a. Model equations

In the fast SST limit, the SST adjustment time is much shorter than the ocean dynamics adjustment time, or in other words SST is assumed to respond instantaneously to thermocline depth changes (JN93, Neelin 1991). We obtain our model equations for this limit by taking the term $\partial_t T_{eE}$ in (15) to be zero, so that the SST equation becomes a diagnostic equation of the form

$$T(t) = \gamma \frac{\overline{w}}{H_1} \left(\varepsilon_T + \gamma \frac{\overline{w}}{H_1} \right)^{-1} T_{sub}(t). \tag{25}$$

Furthermore, instead of using (14) to represent the Rossby and Kelvin waves through integration along wave characteristics, we use (5) for the Kelvin waves, and the prognostic equation (6), discretized using two zonal boxes (Jin 1997a) for Rossby waves,

$$\partial_t h_{nW}(t) = -\varepsilon_m h_{nW}(t) + \frac{c^2}{\beta y_n^2 L}(h_{nE}(t) - h_{nW}(t)) - \frac{1}{\beta\rho} A^* \mu(t) b_0 T(t). \tag{26}$$

The reason for this change is to avoid numerical noise that arises in non-differential delayed equations such as (14), although in principle we could have used (14) and (25).

To obtain an oscillation that resembles the observed ENSO characteristics, some model parameters need to be modified, and since the fast SST limit is not a realistic one, the required change in parameters may lead to less realistic values. We therefore investigated two versions of this limit, both of which simulate reasonable ENSO-like events, but each controlled by a different set of parameters (Table 2). Even though the two versions differ fairly substantially, they display similar locking to the seasonal cycle with a similar locking mechanism, which clearly testifies to the robustness of the phase locking mechanism. As the results are similar for both versions of the fast SST model, we analyze here version I only.

b. Results

The model was integrated numerically with a seasonally varying coupling coefficient (16), for a period of 500 years. Fig. 7 shows the results for version I: Events show a clear tendency to lock to months August-October with maximum number of event peaks in September. In the mixed mode regime (Fig. 1), locking to the seasonal cycle was in general similar but shifted by 1-2 months toward the end of the year. The results for version II are similar (not shown) except of the events being stronger and the La Niña events being less locked to the seasonal cycle.

c. Phase-locking mechanism

In the fast SST limit, the time of maximum SST anomaly is also a time of maximum thermocline depth

parameter	modified value
fast SST limit - version I	
y_n	$10 \cdot 10^5 m$
dt	0.75τ
k	$0.12° \cdot m^{-1}$
fast SST limit - version II	
C_o	$2.3 m \cdot sec^{-1}$
dt	0.75τ
k	$0.1° \cdot m^{-1}$
fast wave limit	
ε_a	2.5
x_0	$0.75L$
x_c	$0.5L$
x_e	$0.9L$
b_0	$9 \cdot 10^{-2} kg \cdot sec^{-2} m^{-1} C^{-1}$

TABLE 2. Parameters in the fast SST and fast wave models, that were modified from the values used in the mixed mode model.

anomaly (25). Therefore we can use equation (5) for the thermocline depth at the eastern boundary, h_{eE}, in order to analyze the locking of the peak time for both h_{eE} and the SST. The two terms in (5) represent the reflected Rossby wave (*ROS*), and the Kelvin wave excitation due to wind stress (*KEL*). In the fast SST regime, these terms directly determine the SST, whereas in the mixed mode regime they influence the time derivative of the SST equation along with other factors. For reference we note that *ROS* in this case is equivalent to the sum of RK and ER in the mixed mode model, KEL is equivalent to EK. Fig. 8 shows time series of all terms for a single event.

While the details of this fast wave model are different from those of the mixed mode model of the previous section, the physical mechanism of ENSO's phase locking to the seasonal cycle is still largely the wave dynamics mechanism explained in the previous section, with the related wave time scales (τ_1 and τ_2). The two main competing feedbacks are still the warming Kelvin waves and the cooling Rossby waves. SST maximum is reached when the SST warming tendency due to the Rossby wave excited six months prior to the peak time (*ROS* term), balances the SST cooling tendency due to the Kelvin excited one month prior to the peak time (the KEL term).

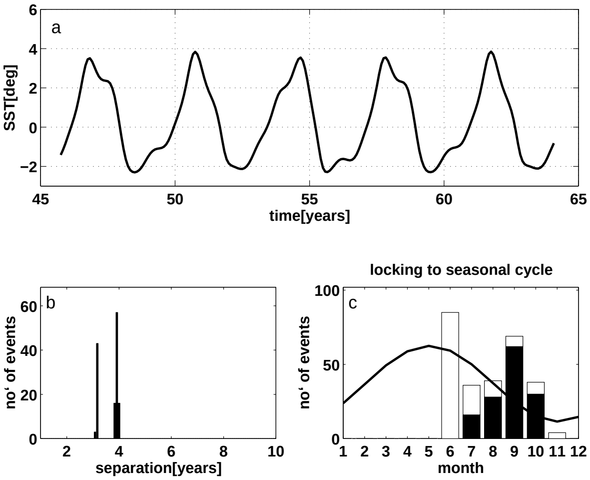

FIG. 7. As in Fig 1, for the effect of a seasonally varying coupling strength in the fast SST limit (version I).

However, a comparison between the mixed mode results (Fig. 1) and the fast SST results (Fig. 7) shows that there is about two months difference in the event peak time. This two months difference between the mixed mode regime and the fast SST limit can be explained by the lack of two months delay time due to upwelling in the fast SST limit. as $[\overline{w}/H_1]^{-1} \approx 2$ months, (25). Therefore, in the mixed mode regime we can expect events to reach to their maximum two months later than events in the fast SST limit (Fig. 9).

We can therefore conclude this analysis of the fast SST limit with the main lesson being that the role of the SST adjustment time in the more realistic mixed mode regime is to shift the peak time by about two months towards the end of the calendar year.

4. The fast wave limit

In the fast wave limit, the Rossby and Kelvin wave propagation speeds are assumed infinite, resulting in an instantaneous adjustment of ocean thermocline depth and current velocities to wind stress anomalies (Hao et al. 1993; Neelin 1991). Hence, the SST adjustment time to thermocline depth changes plays the central role in the physical mechanism of the oscillations obtained in this parameter regime (Hao et al. 1993). The fast wave limit results in somewhat unrealistic oscillations, in comparison to both ENSO's time scale and amplitude (JN93, Hao et al. 1993; Neelin 1991), as this is not a re-

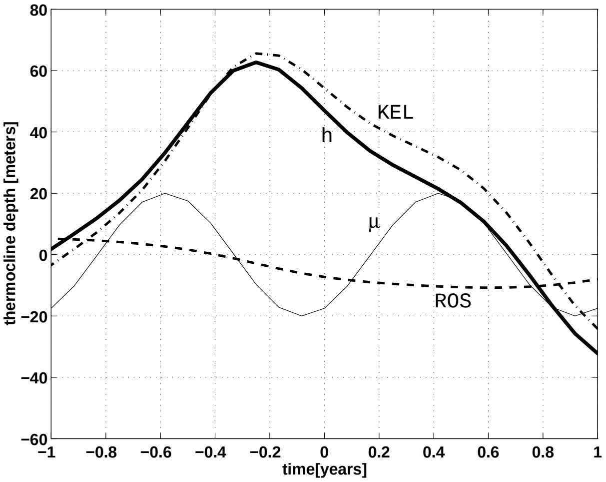

FIG. 8. Time series of the fast SST limit (version I), showing the terms in the thermocline depth equation for one specific event. *KEL* is the excited Kelvin wave and *ROS* is the Rossby wave term.

alistic ENSO regime. Nevertheless, it is still useful to analyze ENSO's phase locking in this regime, since it reveals some new aspects not considered in the previous two regimes.

a. Model equations

The fast wave limit can be derived by taking the time derivatives terms in the ocean momentum equation (1) to be zero. In the fast wave limit, the dynamics crucially depend on the east-west tilt of the thermocline. Therefore, we divided the basin into two boxes, one for the east Pacific and one for the central Pacific. The full derivation of the model equations is given in Appendix B, and is a simplification into a system of ODEs based on the PDE model of (Hao et al. 1993). The two SST tendency equations for the two regions are

$$\partial_t T_c = -\varepsilon_T T_c - \gamma \frac{\overline{w}}{H_1} T_c + \gamma \frac{\overline{w}}{H_1} T_{sub}\left(h_c(T_c, T_e)\right), \quad (27)$$

$$\partial_t T_e = -\varepsilon_T T_e - \gamma \frac{\overline{w}}{H_1} T_e + \gamma \frac{\overline{w}}{H_1} T_{sub}\left(h_e(T_c, T_e)\right), \quad (28)$$

where T_c and T_e are the SST in the central Pacific and the eastern Pacific respectively, and the dependence of T_{sub} on T_c and T_e is via the thermocline depth anomalies h_c and h_e (see appendix B). Table 2 summaries the model parameters used for this model.

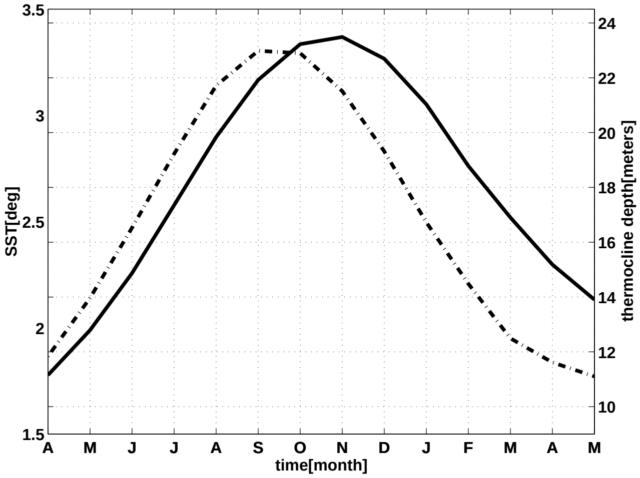

FIG. 9. Time series of *SST* (solid) and *h* (dash-dot) in the mixed mode regime. The figure shows the delay between the two, which is missing in the fast SST regime, causing the locking of events to occur about two months earlier in the fast SST regime.

b. Results

The oscillatory mechanism of the eastward propagating fast wave oscillations is explained in Hao et al. (1993) (see also appendix B). The seasonal cycle is introduced as before (16) via a coupling coefficient between wind-stress and SST anomalies. The simplification in the ocean dynamics and the simple two box zonal discretization allows us to include a somewhat more elaborated atmospheric model with local ocean-atmosphere coupling in both the eastern and central Pacific. We take here the coupling coefficient to vary seasonally only in the eastern box ($\mu_2 = \mu$), whereas in the central box it remains constant ($\mu_1 = const$). Events in this seasonal fast wave model tend to peak in August-October (Fig. 10). Integrating the model with a seasonally varying coupling strength in both boxes shows a weak locking to months May-October (not shown), whereas integration with seasonal coupling in the central basin only results in event peaking in February-June (not shown). Introducing a climatological seasonal upwelling (16) results, as in the mixed mode regime, in a weak locking to months January-July (not shown). The combined effect of both seasonal varying coupling coefficient and seasonal upwelling tends to weaken events locking with maximum event at July-November (not shown). Clearly the phase locking in this regime is not very robust.

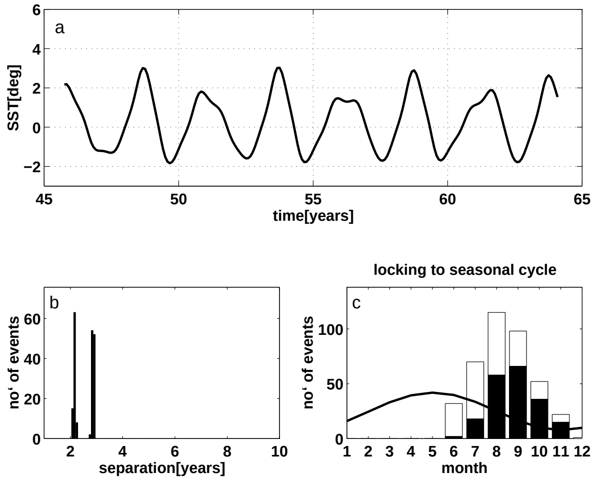

FIG. 10. As in Fig 1, for a seasonally varying ocean-atmosphere coupling strength in the fast wave limit.

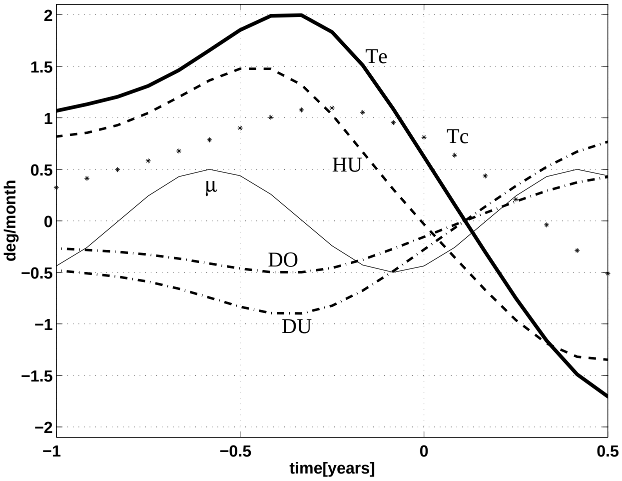

FIG. 11. A time series of the terms in the SST equation for the eastern box in the fast wave limit for one specific event. *DO* is the thermal damping term, *DU* is the damping due to the upwelling, and *HU* is the part of the upwelling that depends on the thermocline depth h_e.

c. Physical mechanism for phase locking

Although our model is formulated to be similar to the eastward propagating fast wave case of Hao et al. (1993), our coarse two box discretization in the zonal direction eliminates the specific mechanism responsible for the eastward propagation in Hao et al. (1993). Instead, the central Pacific temperature lags behind that of the eastern Pacific, indicating a westward propagation (Fig. 11). This, however, does not affect the basic oscillatory mechanism in this fast wave limit.

Denote the first and second terms in (27) and (28) as *DO* and *DU* (corresponding to SST damping due to Newtonian cooling and upwelling respectively), and the third term as *HU*, representing the effect of the thermocline depth on the upwelling. At the peak time, $\partial_t T_e = 0$, which implies that *DO* and *DU* balance *HU*. Fig. 11 shows the three terms in the SST equation for the eastern box. *HU*, which contributes to the growth tendency, is affected strongly and positively (through a seasonal varying coupling strength) by T_e and weakly and negatively (with a constant coupling strength) by T_c (see B-13). During the first 6 months of year -1 prior to the peak time, *HU* is growing since it is affected mainly by the rapidly growing T_e which is amplified by a growing coupling strength, whereas the negative effect of T_c is weak due to the small amplitude of the central Pacific warming. Around July, *HU* reaches its peak due to the combination of the growing T_c and the decreasing coupling strength that weakens the effect of T_e. The SST reaches its peak 2-3 months after the time of maximum *HU* due to the finite SST adjustment time (i.e. the upwelling time scale). Fig. 11 shows that T_e always lags *HU* by 2 months.

In the fast wave limit, the mechanism both for the oscillatory nature of El Niño and for the interaction with the seasonal cycle, are entirely different from those for the mixed mode and the fast SST regimes. The locking of the events peak time to the seasonal cycle is very different from the observed one. There is only 2-3 months difference between the time of maximum ocean-atmosphere coupling strength and the time of event peaks in the fast wave regime. Clearly, the additional time delay needed for the events to peak towards the end of the year must come from the finite wave propagation time, which is omitted in this regime.

5. Seasonal ocean-atmosphere interaction in the CZ-model

Throughout this paper we use a linear relation for the coupling between wind stress and SST anomalies (13) with a coupling coefficient that varies monthly. We now analyze this seasonal relation using the CZ-model. A similar analysis based on observations would have made a stronger point, but such an analysis is left for future work.

The SST and the wind stress anomalies in the CZ model, have been least-square fitted as $\tau_c^{m,j} = b_0^m Nino3^{m,j}$, for a 300 year time series. Here, τ_c is the zonal wind stress averaged over the central Pacific (160E-120W and 3S-3N), Nino3 is the SST averaged over 5S-5N and

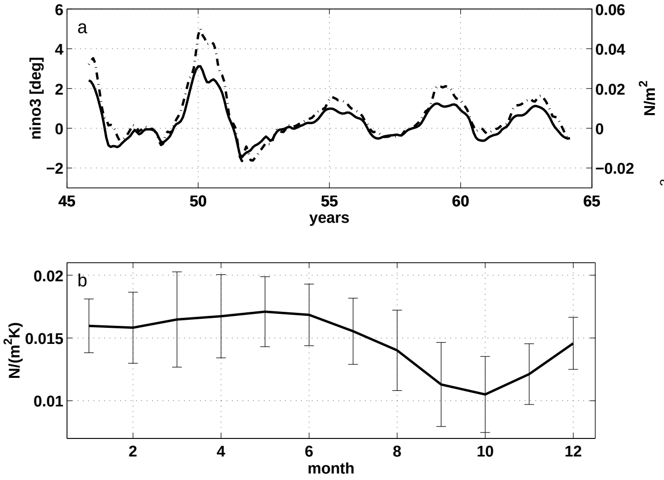

FIG. 12. (a) Time series of $Nino3$ (solid) and wind stress τ_c (dash-dot). (b) Regression of τ_c and $Nino3$ in the CZ-model, as function of month of the year. Vertical bars indicates the variance in the least-square fit.

90W-150W, j sums over all the time series points in a given month, and m stands for the month index. Figs. 12 and 13 show b_0 as a function of month. There is an evident seasonal cycle with the maximum coupling at May and the minimum coupling at September. Vertical bars indicate the standard deviation of the least square fit calculation, ($std(m)$), estimated as

$$std(m) = \sqrt{\sum_{j=1}^{300} (\tau_c^{m,j} - b_0^m Nino3^{m,j})^2 / \sum_{j=1}^{300} (Nino3^{m,j})^2}, \tag{29}$$

where b_0^m is the monthly coupling coefficient calculated from the least square fit, and the summation is over 300 occurrences of each month in the data set. Clearly $std(m)$, representing the year to year variations in the seasonal coupling, should be small if our phase locking mechanism which depends on the seasonal variations of b_0 is to account for the fairly robust phase locking in the CZ model. Indeed, it seems that the std is smaller than the seasonal signal in the coupling coefficient b_0^m.

Based on the dependency of b_0^m on the month of the year we constructed the simple parameterization for the seasonal variation of the coupling coefficient (16) to reach its maximum at May and its minimum at November. Note again, that the behavior of b_0^m was shown by Tziperman et al. (1997) to be mostly a result of seasonal variations in the mean wind convergence and the mean SST.

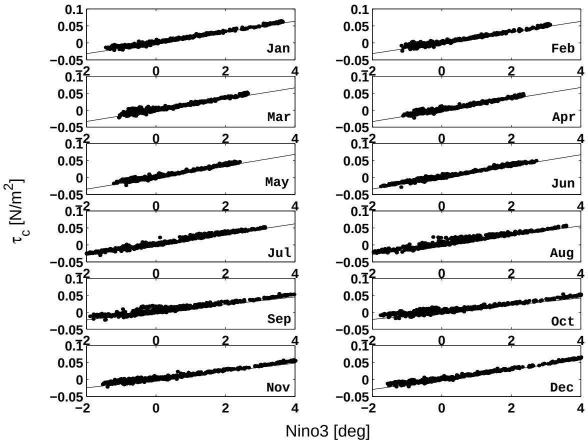

FIG. 13. τ_c vs. $Nino3$ as function of month of the year. Lines indicate least-square fit.

6. Conclusions

The phase locking of idealized ENSO models to the seasonal cycle was examined in three parameter regimes: the fast SST limit, the fast wave limit, and the mixed mode regime (JN93, Neelin 1991). The idealized models used here for all three regimes are based on simplifications to the dynamics and thermodynamics of the CZ-model.

The phase locking mechanism in the mixed mode and fast SST regimes relies on the seasonal excitation of the Kelvin and the Rossby waves by wind stress anomalies in the central Pacific basin. The peak time of the events is set by the dynamics to allow a balance between the warming and cooling trends due to downwelling Kelvin and upwelling Rossby waves. This balance is obtained because the warming trend due to the large amplitude Kelvin waves, amplified by a weak boreal winter-time ocean-atmosphere coupling strength, balances the cooling trend due to weak Rossby waves, amplified by a strong boreal summer-time coupling strength. The comparison of ENSO's phase locking in the fast SST limit and in the mixed mode regime demonstrated that the adjustment time of SST to changes in thermocline depth can shift the event peak time by about two months in our idealized models. This SST adjustment time may therefore be an important part of the mechanism responsible for the phase locking of observed ENSO events.

In addition to exploring the detailed locking mechanism, we have shown explicitly that ENSO's phase locking in our simple models is not a result of the model nonlinearity, but is a result of the seasonal modulation of the background model parameters, and can occur in linearized dynamics as well as in nonlinear dynamics.

In order to support our idealized model analysis, we calculated the seasonal ocean-atmosphere coupling strength (the regression coefficient between the wind stress and the SST) in the CZ model. We showed that the maximum coupling strength occurs in May whereas its minimum is in September, consistent with the coefficient used in the above idealized models.

This study of ENSO's seasonal phase locking mechanism is, hopefully, a step forward from the heuristic model of Tziperman et al. (1998). The simple, yet more rigorously derived models used here enabled us to explore the physical mechanisms underlying ENSO's phase locking to the seasonal cycle in a variety of more and less realistic parameter regimes. Yet, further validation of the proposed mechanisms, especially by means of data analysis and data assimilation into fuller coupled models, is obviously still needed for a fuller understanding of ENSO's phase locking.

Acknowledgment. We would like to thank Steve Zebiak and Mark Cane for allowing the use of their model and to Yochanan Kushnir for useful discussions. This work was partially funded by the Israeli-US binational science foundation.

APPENDIX

A. T_{sub} function

The function that relates deep temperature anomalies to the deviation of the thermocline from its mean state is taken to be a modified hyperbolic tangent as in equations (9,10,11) of Munnich et al. (1991), yet fitted to the form of T_{sub} in the CZ model:

$$T_{sub}(h) = \begin{cases} b_+ + \frac{b_+}{a_+}\left\{\tanh\left(\frac{a_+}{b_+}(h^* - h_+)\right) - 1\right\} \\ \quad \text{for } h^* > h_+ \\ h^* \text{ for } h_- < h^* < h_+, \\ -b_- + \frac{b_-}{a_-}\left\{\tanh\left(\frac{a_-}{b_-}\ (h^* - h_-)\right) + 1\right\} \\ \quad \text{for } h^* < h_- \end{cases} \tag{A-1}$$

where $h_+ = b_+(a_+ - 1)/a_+$; $h_- = -b_-(a_- - 1)/a_-$; $h^* = \kappa h$. We also set

$$\begin{aligned} \kappa &= 0.5\left[\frac{b_1 T_1}{\cosh(b_1\overline{H})^2} - \frac{b_2 T_2}{\cosh(b_2\overline{H})^2}\right], \\ b_+ &= T_1(1 - \tanh(b_1\overline{H})), \\ b_- &= T_2(1 - \tanh(b_2\overline{H})), \end{aligned} \tag{A-2}$$

where $T_1 = 28°$, $T_2 = -40°$, $b_1 = (80m)^{-1}$ and $b_2 = (33m)^{-1}$. This parameterization of $T_{sub}(h)$ provides a close approximation to the form used in the CZ model, yet is continuous and has a continuous derivative with respect to h.

B. Derivation of the fast wave model

The fast wave limit neglects the time derivative terms in the ocean momentum equations (1). Our derivation of the fast wave model starts with the equations for the eastward propagating case of Hao et al. (1993). The relation between the wind-stress and the SST is as in (11), where $A(T,x)$ is the solution to the Gill type atmospheric model (Gill 1980), retaining the Kelvin and first Rossby atmospheric modes (Hao et al. 1993),

$$A(T,x) = \frac{1}{2}b_0\varepsilon_a\left[3e^{3\varepsilon_a x}\int_x^{x_e} T(s)e^{-3\varepsilon_a s}ds - e^{-\varepsilon_a x}\int_{x_W}^{x} T(s)e^{\varepsilon_a s}ds\right] \tag{B-1}$$

where ε_a is the nondimensional atmospheric damping. The east-west thermocline tilt in the fast wave limit is taken to be in a balance with the wind stress,

$$C_o^2\rho\partial_x h(x) = \tau(x), \tag{B-2}$$

so that

$$h(x) = h_e - \frac{1}{C_o^2\rho}\int_x^{x_E}\tau(s)ds. \tag{B-3}$$

Following Cane et al. (1990) and Hao et al. (1993), the response of the thermocline at the eastern boundary to wind stress of the form of (11) is taken to be

$$h_e = \frac{1}{C_o^2\rho}\int_{x_W}^{x_E}\tau(s)(\frac{s}{L})^{1/2}ds. \tag{B-4}$$

In Hao et al. (1993), the SST equation includes the effects of upwelling, meridional advection and thermal damping. Furthermore, T_{sub} was used there as a total deep temperature rather than a deep temperature anomaly. We have verified that the nature of the oscillations does not change when the meridional advection term is neglected, the model is changed to an anomaly model, and the mean annual upwelling (which appears in the thermodynamic equation) is taken to be constant throughout the basin. Therefore, we take the thermodynamic equation to be (10), where T_{sub} is modified from Munnich et al. (1991) as given in (A-1).

We divide the basin into two zonal boxes eastern and central pacific, of temperature, wind-stress and thermocline depth (T_e, τ_e, h_e) and (T_c, τ_c, h_c) correspondingly. Eqn (B-1) is solved for T_c and T_e to give

$$\tau_c = \frac{1}{2}\mu_1 b_0\left[B_1 T_c + B_2 T_e\right] \tag{B-5}$$

$$\tau_e = \frac{1}{2}\mu_2 b_0\left[D_1 T_c + D_2 T_e\right] \tag{B-6}$$

$$
\begin{aligned}
B_1 &= -e^{3\varepsilon_a x_c}\left(e^{-3\varepsilon_a x_0} - e^{-3\varepsilon_a x_c}\right) - e^{-\varepsilon_a x_c}\left(e^{\varepsilon_a x_c} - 1\right),\\
B_2 &= -e^{3\varepsilon_a x_c}\left(e^{-3\varepsilon_a} - e^{-3\varepsilon_a x_0}\right),\\
D_1 &= -e^{\varepsilon_a x_e}\left(e^{\varepsilon_a x_0} - 1\right),\\
D_2 &= -e^{3\varepsilon_a x_e}\left(e^{-3\varepsilon_a} - e^{-3\varepsilon_a x_e}\right) - e^{-\varepsilon_a x_e}\left(e^{\varepsilon_a x_e} - e\varepsilon_a x_0\right),
\end{aligned}
\tag{B-7}
$$

where μ_1 and μ_2 represent the seasonal background in the central and eastern boxes respectively, x_0 is the boundary between the two boxes, x_c is the longitude where τ_c and h_c are evaluated, and x_e is the longitude where τ_e and h_e are evaluated. Equations (B-3) and (B-4) are then solved for τ_c and τ_e to give,

$$h_e = \frac{1}{C_o^2 \rho}\left(x_0^2 \tau_c + (1 - x_0)^2 \tau_e\right), \tag{B-8}$$

$$h_c = h_e - \frac{1}{C_o^2 \rho}\left((x_0 - x_c)\tau_c + (1 - x_0)\tau_e\right). \tag{B-9}$$

Using (B-5) and (B-6) in (B-8) and (B-9) respectively we get

$$h_c = h_c(T_c, T_e), \qquad h_e = h_e(T_c, T_e). \tag{B-10}$$

Substituting the above result into (10), we get

$$\partial_t T_c = -\varepsilon_T T_c - \gamma \frac{\overline{w}}{H_1} T_c + \gamma \frac{\overline{w}}{H_1} T_{sub}\left(h_c(T_c, T_e)\right), \tag{B-11}$$

$$\partial_t T_e = -\varepsilon_T T_e - \gamma \frac{\overline{w}}{H_1} T_e + \gamma \frac{\overline{w}}{H_1} T_{sub}\left(h_e(T_c, T_e)\right), \tag{B-12}$$

which form our simplified fast wave model. Table (2) summaries the model parameters used.

Using those parameters and assuming seasonal variations only for the terms that involve T_e (see section b), (B-10) takes the form

$$h_c \propto \frac{7}{4} T_c + \mu T_e, \qquad h_e \propto -\frac{4}{5} T_c + \mu T_e, \tag{B-13}$$

so that h_c depend positively on T_c and T_e, whereas h_e depend negatively on T_c and positively on T_e.

REFERENCES

Battisti, D. S., 1988: The dynamics and thermodynamics of a warming event in a coupled tropical atmosphere/ocean model. *J. Atmos. Sci.*, **45**, 2889–2919.

Battisti, D. S., and A. C. Hirst, 1989: Interannual variability in the tropical atmosphere-ocean system: Influence of the basic state and ocean geometry. *J. Atmos. Sci.*, **45**, 1687–1712.

Cane, M. A., M. Münnich, and S. E. Zebiak, 1990: A Study of Self-Excited Oscillations of the Tropical Ocean-Atmosphere System. Part I: Linear Analysis. *J. Atmos. Sci.*, **47**(13), 1562–1577.

Chang, P., L. Ji, B. Wang, and T. Li, 1995: On the interactions between the seasonal cycle and El Niño-Southern Oscillation in an intermediate coupled ocean-atmosphere model. *J. Atmos. Sci.*, **52**, 2353–2372.

Gill, A. E., 1980: Some simple solutions for heat-induced tropical circulation. *Q. J. R. Meteorol. Soc.*, **106**, 447–462.

Hao, Z., J. D. Neelin, and F. Jin, 1993: Nonlinear air-sea interaction in the fast-wave limit. *J. Climate*, **6**, 1523–1544.

Hirst, A. C., 1986: Unstable and damped equatorial modes in simple coupled ocean-atmosphere models. *J. Atmos. Sci.*, **43**, 606–630.

Jin, F.-F., 1997a: An equatorial ocean recharge paradigm for ENSO. part i: conceptual model. *J. Atmos. Sci.*, **54**, 811–829.

Jin, F.-F., 1997b: An equatorial ocean recharge paradigm for ENSO. part ii: a stripped-down coupled model. *J. Atmos. Sci.*, **54**, 830–847.

Jin, F.-F., and D. Neelin, 1993a: Models of interannual tropical ocean-atmosphere interaction - a unified view. part i: numerical results. *J. Atmos. Sci.*, **50**, 3477–3503.

Jin, F.-F., and D. Neelin, 1993b: Models of interannual tropical ocean-atmosphere interaction - a unified view. part iii: analytical results in fully coupled cases. *J. Atmos. Sci.*, **50**, 3523–3540.

Jin, F.-F., D. Neelin, and M. Ghil, 1994: ENSO on the devil's staircase. *Science*, **264**, 70–72.

Li, and Tianming, 1997: Phase transition of the El Nino-Southern Oscillation: A stationary sst mode. *J. Atmos. Sci.*, **54**, 2872–2887.

Munnich, M., M. A. Cane, and S. E. Zebiak, 1991: A study of self-excited oscillations of the tropical ocean-atmosphere system. *J. Atmos. Sci.*, **48**, 1238–1248.

Neelin, J. D., 1991: The slow sea surface temperature mode and the fast-wave limit: analytic theory for tropical interannual oscillations and and experiments in a hybrid coupled model. *J. Atmos. Sci.*, **48**, 584–605.

Neelin, J. D., and F.-F. Jin, 1993: Models of interannual tropical ocean-atmosphere interaction - a unified view. part ii: analytical results in the weak-coupling limit. *J. Atmos. Sci.*, **50**, 3504–3522.

Neelin, J. D., D. S. Battisti, A. C. Hirst, F.-F. Jin, Y. Wakata, T. Yamagata, and S. Zebiak, 1998: ENSO theory. *Special Joint issue of J. Geophys. Res. Atmospheres and J. Geophys. Res. Oceans*, **103**(C7), 14,261–14,290.

Philander, S. G., 1983: El Niño southern oscillation phenomena. *Nature*, **302**, 295–301.

Picaut, J., F. Masia, and Y. DuPenhoat, 1997: An advective-reflective conceptual model for the oscillatory nature of the ENSO. *Science*, **277**, 663–666.

Rasmusson, E. M., and T. H. Carpenter, 1982: Variations in tropical sea surface temperature and surface wind fields associated with the Southern Oscillation/El Niño. *Mon. Weath. Rev.*, **110**, 354–384.

Suarez, M. J., and P. S. Schopf, 1988: A delayed action oscillator for ENSO. *J. Atmos. Sci.*, **45**, 3283–7.

Tziperman, E., L. Stone, M. A. Cane, and H. Jarosh, 1994: El-nino chaos: Overlapping of resonances between the seasonal cycle and the pacific ocean-atmosphere oscillator. *Science*, **264**(5155), 72–74.

Tziperman, E., M. A. Cane, and S. E. Zebiak, 1995: Irregularity and locking to the seasonal cycle in an ENSO prediction model as explained by the quasi-periodicity route to chaos. *J. Atmos. Sci.*, **52**(3), 293–306.

Tziperman, E., S. E. Zebiak, and M. A. Cane, 1997: Mechanisms of seasonal: ENSO interaction. *J. Atmos. Sci.*, **54**(1), 61–71.

Tziperman, E., M. A. Cane, S. E. Zebiak, Y. Xue, and B. Blumenthal, 1998: Locking of El Nino's peak time to the end of the calendar year in the delayed oscillator picture of ENSO. *J. Climate*, **11**(9), 2191–2199.

Zebiak, S. E., and M. A. Cane, 1987: A model El Niño-Southern Oscillation. *Mon. Weath. Rev.*, **115**, 2262–2278.

Chapter 3:
The equatorial thermocline outcropping - A seasonal control on the tropical Pacific ocean-atmosphere instability strength

ELI GALANTI AND ELI TZIPERMAN

Environmental Sciences, Weizmann Institute, Rehovot 76100, Israel

MATTHEW HARRISON AND ANTONY ROSATI

NOAA/GFDL, Princeton, USA

RALF GIERING

FastOpt, Hamburg, Germany

ZIV SIRKES

Institute of Marine Science, University of Southern Mississippi, Stennis Space Center, Mississippi

ABSTRACT

One of the major factors determining the strength and extent of ENSO events, is the instability state of the equatorial Pacific coupled ocean-atmosphere system and its seasonal variations. This study analyzes the coupled instability in a hybrid coupled model of the Indo-Pacific region, using the adjoint method for sensitivity studies.

It is found that the seasonal changes in the ocean-atmosphere instability strength in the model used here are related to the outcropping of the thermocline in the east equatorial Pacific. From July to December, when the thermocline outcrops over a wide area in the East Pacific, there is a strong surface-thermocline connection and anomalies that arrive as Kelvin waves from the west along the thermocline can reach the surface and affect the SST and thus the coupled system. Conversely, from February to June, when the thermocline outcropping is minimal, the surface decouples from the thermocline and temperature anomalies in the thermocline depth range do not affect the surface and dissipate within the thermocline. The role of vertical mixing rather than upwelling in linking vertical thermocline movements to SST changes is emphasized.

It is therefore suggested that the seasonal ocean-atmosphere instability strength in the equatorial Pacific is strongly influenced by the thermocline outcropping and its seasonal modulation, a physical mechanism that is often neglected in intermediate coupled models and that can be represented properly only in models that employ the full dynamics of the mixed-layer.

---

1. Introduction

One of the major factors determining the strength and extent of ENSO events, is the instability state of the equatorial Pacific ocean-atmosphere system. This instability is determined to a large degree by the ocean-atmosphere "coupling strength" (Cane et al. 1990), so that the instability strength and the coupling strength may be considered alternative measures of the same physical quantity. An unstable state allows the growth of anomalous conditions that can then evolve to become an El Niño event, whereas a stable state causes any perturbation to vanish, forcing the system to stay at its mean seasonal state.

The instability strength in the equatorial Pacific region undergoes seasonal variations (e.g. Battisti and Hirst 1989; Hirst 1986; Philander 1983), along with variations whose time scale range from few years to decades (e.g. Gu and Philander 1995, 1997). Understanding the physical factors determining the strength and the seasonal variability of the coupled instability is an important task because it has implications for both El Nino's predictability (Chen et al. 1995; Moore and Kleeman 1996; Torrence and Webster 1998; Webster and Yang 1992; Weiss and Weiss 1999; Xue et al. 1994), as well as for ENSO's irregularity (Chang et al. 1994; Jin et al. 1994; Tziperman et al. 1994, 1995) and phase locking (Galanti and Tziperman 2000; Tziperman et al. 1998).

Philander (1983) suggested that the key element determining the seasonality of the coupled instability strength is the seasonal movement of the Pacific Inter Tropical Convergence Zone (ITCZ) and its effect on the atmospheric heating. Other seasonal climatological factors that might enhance the coupled ocean-atmosphere instability are large zonal gradients of mean SST, shallow thermocline, strong zonal winds, high SST (Hirst 1986) and strong upwelling (Battisti 1988). Battisti and Hirst (1989) found that setting the basic state in a simplified model to different monthly climatologies affects the rate of anomaly growth. Analyzing separately the effect of each seasonal variable in an intermediate model, Tziperman et al. (1997) suggested that the seasonal wind convergence (i.e. the ITCZ location) and the seasonal climatological SST are the dominant factors in determining the strength of the ocean-atmosphere instability in the Cane-Zebiak model (Zebiak and Cane 1987). All the above works used simplified models, ranging from low-order models to intermediate models such as the CZ-model which lack the ability to explicitly resolve the mixed layer and the thermocline structure.

In this paper we suggest an additional mechanism for the seasonality in the coupled instability strength. We emphasize the role of vertical mixing between the thermocline and the sea surface and show that seasonal changes in the strength of the SST response to thermocline movements is a function of the extent of outcropping of the thermocline in the east equatorial Pacific. That is, we show that from summer to early winter when the thermocline outcrops over a wide area in the East Pacific, there is a strong surface-thermocline connection and anomalies that arrive as Kelvin waves from the west along the thermocline can reach the surface and affect the SST and thus the coupled system. Conversely, from late winter to early spring, when the thermocline outcropping is minimal, the surface decouples from the thermocline and temperature anomalies in the thermocline depth range do not affect the surface and dissipate within the thermocline. We therefore suggest that the seasonal ocean-atmosphere coupling strength is strongly influenced by the seasonality in the thermocline outcropping in the East Pacific.

The results of this work were obtained using the adjoint method for sensitivity studies (e.g Errico and Vukicevic 1992; Giering 1997; Giering and Kaminski 1998; Hall 1986; Marotzke et al. 1999; Moore and Kleeman 1996, 1997; Sirkes and Tziperman 2001; Van-Oldenborgh 2000; Van-Oldenborgh et al. 1999). The adjoint method was applied to a hybrid coupled model of the Indo-Pacific region, that is based on an ocean general circulation model (GCM) coupled to a statistical atmospheric model (e.g Syu et al. 1995). Our results regarding the physics of ENSO, however, do not depend on the particular methodology of sensitivity analysis used here. We have made an effort to present the work in a way that would hopefully be clear to readers with no previous exposure to the adjoint method.

The sensitivity analysis in this paper is arranged and presented as follows. We first describe the hybrid coupled ENSO model, along with the adjoint model that was constructed for the sensitivity studies (section 2), and the design of the sensitivity experiments is presented in section 3. The actual sensitivity analysis begins with section 4, in which we examine the sensitivity of the averaged subsurface thermocline-depth temperature in the East Pacific to processes in the entire equatorial Pacific in an ocean only model. We show that the East Pacific subsurface temperature is sensitive to the thermocline-depth temperature to the west, due to the Kelvin waves that can transmit the signal from the West Pacific to the East Pacific. The purpose of this section is to introduce the reader to the adjoint analysis and to looking at the adjoint model results. Next, in section 5, we consider the sensitivity of the same averaged temperature in the subsurface East Pacific, but in a coupled model. We show that in this case, the sensitivity increases in time, indicating that the coupled ocean-atmosphere amplifies temperature anomalies because of the coupled ocean-atmosphere instability responsible for ENSO's development in our model. The coupled instability acts as follows: subsurface East Pacific temperature anomalies are transmitted to the surface, affect the East Pacific SST and therefore the wind stress in the Central Pacific. The wind stress then creates a temperature signal along the thermocline in the Central Pacific which is transmitted to the East Pacific as Kelvin waves, and amplifies the original signal there. Now, there are two issues to note here: first, the fact that we observe an amplification by the coupled system means that there is a connection between the subsurface and surface temperatures in the East Pacific. This connection is our focus here and is further explored in the following. Second, the instability or amplification by the coupled ocean-atmosphere system is seen here via the adjoint analysis, and we would like to spend a few lines explaining this.

Consider the system

$$\frac{dx}{dt} = \alpha x, \tag{1}$$

where x is a scalar variable, and α is a constant coefficient. Suppose the cost function (the scalar quantity whose sensitivity we are after) is simply some constant β times the model variable x at the final time T

$$J = \beta x(T). \tag{2}$$

The adjoint equation in this case can be shown to be (e.g. Thacker 1987; Tziperman and Thacker 1989)

$$\frac{d\lambda}{dt} = -\alpha\lambda + \beta\delta(t-T), \tag{3}$$

where $\delta(t-T)$ is the Dirac delta function. Note that the adjoint equation starts with zero initial conditions at time T, $\lambda(t=T)=0$, is then forced by the cost function value at that time, and is integrated backward in time, from time T to the initial time $t=0$. Given that the adjoint equation for $\lambda(t)$ is integrated backward in time, its behavior is exactly the same as that of the forward equation: if α is positive, i.e., the model is unstable and x is growing in time, then the adjoint solution λ will also grow backward in time. The behavior of the adjoint solution is therefore a direct measure of the model instability. An adjoint solution that grows backward in time indicates that the model is unstable with regard to the chosen cost function, whereas an adjoint solution that decays backward in time indicates that the model is stable. We will take advantage of this when analyzing the adjoint solution of the coupled model, and examining its stability.

Having observed the coupled instability via the subsurface to surface connection, we next (section 6) examine the same sensitivity of the subsurface east Pacific temperature during a different month, when the thermocline does not outcrop in the East Pacific. We find that in this case the adjoint solution grows less rapidly backward in time, indicating that the forward model is less unstable. We conclude that the subsurface to surface connection in the East Pacific is less strong, because the thermocline does not outcrop, and as a result the coupled instability is weaker. Finally, in section 7, we examine the sensitivity of the SST in the East Pacific to the subsurface temperature, and explicitly examine the role of vertical mixing in order to demonstrate that the seasonality of the thermocline outcropping indeed affects the seasonality in the ocean-atmosphere coupling strength and coupled instability. We conclude in Section 8.

2. The hybrid coupled model

The hybrid coupled model we use is constructed from an ocean GCM coupled to a monthly statistical atmosphere. In the following subsections we describe the different components of the hybrid coupled model.

a. The ocean model

The ocean model is based on the GFDL modular ocean model (MOM) (Pacanowski and Griffies 1999). The model domain is the Indo-Pacific region, 30°E-70°W, and 50°S-50°N. The model resolution is 3° in longitude, 3° going to 1° at the equator in latitude, and 30 depth levels where the top 15 layers are within the top 200 meters of the ocean. The resolution is such that the equatorial dynamics (Kelvin and Rossby waves) are resolved (with a Rossby radius of deformation being roughly 250 km, there are some 5 grid points in latitude to marginally represent the Kelvin Wave structure in latitude over both sides of the equator), while the number of grid points is still small enough to enable many long model runs.

The model uses a modified Richardson-number dependent vertical mixing scheme (Pacanowski and Philander 1981; Syu and Neelin 2000). In addition, a simplified mixed-layer scheme is applied as in Syu and Neelin (2000). Constant horizontal viscosity and diffusivity are used. Sponge layers are used at the North and South horizontal boundaries, restoring the temperature and salinities to the monthly Levitus climatology (Levitus 1982).

The model is spun-up forced by the climatological FSU wind stress (Stricherz et al. 1997; Stricherz and Legler 1992) and climatological heat fluxes (Esbensen and Kushnir 1981). The model is also restored to the climatological monthly NCEP SST (Reynolds and Smith 1994) and to the climatological monthly Levitus SSS (Levitus 1982) with a restoring time of 10 days (for an upper layer thickness of 10 m). After reaching its mean seasonal climate state (50 years of spin-up), the monthly-mean model air-sea heat flux is saved to be used as a flux adjustment term in the coupled run. A weak restoring of the temperature to the climatological SST of the ocean model during the spin-up, with a time scale of 100 days, is applied during the coupled model run. The monthly temperature climatology of the coupled model is similar to the Levitus climatology (Levitus 1982).

b. Statistical atmospheric model

The statistical atmospheric model is based on that of Harrison et al. (2002) (HAR) (see also (Syu et al. 1995)), using the NCEP SST (Reynolds and Smith 1994), and the wind stress and heat fluxes of the ECMWF re-analysis (Gibson et al. 1997). The atmospheric model is constructed by finding the best correlated patterns of the two data sets (SST anomalies vs. atmospheric anomalies) using an SVD decomposition of the cross-covariance matrix of the SST and the atmospheric variables (e.g. Syu et al. 1995). The first few singular vectors are then used to predict the wind stress and heat flux anomalies based on the model SST anomalies. HAR have shown that only the first two or three singular vectors should be used; the use of higher modes could introduce an un-physical relatively large scale noise into the model. We chose to use the first three SVD modes. The coupling of the atmospheric variables to the anomalous SST (see details below) is done only between 20°S and 20°N. This choice was made in order to avoid spurious tropical extra-tropical teleconnections that may occur due to the fact that the atmospheric model is derived from only 15 years of data. It is known that different flux products that are used to derive statistical atmospheric models result sometimes in self-sustained and sometimes in damped variability (HAR). In this model we do not use an artificially enhanced (stronger) coupling coefficient, and the coupling is therefore not artificially tuned to result in self-sustained oscillations. Also, we are not using (see end of section a) a strong restoring heat flux in addition to the heat flux calculated by the statistical atmosphere when running the coupled model. This allows for thermal anomalies to exist and evolve more freely.

Note that the resulting estimate of the atmospheric forcing fields does not account for high frequency variability (i.e. frequencies higher than one month) and for wind stress anomalies induced by mid-latitude teleconnections. Also note that the RMS variability of the atmospheric anomalous response in our model will be smaller than the observed one since we exclude the energy contained in the higher SVD modes, being interested in the large-scale low frequency dynamics.

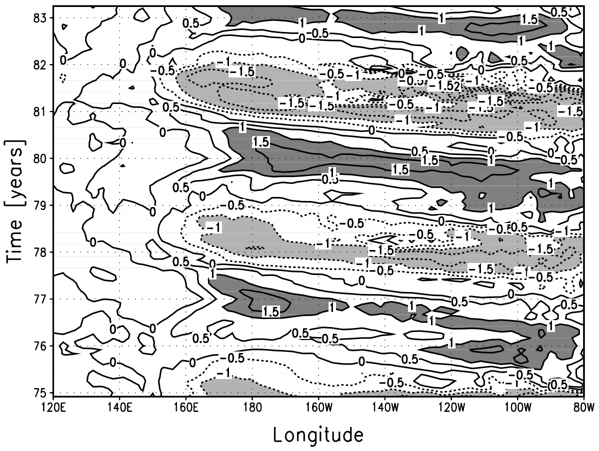

FIG. 1. The hybrid coupled model temperature anomalies along the equator, averaged from 5S to 5N, as function of time. Values larger (smaller) than 1.0° C ($-1.0°$ C) are shaded with dark (light) gray.

c. The hybrid coupled model

The coupled model is run as follows: at each time step, the SST anomalies are calculated with respect to the monthly climatological SST of the uncoupled ocean model. Next, the wind stress and heat flux anomalies are derived from the SST anomalies using the statistical atmospheric model. Finally, the calculated wind stress and heat flux anomalies are added to the monthly climatological FSU wind stress and to the climatological model heat flux, respectively, to be used as forcing for the ocean model.

The model exhibits interannual variability similar to, although weaker than, the observed ENSO variability (Fig. 1). The SST anomalies are mainly in the east and central Pacific, the oscillation time scale is of 3-4 years and the maximum of the warm events is reached during November-December, in a reasonable agreement with observations. Note that the model oscillations are more regular than the observed, and that the interannual variance in the central Pacific is similar to that in the eastern Pacific, while in the observations it is smaller. Also note that the La Niña events are slightly stronger than the El Niño events, which may indicate that the nonlinearity dominant in the model is not identical to that in reality.

d. The adjoint model

An adjoint model for the hybrid coupled model was derived with the help of the Tangent linear and Adjoint Model Compiler (Giering 1997; Giering and Kaminski 1998; Marotzke et al. 1999). This compiler derives an adjoint code for a given Fortran code, provided that the compiler can recognize all the structures and syntax of the original code.

Many changes were made to MOM to make it more consistent with the adjoint compiler. In addition, a set of PERL scripts were developed to convert structures in the MOM code that the compiler could not handle. Those include most of the Fortran 90 code and some Fortran 77 commands. In order to verify the adjoint code, its solution was compared at each grid point to a finite difference estimate of the derivative of the cost function. For an appropriately small amplitude perturbation to the initial conditions, the finite difference gradient of the cost function was found to converge to the adjoint solution, up to the truncation error.

3. Sensitivity analysis methodology

Two factors determine the physical context of our sensitivity experiments: the first is the formulation of the cost function, and the second is the choice of the control variables. The cost function is the index (a scalar) whose sensitivity is studied with respect to changes in the control variables. We start this section with a brief review of the adjoint method for sensitivity studies, followed by a detailed description of the specific experiments we carried out.

a. Sensitivity studies - general formulation

Let us denote the model initial conditions by a vector $\mathbf{X}_{init}$. These initial conditions can be any combination of the model variables (temperature, salinity, currents, etc.). The initial conditions, also referred to here as "control variables", are then propagated in time by the model equations which we denote here by an operator $\mathbf{L}_\tau$, so that

$$\mathbf{X}_{final} = \mathbf{L}_\tau(\mathbf{X}_{init}), \tag{4}$$

where the vector $\mathbf{X}_{final}$ is the final state of the model, and τ is the time interval over which the model was integrated. The next stage is to define a scalar "cost function" from the model solution, possibly based on the solution at several time steps. The cost function is usually a measure of a model characteristic we would like to study; in our case it will be a measure of the amplitude of ENSO. Let the cost function, as a function of the final model state, be

$$J = J(\mathbf{X}_{final}), \tag{5}$$

and since the final state depends on the initial one, we can also write

$$J = J(\mathbf{X}_{init}). \tag{6}$$

We now ask the following question: what would be the sensitivity of the cost function J to perturbation in the kth control variables x^k_{init} (note that the index k stands for different spatial locations as well as for different physical variables such as temperature, currents, etc.). The sensitivity is simply the derivative, so that

$$\lambda^k = \frac{\partial J}{\partial x^k_{init}}, \tag{7}$$

where λ^k denotes the derivative of the cost function with respect to the kth control variable, or in other words, λ^k is the sensitivity of the cost function to the kth control variable.

To compute the sensitivity λ^k one could run the model once without any perturbation and once with a small perturbation δx in the kth control variables, and estimate the cost function gradient by

$$\lambda^k_{es} = \frac{J(x^k_{init} = x^k_0 + \delta x) - J(x^k_{init} = x^k_0)}{\delta x}, \tag{8}$$

where λ^k_{es} is the estimated finite difference approximation to the gradient of the cost function with respect to the kth control variable, and x^k_0 is the kth control variable without perturbation. One would then have to run the model again for each control variable in order to get the full vector of sensitivities. That is, of course, an impractical procedure when dealing with complicated 3D models with $O(10^6)$ initial conditions (control variables) such as our hybrid coupled model. The adjoint method enables us to compute all the sensitivities $\lambda^k, k = 1, ..., K$ by running the forward (physical) model once, and then its adjoint model only once (computationally equivalent to about 4 runs of the physical model). The adjoint model runs backward in time, from the time of the cost function evaluation to the time of the initial conditions; in other words, it propagates the sensitivity backward, from the effect to the cause. It computes not only the sensitivities to the control variables at the initial time, but also the sensitivities at all intermediate time intervals until the time at which the cost function is evaluated.

In order to obtain a feeling for the physical contents of the adjoint model solution, consider a (rigid lid) two layer equatorial ocean model in which baroclinic Kelvin waves exist, so that any perturbation to the model variables propagates eastward as equatorial Kelvin waves. Defining the cost function to be the upper layer depth at some location along the equator, the adjoint model solution will be the sensitivity of the upper layer depth at the chosen location to perturbations in all model variables at previous times. Since the model allows for eastward-propagating Kelvin waves to exist, the cost function would be sensitive to Kelvin waves that were excited west of the location of the cost function, at a time interval that is exactly the time it takes the Kelvin wave to reach the location where the cost function is evaluated. The adjoint model, running backward in time, will manifest this sensitivity in the shape of an adjoint Kelvin wave that propagates westward from the location of the cost function evaluation to the distance that an actual Kelvin wave would have propagated during the same time interval.

It is important to remember that the adjoint sensitivities are based on the model tangent-linearization and therefore represent the sensitivity to infinitesimal perturbations. Any nonlinearity (such as the Richardson number vertical mixing scheme) will affect the accuracy of the sensitivity to larger amplitude perturbations.

b. Formulation of the cost function

The cost function we use focuses on the temperature variability in the East Pacific. The largest amplitude interannual temperature variability observed in the equatorial Pacific (as well as in our model) is located near 100W at a depth of about 60 meters. Fig. 2 shows the root mean square (RMS) of the coupled model interannual temperature variability along the equator (averaged over 5°S-5°N). Two main features can be seen: the first is the large amplitude variability in the east that is due to the El Niño and La Niña signal, and the second is located just beneath the warm pool due to a signal of opposite sign to that of the East Pacific SST; that feature is formed during the mature phase of the El Niño /La Niña event and is the negative feedback that later on propagates to the east and terminates the event. The NINO3 index is the surface manifestation of the first feature. For example, an SST anomaly at the peak time of ENSO of 3°C, corresponds to a temperature anomaly at depth of 60m of about 9°C at 100W (these temperature differences are true also for the observed ENSO).

As will be seen below, our sensitivity experiments mostly need to be based on a cost function that focuses on the region of largest variability. We therefore set the cost function to be a summation of temperature, weighted toward the regions of maximum RMS temperature variability in the East Pacific (Fig. 2). The cost function also sums the temperature over a short time interval around a time t_{max}, with a Gaussian-like weight that has a time scale of $\Delta T = 10 days$ days, so that the cost function has contributions from the temperature at a range of times around t_{max}. This results in a smoother sensitivity signal; the cost function serves as forcing to the adjoint model, and therefore needs to be smooth in both space and time. The cost function is therefore,

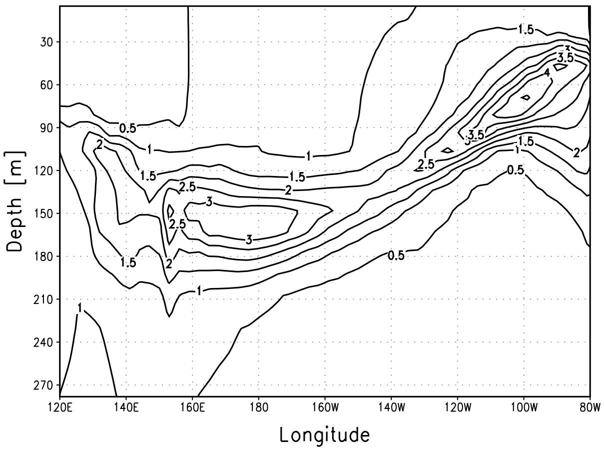

FIG. 2. RMS of the interannual variability of temperature in the model, averaged from 5S to 5N.

$$\mathbf{J} = \sum_{i,j,k,n} W^{space}_{i,j,k} W^{time}_{n} T_{i,j,k,n} \tag{9}$$

$$W^{space}_{i,j,k} = exp\left[-\left(\frac{x_i - x_{max}}{\Delta X}\right)^2\right]$$
$$\cdot exp\left[-\left(\frac{y_j - y_{max}}{\Delta Y}\right)^2\right]\cdot exp\left[-\left(\frac{z_k - z_{max}}{\Delta Z}\right)^2\right] \tag{10}$$

$$W^{time}_{n} = exp\left[-\left(\frac{t_n - t_{max}}{\Delta T}\right)^2\right] \tag{11}$$

where $x_{max} = 100W, y_{max} = 0, z_{max} = 60m$ is the location of maximum weight, $\Delta X = 3000km, \Delta Y = 300km, \Delta Z = 40m$ are scales similar to those of the model maximum temperature RMS signal (Fig. 2), and x_i, y_j, z_k, t_n are the model coordinates. The connection between anomalies at the ocean surface and anomalies at the depth of the thermocline will be studied in section 7, using a modified cost function. Note that in sensitivity studies such as here, in contrast to cases where the adjoint model is used for calculating optimal initial conditions (Farrell 1988; Kleeman and Moore 1997; Penland and Sardeshmukh 1995), the cost function need not be quadratic and may be any function, linear or not, of the model state.

c. Choice of the control variables

The control variables $\mathbf{X}_{init}$ are all the initial prognostic variables, that is, temperature, salinity, currents, and surface height. In addition, one may examine the sensitivity to diagnostic and other intermediate model variables such as the wind stress etc, that are also calculated by the adjoint model. Although the definition of the adjoint sensitivities (7) is straight forward, there are still some issues to consider when analyzing the results.

First, it is important to understand that the adjoint sensitivity reflects the effect of a perturbation in a specific place and time on the cost function. A high sensitivity doesn't mean that the actual probability for such a perturbation to occur is high. Second, one necessary measure to be taken before analyzing the adjoint solution is a normalization of all adjoint sensitivities by the volume of the model grid they represent. This compensates for the fact that the model grid is not uniform. A temperature perturbation in a deep grid box corresponds to a larger energy perturbation than the same temperature perturbation in a surface grid box, simply because the grid box size is larger at depth. The adjoint solution therefore biases the sensitivities toward the large volume boxes, so that when analyzing the adjoint solution, this bias needs to be properly compensated for (Marotzke et al. 1999). All adjoint sensitivities appearing in this work are normalized by the volume of the box they represent, in such a way that the surface variables at the equator (smallest box volume) are normalized by a factor of one. The normalization of the adjoint solution is done only when displaying and analyzing the results, and not during the adjoint model integration.

4. Sensitivities in the ocean-only model

In this section we study the adjoint sensitivities in an ocean only model. This will set the stage for the investigation of the ocean-atmosphere coupling and its dependence on the seasonality of the thermocline outcropping in the later sections. For this purpose, we ran the coupled model with the coupling to the statistical atmosphere turned off, i.e. the SST anomalies do not affect the winds and heat fluxes and no interannual variability exists. These experiments therefore examine the free ocean dynamics. The forward model was run for one year (January to December) from its climatological state, so that the adjoint model is integrated backward in time for one year with the model climatology as the background state; note that the model climatology will be used as the background state troughout the paper. The cost function (9) is calculated with t_{max} set to the middle of December, and the adjoint model is then run accordingly from December to January. This experiment will be referred to as *ocean-December* (Table 1).

Experiment	Ocean-Atmos coupling	t_{max}	Figures
ocean-December	no	December 15	Figs. 3-4
coupled-December	yes*	December 15	Figs. 5- 6
ocean-June	no	June 15	Fig. 7
coupled-June	yes*	June 15	Fig. 8
Surface-December	no	December 15	Fig. 9
Surface-June	no	June 15	Fig. 10

TABLE 1. List of sensitivity experiments. *Statistical atmospheric model is set to perpetual January.

Fig. 3 shows the monthly averaged sensitivity of the cost function to temperature perturbations along the equator at 1,3,5 and 7 months prior to the time of the cost function evaluation. For reference we plot the 18° and 26° isotherms (which span the main thermocline temperature range) of the forward model climatology at the same months in which the sensitivities are displayed. The upper panel of Fig. 3 shows the sensitivity of the cost function, that is centered around December 15, to perturbations in the temperature field in November, i.e. one month prior to the time of the cost function. These sensitivities indicate the relative effect on the cost function of temperature perturbations made at different locations during November. E.g., we see from the figure that a temperature perturbation made in November at a depth of 90 meters at longitude of 120W would be about 6 times more effective in changing the cost function one month later than the same perturbation applied to the temperature field at a depth of 90 meters at the dateline. The next panel shows the sensitivity of the same cost function to temperature perturbations in September, i.e., 3 months prior to the time of cost evaluation.

The sensitivities are seen in Fig. 3 to propagate westward as an adjoint second baroclinic Kelvin wave (see section a above and Philander (1990); Van-Oldenborgh et al. (1999)). The vertical structure of the sensitivity to perturbations in the zonal velocity (Fig. 4), with positive sensitivity above the thermocline, negative beneath it, and again positive sensitivity at larger depths (below the plotted depth range), reflects the vertical profile of the second baroclinic Kelvin wave. The adjoint Kelvin wave is seen to propagate from around 120W in Fig. 4a, to around 160E in Fig. 4b. Yet the sensitivity signal is not only due to the above adjoint Kelvin wave. Some of the sensitivity signal reaches the western boundary

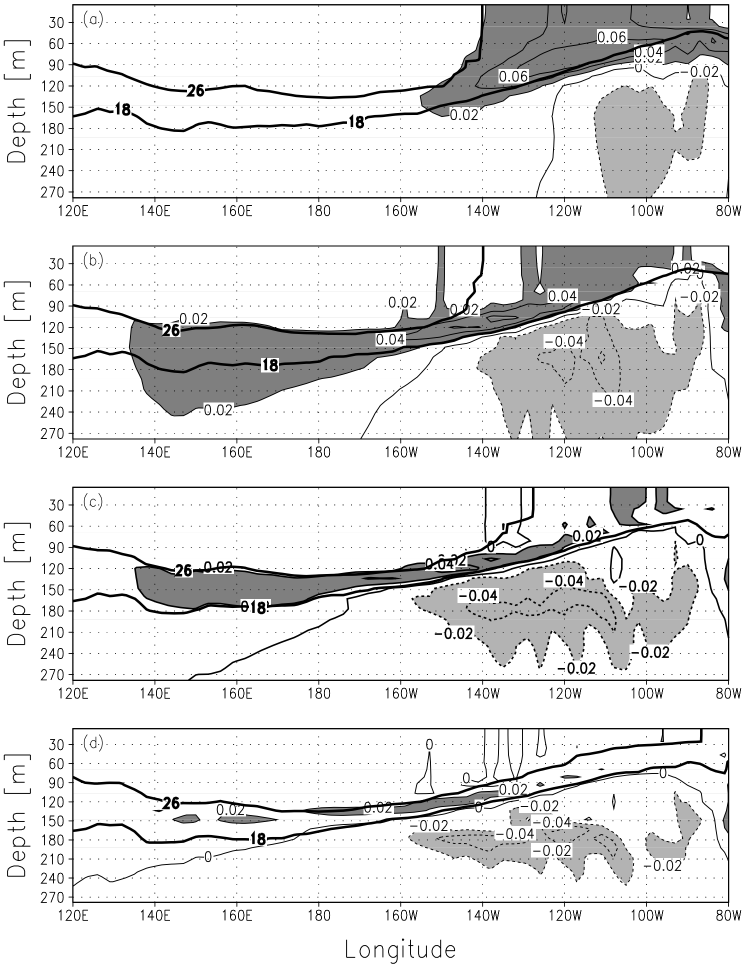

FIG. 3. The cost function sensitivity to temperature perturbations (units are dimensionless) along the equator in the *ocean-December* experiment, as function of longitude and depth. The sensitivities are for (a) November, (b) September, (c) July and (d) May, which are 1,3,5 and 7 months prior to the time of the cost function evaluation. Values larger (smaller) than 0.02 (−0.02) are shaded with dark (light) gray.

after 3 months, as expected from an equatorial adjoint Kelvin wave, but there is also a different sensitivity feature that is limited vertically to the thermocline depth range between the 18° and 26°, and which propagates much slower in time between 170W and 140W. This feature may be a manifestation of some other physical processes, such as advection or higher baroclinic modes, yet it is not relevant to our main aim here.

The negative temperature sensitivity beneath the thermocline and positive sensitivity at and above the thermocline depth range appear in all sensitivity experiments presented here, and are simply a manifestation of the second baroclinic mode structure of the sensitivity signal. The cost function in our model is sensitive to perturbations that have the vertical structure of the second baroclinic mode, hence the structure of the adjoint solution for the sensitivity. Note that both the positive and negative sensitivity signals are part of the same baroclinic structure that is of interest to us here. Higher baroclinic modes will clearly also consist of alternating positive and negative signals. Note also that the sign of the sensitivities in Fig. 3 depends on the formulation of the cost function. As the adjoint model is based on a tangent-linearization of the full model, the same cost function multiplied by minus one generates exactly the same sensitivities, but with an opposite sign.

The adjoint Kelvin wave temperature sensitivity signal is reflected as eastward propagating off-equatorial adjoint Rossby waves upon reaching the western boundary. These are not shown as our focus in this work is on

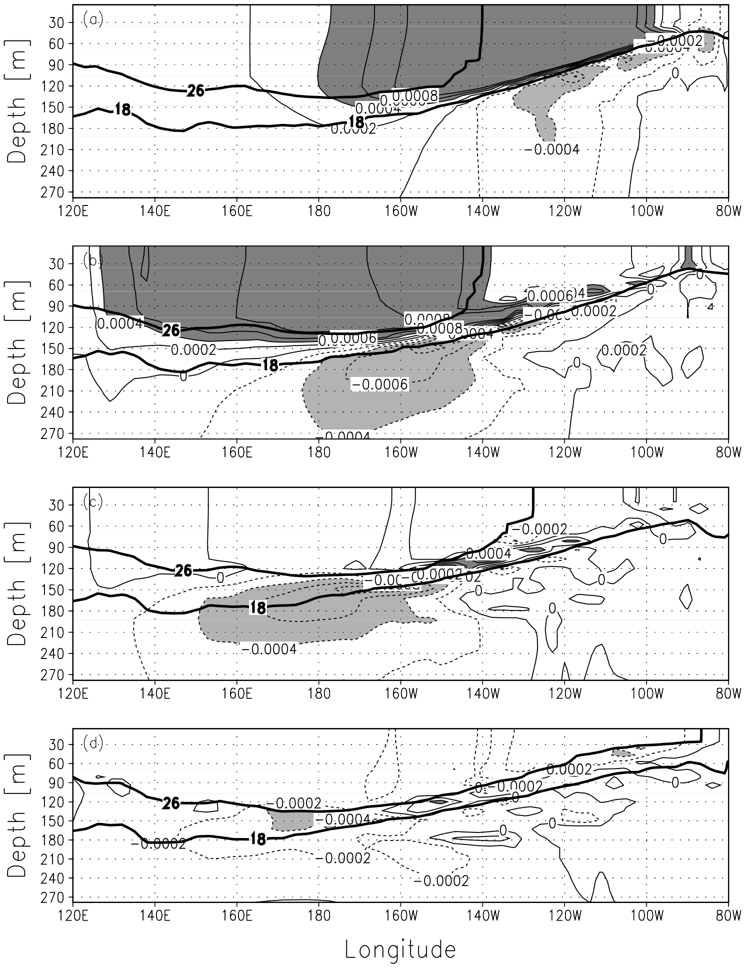

FIG. 4. Same as Fig. 3, but for the sensitivity to the zonal velocity (units are K/(m/sec)). Values larger (smaller) than 0.0004 (−0.0004) are shaded with dark (light) gray.

the equatorial region and on a time scale of 1-7 months only. We now proceed to investigate the sensitivities in the coupled model.

5. Sensitivities in the coupled model

We ran the standard coupled model and its adjoint with t_{max} set again to middle of December. The results of the coupled model sensitivity experiment presented in this section are central to our objective. As explained in the introduction, the adjoint solution is a direct measure of the model instability. An adjoint solution that grows backward in time indicates that the background state of the forward model is unstable to small perturbations. We expect to see such an instability in our model because our coupled model displays self-sustained variability. The self-sustained variability develops due to the fact that the seasonal background is unstable to small perturbations. If the forward coupled model were in a stable (damped) regime where small perturbations decay back to the seasonal background state, then the adjoint solution would also be decaying backward in time.

The couple model was run with the statistical atmospheric model set to perpetual January. This was done in order to isolate the effect of the thermocline outcropping on the seasonal instability strength, from the possible seasonal atmospheric influences. Fig. 5 shows the sensitivity of the cost function to perturbations in the temperature field, as function of longitude and depth, at different time intervals from the central time of the cost function evaluation, t_{max}, (11). This experiment will be referred to as *coupled-December* (Table 1). It can be clearly seen that the sensitivity in the coupled model is much larger than in the *ocean-December* experiment. Furthermore, the sensitivities grow backward in time (that is, downward along the panels of Fig. 5) due to the amplification by the coupled ocean-atmosphere instability responsible for the self-sustained ENSO events in the forward model. The figure shows that the source of the sensitivity signal seems to be at the surface in the East Pacific, as anticipated from the coupled instability mechanism explained in the introduction. Once the sensitivities are amplified by the coupled ocean-atmosphere instability, they propagate in the ocean as in the *ocean-December* experiment.

We can now use the results of this experiment together with those from section 4 to study the effect of the ocean-atmosphere coupling on the sensitivities. As the adjoint model is linear we can subtract the results of the *ocean-December* experiment from those of the *coupled-December* experiment (Fig. 6), thus isolating the role of the coupling. The growth of the sensitivities in time is especially evident in this plot. The time scale at which the coupled sensitivities grow is of the order of 6 months; at that time the sensitivities start to propagate westward along the thermocline. This time scale is partly a result of the time scale of the connection between the surface and the thermocline, which will be discussed in section 7.

The important lesson from this experiment is that the coupled ocean-atmosphere instability strongly amplifies the sensitivity of the East Pacific temperature evaluated at December to perturbation in previous months. We note at this stage that during the months July to December the thermocline as indicated by the 18 and 26 degree contours outcrops over a wide region in the East Pacific, and we now proceed to examine the sensitivity of the East Pacific temperature evaluated during other months.

6. The thermocline outcropping and the seasonality of the coupled instability strength

So far we have analyzed the sensitivities of the averaged East Pacific temperature during December (i.e. the cost function was evaluated in December). In this section we finally get to the main point of this paper, and examine whether there are differences between sensitivities of our cost function when it is evaluated at different times of the year. To address this issue we repeat the ocean only and coupled model sensitivity experiments of sections 4 and 5, with the cost function now centered in June rather than in December. The forward model is therefore run for one year from July to June, and the adjoint model is run backward in time over the same period. These experiments will be referred to as *ocean-June* and *coupled-June*, respectively (Table 1). In the *coupled-June* experiment, the statistical atmospheric model is set to perpetual January, as was done in the *coupled-December* experiment above.

We first consider the ocean-only experiment (*ocean-June*, Fig. 7). In general, the evolution of the sensitivities is similar to those of the *ocean-December* experiment (Fig. 3), with some small differences in the dissipation rate and the propagation speed. The sensitivity to temperature perturbations in the *ocean-December* experiment is somewhat stronger than that in the *ocean-June* experiment during the first 3 months, yet the overall behavior is similar. The overall similarity between the *ocean-December* and the *ocean-June* experiments suggests that the propagation of perturbations within the subsurface water is only mildly influenced by the seasonal changes of the tropical Pacific ocean-atmosphere system. Thus, the pronounced seasonal behavior of the ocean-atmosphere instability strength must be a result of another characteristic of the system.

We now examine the *coupled-June* experiment. We use the fact that the adjoint sensitivity analysis is linear, and subtract the *ocean-June* results from the *coupled-June* results to obtain the sensitivity due to the coupling only (Fig. 8). Comparing this experiment to the *coupled-December* experiment (Fig. 6) shows some significant differences. The sensitivities in the *coupled-June* experiment are weaker than those of the *coupled-December* experiment. Within the time interval of the 3 months prior to the cost evaluation, only minor differences can be seen, both in the sensitivity to temperature perturbations (compare Figs. 8 and 6) and to zonal current perturbations (not shown). Pronounced differences appear in the time interval of 5 to 7 months, where the *coupled-December* experiment shows sensitivities that are two times stronger than the *coupled-June* experiment. For example, at seven months prior to the cost evaluation, the sensitivity at 130W at depth of 50 meters is more than 0.07 in the *coupled-December* experiment, whereas in the *coupled-June* experiment it is about 0.03. The question, of course, is what causes this difference in sensitivities (which reflect difference in the coupled ocean-atmosphere instability strength) of the subsurface East Pacific temperature during December and June.

The main massage of this paper is that the difference in the sensitivity between the December and June coupled sensitivity runs is a result of the outcropping location of the 26° isotherm, or in other words, the instability strength is strongly influenced by the outcropping of the thermocline in the East Pacific. In the *coupled-December* experiment, the outcropping area of the thermocline is initially very wide (the 26° isotherm surfaces in December around 140W so that the thermocline outcropping is from 140W to 80W, Fig. 6a), enabling the subsurface temperature anomalies that propagate along

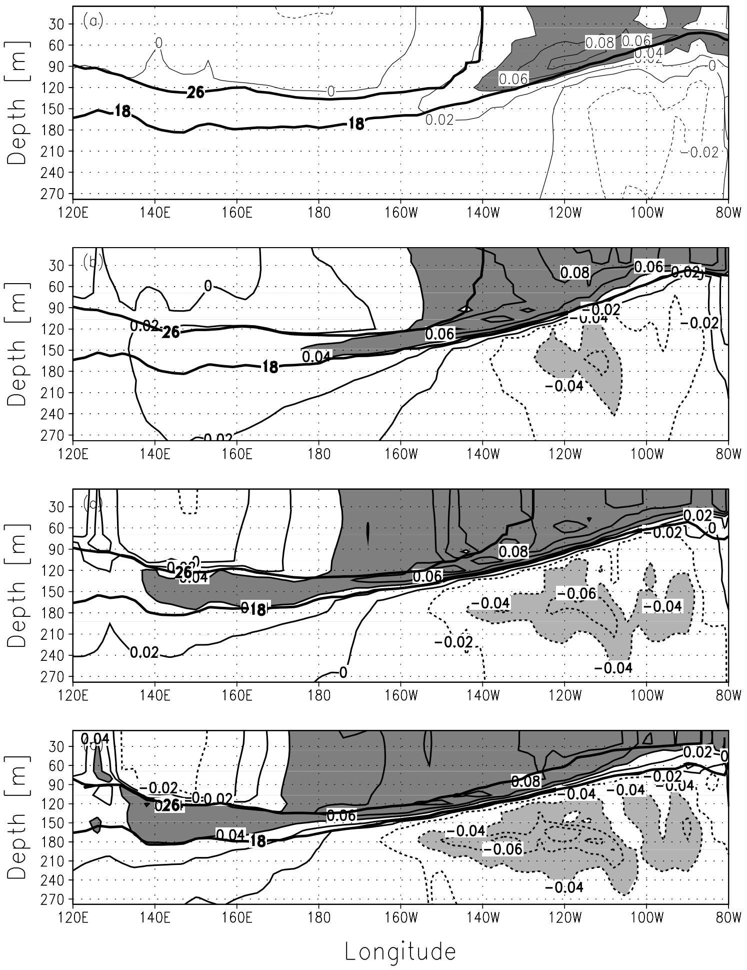

FIG. 5. Same as Fig. 3, but for the *coupled-December* experiment, where the coupled model was run with the statistical atmosphere set to perpetual January. Values larger (smaller) than 0.04 (−0.04) are shaded with dark (light) gray.

the thermocline to reach the surface, affect the atmosphere, and be amplified by the coupled instability. In contrast, in the *ocean-June* experiment the outcropping area of the thermocline is initially very narrow (the 26° isotherm surfaced in June only east of 70W so that there is practically no outcropping (Fig. 8a), resulting in a very small area where the subsurface temperature anomalies can reach the surface. In other words, the warm surface water and strong upper ocean stratification in the spring time decouples the surface from the thermocline, thus preventing sensitivities from entering the thermocline and propagating westward. Only in January are the surface temperature anomalies able to penetrate the mixed layer. As a result, the coupled sensitivities in the *coupled-June* experiment develop much later than those in the *coupled-December* experiment. The time window for the anomalies to develop is approximately from August to January, which is the time when the thermocline outcrops in the East Pacific.

The physical mechanism behind the difference between the adjoint sensitivities in the *coupled-December* case and those of the *coupled-June* case is the following: during the growth phase of ENSO, a warm (thermocline-deepening) signal arrives in the east along the thermocline. When the warm signal reaches the east, its degree of influence on the surface (SST) depends on the exposure of the thermocline at the surface; A thermocline deepening signal that arrives to the East Pacific in spring time is decoupled from the surface due to the strong stratification between the surface and the thermocline; a warm signal that arrives in fall affects the surface substantially, as the thermocline is then exposed to the surface and any deepening of the thermocline immediately affects the heat balance of the surface water and

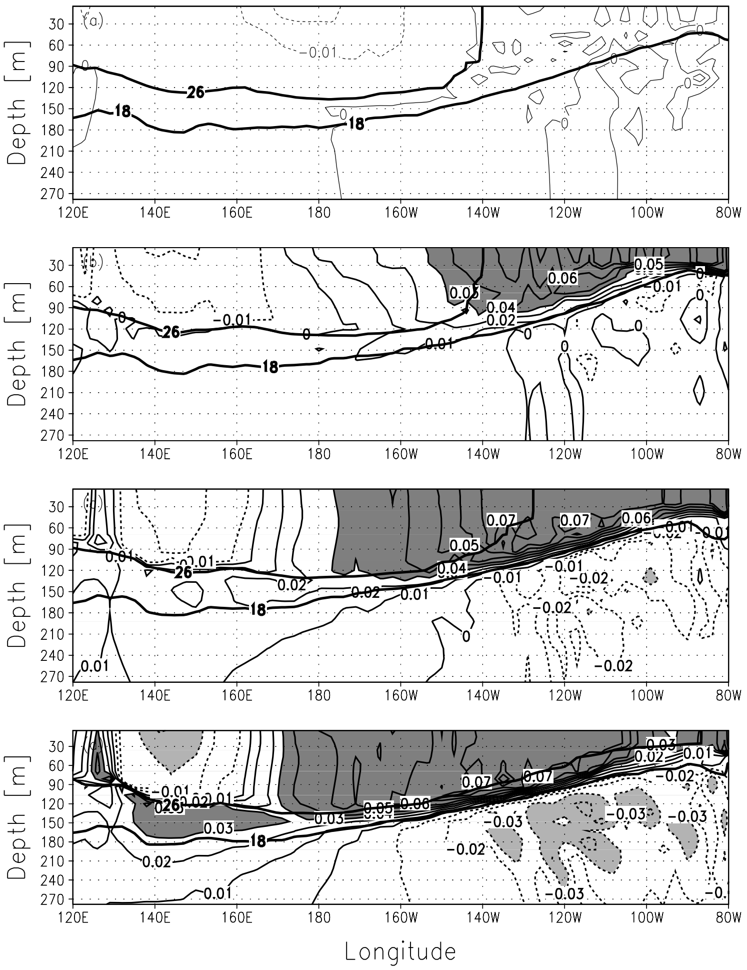

FIG. 6. Same as Fig. 3, but for the difference between the coupled model (*coupled-December* experiment) sensitivities and those of the ocean-only case (*ocean-December* experiment). Values larger (smaller) than 0.03 (-0.03) are shaded with dark (light) gray. Note that the contour levels are different from those of Fig. 3.

hence the SST. The above discussion could be extended to the different phases of ENSO as well, due to the different depth of the thermocline in the East Pacific at different ENSO phases. It has been shown by Van-Oldenborgh et al. (1999) that the sensitivities calculated over different climatologies (the years 1987 and 1988) are very different. The difference in the climatology in their case was between an El Niño event and a La Niña event, still the physical mechanism responsible for the difference may be similar to the one presented here: during the mature phase of an El Niño event the thermocline is buried deep under warm surface layers, and to a large extent is decoupled from the subsurface, whereas during the first stage of the event the surface is much more connected to the subsurface and therefore the event can grow.

The cost function we use is based on the temperature within the subsurface thermocline depth range, therefore at short time intervals (1-3 months) the thermocline outcropping is not dominating the propagation of the sensitivities. However, at longer time intervals (more then 3 months), the coupling between the ocean and the atmosphere makes the thermocline outcropping a dominant factor in the ability of sensitivities to develop and be amplified. The sensitivities to perturbations in the subsurface temperature propagate westward where they create current sensitivities, which in turn create wind stress sensitivities. The wind stress sensitivities generate SST sensitivities in the East Pacific, and these penetrate to the thermocline as a function of the thermocline outcropping. We remind the reader that this “adjoint” scenario is the opposite of what happens in the forward model, where the SST anomalies excite the wind anomalies that

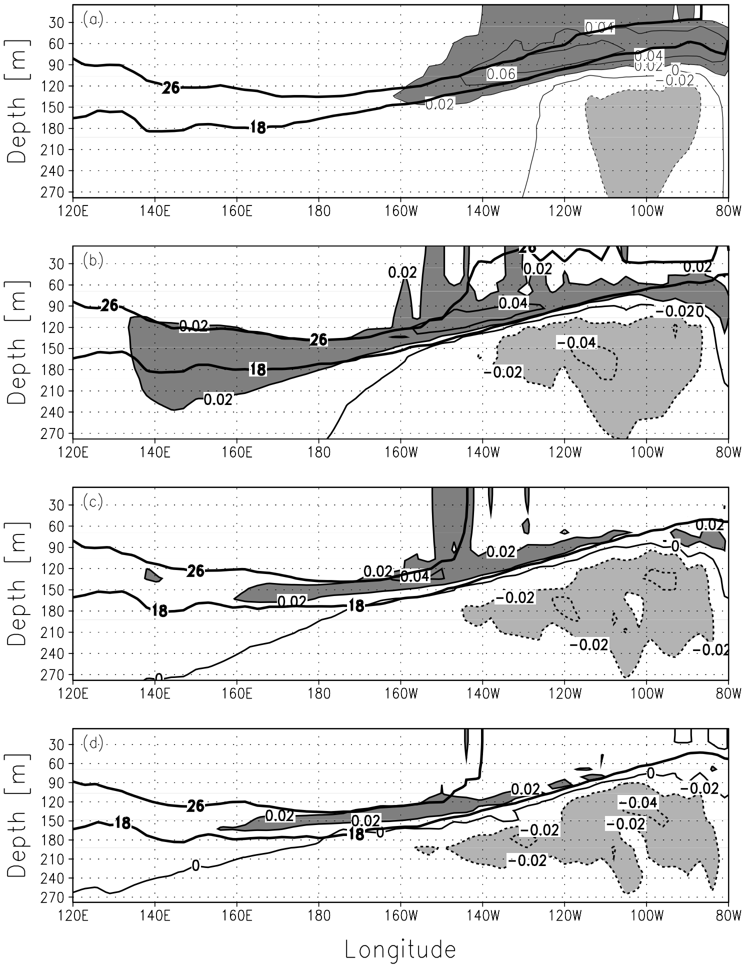

FIG. 7. The cost function (centered in June) sensitivity to temperature perturbations in the *ocean-June* experiment, as function of longitude and depth. The sensitivities are for (a) May, (b) March, (c) January and (d) December, which are 1,3,5 and 7 months prior to the time of the cost function evaluation. Values larger (smaller) than 0.02 (-0.02) are shaded with dark (light) gray.

in turn excite Kelvin waves that propagate eastward and affect the SST in the East Pacific; while the actual physical mechanism propagates from the *cause* to the *effect*, the sensitivities calculated by the adjoint model propagate from the *effect* to the *cause*.

7. The Surface-thermocline connection

In order to clarify the role of the thermocline outcropping in determining the connection between the surface and the subsurface water, we conducted the following experiment: a cost function was set up to focus on the surface temperature at the equator at 120W. We use the same cost function formulation of (9), but with $x_{max} = 120W, y_{max} = 0, z_{max} = 5m$ and $\Delta X = 500km, \Delta Y = 200km, \Delta Z = 1m$. This spatial weighting puts the focus on the sea surface temperature along the equator at 120W. The cost function time-window was reduced to $\Delta T = 1day$ to enable shorter time scales to be resolved. The coupling to the statistical atmosphere was turned off so that all ocean-atmosphere coupling effects were excluded. This experiment will be referred to as *surface-December* (Table 1). Fig. 9 shows the sensitivity of the cost function to temperature perturbations 15, 30, 45 and 60 days prior to the time of the cost function evaluation. At times of up to one month prior to the cost function evaluation time, the sensitivities remain within the region of the mixed layer, not able to penetrate the thermocline region. Only after about 45 days, do the sensitivities enter the thermocline depth range and propagate westward. The separation of the propagating feature (adjoint Kelvin wave) from other sensitivities, can be seen clearly after 30 days. The time scale of the surface to thermocline link is important to the

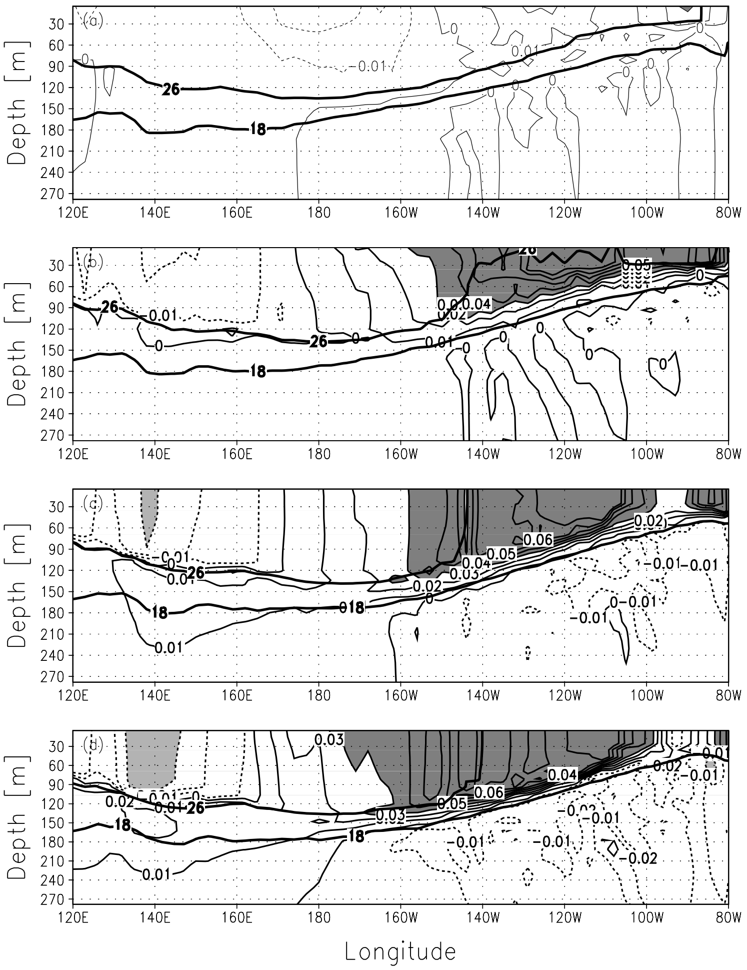

FIG. 8. Same as Fig. 7, but for the difference between the coupled model (*coupled-June* experiment) sensitivities and those of the ocean-only case (*ocean-June* experiment). Contour levels are the same as in Fig. 6. Values larger (smaller) than 0.03 (−0.03) are shaded with dark (light) gray.

ENSO dynamics and has been explored in detail by Jin and Neelin (1993) who studied the differences between the mixed-mode regime that includes the time scale of the surface to thermocline connection, and the fast SST regime that assumes an instantaneous adjustment of the SST to thermocline depth anomalies.

Next, we ran the same experiment but with the surface-centered cost function calculated in June (experiment *surface-June*, see Table 1, Fig. 10). The 26° isotherm now outcrops only at the eastern boundary, decoupling the surface from the thermocline. The sensitivities cannot penetrate the thermocline region and therefore are forced to remain in the mixed layer only. Some of the signal does propagate westward, thus creating a non local sensitivity. But the propagation is above the thermocline depth range and not within it, indicating that the sensitivity is not due to the same baroclinic mode wave propagation seen above. The sensitivity to the zonal velocity (not shown) is also weaker than in the *surface-December* experiment, indicating that the cost function in the *surface-June* experiment is less sensitive to Kelvin waves than the cost function in the *surface-December* experiment. This is a result of the inability of the sensitivities to penetrate the thermocline.

We now turn to look at the above two surface-centered sensitivity experiments after 5 months, in the warm pool area (Fig. 11). The difference is striking, the *surface-December* experiment shows sensitivities that are about 4 times larger than those of the *surface-June* experiment. The June sensitivities that concentrated above the thermocline at time scales of 1-2 months, dissipated due to the strong mixing within the mixed layer, while those

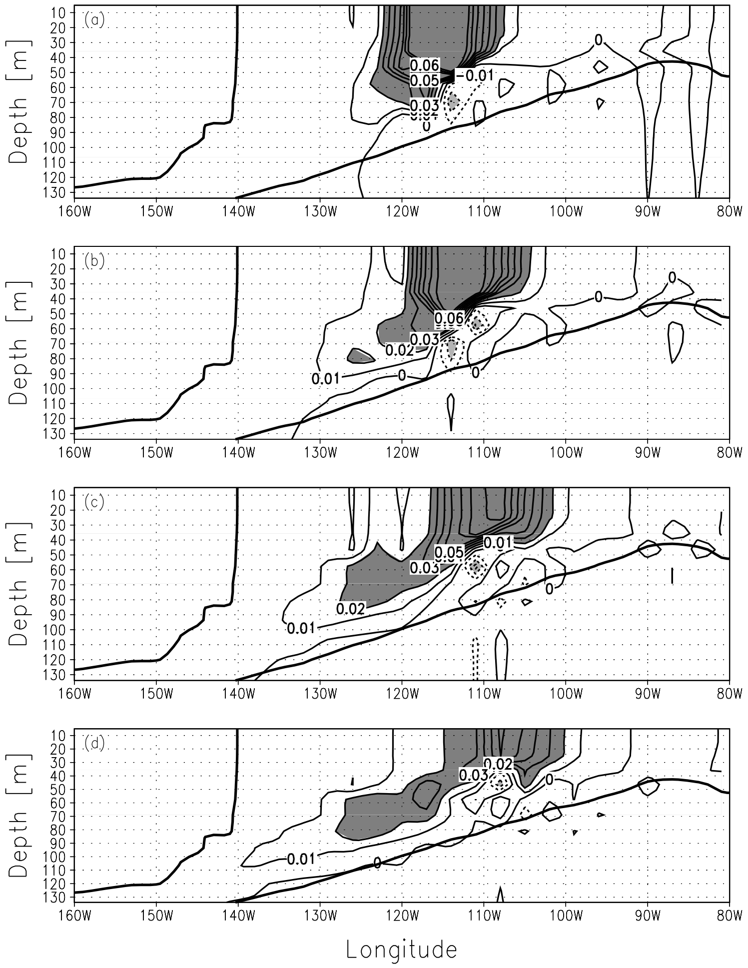

FIG. 9. Sensitivity of a cost function located at the surface and evaluated in December to temperature perturbations (a) 15 days, (b) 30 days, (c) 45 days and (d) 60 days from the time of the cost function evaluation. Values larger (smaller) than 0.02 (−0.02) are shaded with dark (light) gray.

of the *surface-December* experiment were able to propagate westward along the thermocline where mixing is much weaker.

Our assumption that the surface interacts with the thermocline mostly through the thermocline outcropping area implies that perturbations arriving in the east along the thermocline, will get to the surface by vertical mixing. When the thermocline outcrops over a wide area, the vertical stratification in the outcrop area is weak, and therefore mixing is strong. This means that a thermocline deepening signal arriving via a baroclinic Kelvin Wave will be effective in reducing the mixing between the surface and the cold subsurface water, changing the heat balance of the surface water and causing a surface warming. On the other hand, when the thermocline does not outcrop, the vertical stratification is strong and the vertical mixing is already weak. A thermocline deepening signal arriving along the thermocline as a Kelvin wave will not reduce the already weak vertical mixing much more, and therefore will not have a large effect on the SST. We can use the adjoint method to test this assumption regarding the role of vertical mixing by running again the *surface-December* experiment, only this time with the terms in the adjoint model corresponding to vertical mixing shut-off (experiment *surface-December-no-mix*, Table 1). Fig. 12 shows the difference between the *surface-December* case and the case with no vertical mixing affecting the adjoint solution (experiment *surface-December-no-mix*). It is evident that in the no vertical mixing case, the surface sensitivities do not penetrate the thermocline, thus supporting our assumption that vertical mixing provides the link between the Kelvin

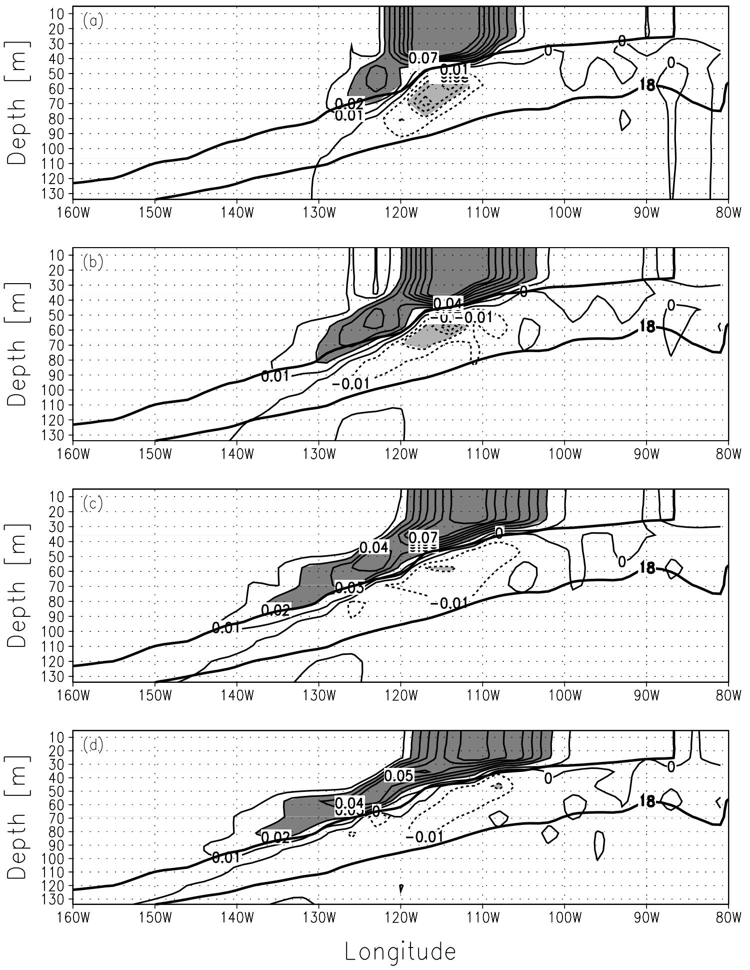

FIG. 10. Sensitivity of a cost function located at the surface and evaluated in June to temperature perturbations (a) 15 days, (b) 30 days, (c) 45 days and (d) 60 days from the time of the cost function evaluation. Values larger (smaller) than 0.02 (−0.02) are shaded with dark (light) gray.

waves propagating along the thermocline and the sea surface temperature.

These experiments support our hypothesis on the seasonal dependence of anomaly growth in the model. The outcropping of the thermocline in the East Pacific is what enables the Kelvin waves arriving in the east to influence the SST. This outcropping occurs from summer to early winter, which is the time when ENSO grows the most. The formation of the strong stratification at the East Pacific in the later months of the winter prohibits the anomaly growth. This new insight is only possible because our ocean model explicitly resolves the thermocline and mixed layer. This mechanism is not represented in intermediate models that do not explicitly resolve the mixed layer dynamics or that do not include the seasonal variations in the thermocline depth (e.g. the CZ model).

Our focus here was the effect of the seasonal outcropping on the coupled ocean-atmosphere system dynamics. Accordingly, the background state used here for the adjoint model run and sensitivity analysis is the solution of the forward coupled model started from the ocean-only climatology. This solution is not far from the seasonal climatology of the ocean-only model. In principle, the adjoint sensitivity might change as function of the ENSO phase, as explored using the adjoint method by Van-Oldenborgh et al. (1999) or from a different perspective by Samelson and Tziperman (2001). This issue deserves further examination, yet is beyond the scope of the present work.

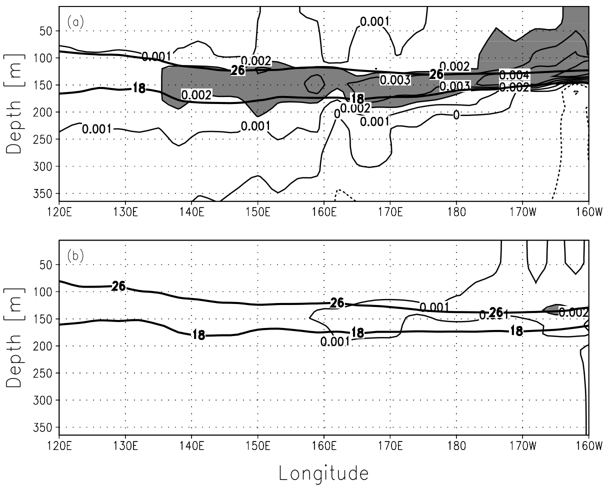

FIG. 11. Sensitivity of a cost function located at the surface to temperature perturbations, after 5 months. Upper panel (a) is for the December-case and lower panel (b) is for the June-case. Values larger (smaller) than 0.002 (−0.002) are shaded with dark (light) gray.

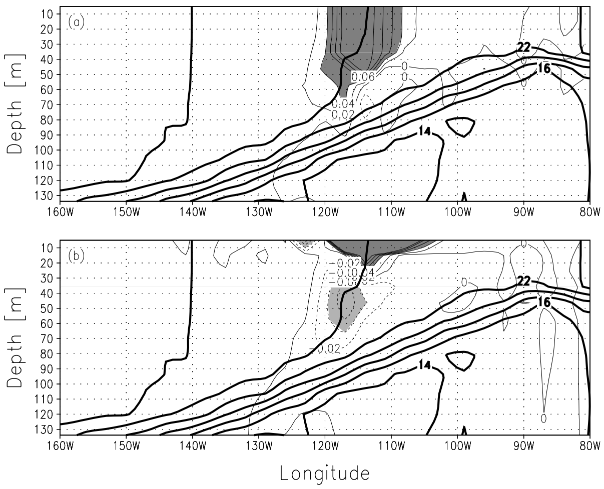

FIG. 12. The contribution of vertical mixing to the connection between the surface and the thermocline. Upper panel (a) shows the temperature sensitivities after one month in the standard case. Lower panel (b) shows the sensitivities when the vertical mixing is shut-off. Values larger (smaller) than 0.04 (−0.04) are shaded with dark (light) gray.

8. Discussion and conclusion

The problem of identifying a mechanism for the seasonal changes in the tropical Pacific ocean-atmosphere instability strength was addressed in many previous studies. However, most if not all of these previous works used simplified models, ranging from low-order models to intermediate models such as the Cane-Zebiak model (Zebiak and Cane 1987). Here we have used a hybrid coupled model, composed of an ocean GCM coupled to a statistical atmosphere, which allows us to examine physical processes not represented in intermediate models.

The positive feedback allowing the growth of anomalous conditions in the tropical Pacific can be described as follows: a positive SST perturbation in the East Pacific excites westerly wind anomalies in the Central Pacific. These wind anomalies then excite downwelling Kelvin waves that propagate eastward. Upon reaching the East Pacific, the subsurface perturbations in the thermocline affect the sea surface temperature. The seasonality in the ocean-atmosphere coupling strength must, therefore, be due to a seasonal modulation in the effectiveness of one of the above processes.

Most of the simple and intermediate ENSO models represent the subsurface thermal structure of the equatorial Pacific by an upper warm layer and a deeper cold layer. The interaction between the surface and subsurface is commonly assumed to be a function of the movements of the thermocline separating the two layers. More specifically, the term that affects the SST in the CZ-like models is the advection by the upwelling that relates changes in SST to the thermocline depth. Vertical mixing is not explicitly included but is clearly implied in this parameterization via the way the upwelling affects the SST if the thermocline nears the surface. While having the advantage of simplicity, these models do not include the seasonal movements of the thermocline and its outcropping, and they also lack the explicit effect of this vertical thermocline movement on the vertical mixing between the surface and the subsurface waters.

In this work we showed that an important factor determining the strength of the coupled ocean-atmosphere instability and its seasonal variations is the strength of the East Pacific SST response to changes in the thermal structure beneath it. We found that the outcropping of the thermocline in the east equatorial Pacific controls the SST response to subsurface temperature anomalies. When a warm thermocline deepening signal reaches the East Pacific as downwelling Kelvin waves, its influence on the surface (SST) depends on the exposure of the thermocline at the surface; a thermocline deepening signal that arrives in late winter to spring time, when there is a strong stratification and therefore weak vertical mixing between the thermocline and the surface, will not affect the vertical mixing and will therefore not affect the SST. On the other hand, a warm thermocline deepening signal that arrives in fall and early winter, when the thermocline is then exposed to the surface, the stratification is weak and vertical mixing between the thermocline and the surface is strong, will be able to weaken the mixing between the cold subsurface water and the surface water, and induce an SST warming. The seasonal ocean-atmosphere coupling strength is therefore influenced by the seasonal changes in the East pacific thermocline outcropping.

The modulation of the subsurface to surface connection by the seasonal changes in the thermocline outcropping is relevant also to the effect of vertical thermocline movements through the ENSO cycle. Our discussion of the role of thermocline outcropping and vertical mixing may therefore also be relevant to the analysis of (Van-Oldenborgh et al. 1999) which found changes in ENSO's sensitivity during different phases of the ENSO cycle.

Neelin et al. (2000) showed that changing the mixed layer parameterization in their model, shifted the peak of the model ENSO events by a few months, although they could not explain this in terms of a specific physical mechanism. A wave dynamics mechanism for ENSO's phase locking was presented by Tziperman et al. (1998) and Galanti and Tziperman (2000). This mechanism is based on the seasonal variations of the ocean-atmosphere instability strength that affects the amplification of ocean waves. The present work shows that the coupled instability strength and its seasonal variations are strongly affected by the mixed layer processes through the thermocline outcropping dynamics. We therefore suggest here that the mixed layer parameterization affects the coupled instability strength and its seasonal variations (via the thermocline outcropping mechanism). Therefore the mixed layer parameterization affects the seasonal amplification of ocean waves, and may influence the phase locking of ENSO as observed by Neelin et al. (2000), based on the dynamical explanations of Tziperman et al. (1998) and Galanti and Tziperman (2000).

The study of the thermocline outcropping and its effect on the instability strength was made possible thanks to the use of a full 3D ocean model. It would be interesting to further examine the issue using higher-resolution models with improved representation of mixed layer processes.

Acknowledgment. This work was partially funded by the Israeli Science Foundation, and by NOAA through the office of global programs. We are grateful to Ron Pacanowski for making the version of MOM used here available to us, and to Andrew Moore and Geert Jan van Oldenborgh for their most constructive and useful reviews.

REFERENCES

Battisti, D. S., 1988: The dynamics and thermodynamics of a warming event in a coupled tropical atmosphere/ocean model. *J. Atmos. Sci.*, **45**, 2889–2919.

Battisti, D. S., and A. C. Hirst, 1989: Interannual variability in the tropical atmosphere-ocean system: Influence of the basic state and ocean geometry. *J. Atmos. Sci.*, **45**, 1687–1712.

Cane, M. A., M. Münnich, and S. E. Zebiak, 1990: A Study of Self-Excited Oscillations of the Tropical Ocean-Atmosphere System. Part I: Linear Analysis. *J. Atmos. Sci.*, **47**(13), 1562–1577.

Chang, P., B. Wang, T. Li, and L. Ji, 1994: Interactions between the seasonal cycle and the southern oscillation — frequency entrainment and chaos in a coupled ocean-atmosphere model. *Geophys. Res. Lett.*, **21**, 2817–2820.

Chen, D., S. E. Zebiak, A. J. Busalacchi, and M. A. Cane, 1995: An improved procedure for El Niño forecasting: Implications for predictability. *Science*, **269**, 1699–1702.

Errico, R. M., and T. Vukicevic, 1992: Sensitivity analysis using an adjoint of the psu-ncar mesoscale model. *Mon. Weath. Rev.*, **120**, 1644–1660.

Esbensen, S. K., and V. Kushnir, 1981: The heat budget of the global ocean: An atlas based on estimates from surface marine observations. Clim. Res. Inst., Tech. Rep. 29.

Farrell, B., 1988: Optimal excitation of neutral Rossby waves. *J. Atmos. Sci.*, **45**, 163–172.

Galanti, E., and E. Tziperman, 2000: ENSO's phase locking to the seasonal cycle in the fast sst, fast wave, and mixed mode regimes. *J. Atmos. Sci.*, **57**, 2936–2950.

Gibson, J., S. Kallberg, S. Uppala, A. Nomura, A. Hernandez, and E. Serrano, 1997: ECMWF reanalysis project report series no.1 technical report 1. ECMWF, Shinfield Park, Reading, U.K., Tech. rep.

Giering, R., 1997: Tangent linear and adjoint model compiler, users manual. http://puddle.mit.edu/∼ralf/tamc, Tech. rep.

Giering, R., and T. Kaminski, 1998: Recipes for adjoint code construction. *Acm Transactions On Mathematical Software*, **24**(4), 437–474.

Gu, D., and S. Philander, 1995: Secular changes of annual and interannual variability in the tropics during the past century. *J. Climate*, **8**(4), 864–876.

Gu, D., and S. G. H. Philander, 1997: Interdecadal climate fluctuations that depend on exchanges between the tropics and extratropics. *Science*, **275**(7), 805–807.

Hall, M. C. G., 1986: Application of adjoint sensitivity theory to an atmospheric general circulation model. *J. Atmos. Sci.*, **43**, 2644–2651.

Harrison, M. J., A. Rosati, B. J. Soden, E. Galanti, and E. Tziperman, 2002: An evaluation of air-sea flux products for enso simulation and prediction. *Monthly Weather Review*, **130**(3), 723–732.

Hirst, A. C., 1986: Unstable and damped equatorial modes in simple coupled ocean-atmosphere models. *J. Atmos. Sci.*, **43**, 606–630.

Jin, F.-F., and D. Neelin, 1993: Models of interannual tropical ocean-atmosphere interaction - a unified view. part i: numerical results. *J. Atmos. Sci.*, **50**, 3477–3503.

Jin, F.-F., D. Neelin, and M. Ghil, 1994: ENSO on the devil's staircase. *Science*, **264**, 70–72.

Kleeman, R., and A. M. Moore, 1997: A theory for the limitation of ENSO predictability due to stochastic atmospheric transients. *JAS*, **54**, 753–767.

Levitus, S. E., 1982: *Climatological atlas of the world ocean*. NOAA Professional Paper 13, US Government Printing Office, Washington DC.

Marotzke, J., R. Giering, K. Q. Zhang, D. Stammer, C. Hill, and T. Lee, 1999: Construction of the adjoint mit ocean general circulation model and application to Atlantic heat transport sensitivity. *J. Geophys. Res.*, **104**(C12), 29,529–29,547.

Moore, A. M., and R. Kleeman, 1996: The dynamics of error growth and predictability in a coupled model of ENSO. *Q. J. R. Meteor. Soc.*, **122**, 1405–1446.

Moore, A. M., and R. Kleeman, 1997: The singular vectors of a coupled ocean-atmosphere model of ENSO, II, sensitivity studies and dynamical interpretation. *Q. J. R. Meteor. Soc.*, **123**, 983–1006.

Neelin, J., F. Jin, and H. Syu, 2000: Variations in ENSO phase locking. *J. Climate*, **13**(14), 2570–2590.

Pacanowski, R. C., and S. M. Griffies, 1999: *MOM 3.0 Manual*, NOAA/Geophysical Fluid Dynamics Laboratory, Princeton, NJ, USA 08542.

Pacanowski, R. C., and S. G. H. Philander, 1981: Parameterization of vertical mixing in numerical models of tropical oceans. *J. Phys. Oceanogr.*, **11**, 1443–1451.

Penland, C., and P. D. Sardeshmukh, 1995: The optimal-growth of tropical sea-surface temperature anomalies. *J. Climate*, **8**(8), 1999–2024.

Philander, S. G., 1983: El Niño southern oscillation phenomena. *Nature*, **302**, 295–301.

Philander, S. G. H., 1990: *El Niño, La Niña, and the Southern Oscillation.*. Academic Press.

Reynolds, R. W., and T. M. Smith, 1994: Improved global sea surface temperature analyses using optimum interpolation. *J. Climate*, **7**, 929–948.

Samelson, R., and E. Tziperman, 2001: Predictability of the chaotic ENSO: the growth phase predictability barrier. *J. Atmos. Sci.*, **58**, 3613–3625.

Sirkes, Z., and E. Tziperman, 2001: Identifying a damped oscillatory thermohaline mode in a general circulation model using an adjoint model. *J. Phys. Oceanogr.*, **in press**.

Stricherz, J., D. Legler, and J. J. O'Brien, 1997: Toga pseudo-stress atlas 1985-1994, volume III: Indian Ocean, 155pp. Florida State University, Tallahassee, FL, Tech. Rep. 155 pp.

Stricherz, J. J. O., J., and D. M. Legler, 1992: Atlas of florida state university tropical Pacific winds for toga 1966-1985. Florida State University, Tallahassee, FL, Tech. rep.

Syu, H., and J. Neelin, 2000: ENSO in a hybrid coupled model. Part I: sensitivity to physical parameterizations. *Clim. Dyn.*, **16**, 19–34.

Syu, H.-H., J. Neelin, and D. Gutzler, 1995: Seasonal and interannual variability in a hybrid coupled gcm. *J. Climate*, **8**, 2121–2143.

Thacker, W. C., 1987: Three lectures on fitting numerical models to observations, external report gkss 87/e/65. GKSS-Forschungszentrum Geesthacht GmbH, Geesthacht, Federal Republic of Germany, Tech. rep.

Torrence, C., and P. J. Webster, 1998: The annual cycle of persistence in the El Nino southern oscillation. *Q. J. R. Meteorol. Soc.*, **124**(550), 1985–2004.

Tziperman, E., and W. C. Thacker, 1989: An optimal-control adjoint-equations approach to studying the oceanic general-circulation. *J. Phys. Oceanogr.*, **19**(10), 1471–1485.

Tziperman, E., L. Stone, M. A. Cane, and H. Jarosh, 1994: El-nino chaos: Overlapping of resonances between the seasonal cycle and the pacific ocean-atmosphere oscillator. *Science*, **264**(5155), 72–74.

Tziperman, E., M. A. Cane, and S. E. Zebiak, 1995: Irregularity and locking to the seasonal cycle in an ENSO prediction model as explained by the quasi-periodicity route to chaos. *J. Atmos. Sci.*, **52**(3), 293–306.

Tziperman, E., S. E. Zebiak, and M. A. Cane, 1997: Mechanisms of seasonal: ENSO interaction. *J. Atmos. Sci.*, **54**(1), 61–71.

Tziperman, E., M. A. Cane, S. E. Zebiak, Y. Xue, and B. Blumenthal, 1998: Locking of El Nino's peak time to the end of the calendar year in the delayed oscillator picture of ENSO. *J. Climate*, **11**(9), 2191–2199.

Van-Oldenborgh, G., 2000: What caused the onset of the 1997/98 El Nino? *Mon. Weath. Rev.*, **128**, 2601–2607.

Van-Oldenborgh, G. J., G. Burgers, S. Venzke, C. Eckert, and R. Giering, 1999: Tracking down the ENSO delayed oscillator with an adjoint ogcm. *Mon. Weath. Rev.*, **127**(7), 1477–1495.

Webster, P. J., and S. Yang, 1992: Monsoon and enso: Selectively interactive systems. *Q. J. R. Meteorol. Soc.*, **118**(507), 877–926.

Weiss, J. P., and J. B. Weiss, 1999: Quantifying persistence in ENSO. *J. Atmos. Sci.*, **56**(16), 2737–2760.

Xue, Y., M. A. Cane, S. E. Zebiak, and M. B. Blumenthal, 1994: On the prediction of ENSO: a study with a low order Markov model. *Tellus*, **46A**, 512–528.

Zebiak, S. E., and M. A. Cane, 1987: A model El Niño-Southern Oscillation. *Mon. Weath. Rev.*, **115**, 2262–2278.

Chapter 4:
A Mid-Latitude – ENSO teleconnection mechanism via baroclinically unstable Long Rossby Waves

ELI GALANTI AND ELI TZIPERMAN

Environmental Sciences, Weizmann Institute, Rehovot 76100, Israel

ABSTRACT

The possibility of generating decadal ENSO variability via an ocean teleconnection to the mid-latitude Pacific is studied. This is done by analyzing the sensitivity of the equatorial stratification to mid-latitude processes using an ocean GCM, the adjoint method, and a QG normal mode stability analysis. It is found that, on time scales of 2 to 15 years, the equatorial Pacific is most sensitive to mid-latitude planetary Rossby waves traveling from the mid-latitudes toward the western boundary and then to the equator. Those waves that propagate through baroclinically unstable parts of the sub-tropical gyre are amplified by the baroclinic instability, and therefore dominate the mid-latitude signal arriving at the equator. This implies that decadal variability in the mid-latitude Pacific would be efficiently transmitted to the equatorial Pacific from specific areas of the mid-latitude pacific, that are baroclinically unstable, such as the near-equatorial edges of the sub-tropical gyres (15°N and 12°S). The Rossby waves that propagate via the baroclinically unstable areas are of the advective mode type which follow the gyre circulation to some degree, and arrive from as far as 25°N and 30°S in the east Pacific. It is shown that the baroclinic instability involves critical layers due to the vertical shear of the sub-tropical gyre circulation, at depths of 150-200 meters.

1. Introduction

ENSO's decadal variability (e.g. An and Wang 2000; Trenberth and Hurrell 1994) has been a subject of quite a few studies during the past decade or so. Because typical time scales at the equator are relatively short, a strong candidate for this equatorial decadal variability is the slower mid-latitude ocean which somehow affects the equatorial ocean (e.g. Gu and Philander 1997; Jin 2001; Kleeman et al. 1999). Gu and Philander (1997) suggested that the decadal variability in the Equatorial Pacific is a result of surface mid-latitude water sinking along isopycnals toward the central Pacific equatorial thermocline base, where it upwells to the surface to affect the SST. The warmer SST, in turn, aside from changing the characteristics of ENSO (strength, period, etc.) also affects the mid-latitude westerlies through the tropics-extratropics temperature gradient. The stronger westerlies in the mid-latitudes enhance evaporative cooling, and create colder water that sinks and is advected toward the equator by the ocean general circulation, to later cool the SST there. The result is an interdecadal oscillation with an amplitude of about $1°C$ SST anomaly.

This scenario was modified in various ways by other studies. Some focused on pure oceanic pathways between the mid-latitude and the equatorial region via long isopycnal advection (Harper 2000; Zhang et al. 2001) or via planetary waves that propagate from mid-latitudes to the tropics (Capotondi and Alexander 2001; Jin 2001; Lysne et al. 1997). Repeat hydrography observations show eddy motions that may perhaps be interpreted as planetary waves (e.g. Roemmich and Gilson 2001). Some other studies seemed to find that oceanic teleconnections are not efficient (Hazeleger et al. 2001), and others that the oceanic teleconnection is mostly active in the southern hemisphere (Schneider et al. 1999). An alternative atmospheric bridge via which atmospheric influence propagates to the tropics has also been suggested (Barnett et al. 1999). The influence of the tropical SST on the mid-latitude atmosphere is proposed by Kleeman et al. (1999) to be via effects on the subtropical gyre circulation rather than via evaporative cooling.

The question of what is the relative importance of the two oceanic teleconnection mechanisms (subduction vs. waves) in transferring decadal signals from the mid-latitudes to the equator, is still unanswered. Another unresolved issue in these works is what selects the particular mid-latitude areas from which Rossby waves arrive to influence the equatorial Pacific

In this work we attempt a new approach to the study of possible oceanic teleconnections from the mid-latitudes to the equatorial Pacific. We use the adjoint method of sensitivity studies (Galanti et al. 2002a; Hall and Cacuci 1983; Marotzke et al. 1999) with an ocean GCM to ask what are the mid-latitude locations and physical processes that influence the equatorial region within a decadal time scale. We find that long Rossby waves that propagate from the mid-latitude as far as 25°N and 30°S are the dominant mechanism that transmits information from the mid-latitudes to the equator in our model. Furthermore, we find that the waves which are especially effective in transmitting information from the mid-latitudes to the equator travel mostly along specific latitude bands (15N and 12S). By analyzing the quasi-geostrophic normal modes for the model background state, we show that the model climatology is baroclinically unstable at the latitudes where the sensitivities are seen. The Rossby waves that are able to affect substantially the equatorial thermal structure, seem to be of the ”advective mode” type (Liu 1999b) which tend to follow the gyre circulation fairly closely yet are distinct from an advection by the gyre circulation.

Fig. 1 therefore summarizes our main finding here. Rossby waves travel from all latitudes of the Pacific ocean toward the western boundary, and then travel as coastal Kelvin waves to affect the equator. However, only the waves that travel along baroclinically unstable parts of the mid-latitude gyre (mostly the southern edge of the gyre in the North Pacific and northern edge in the south Pacific) are amplified by baroclinic instability. Waves at other latitudes are damped by various dissipative mechanisms and do not make it to the equator. The Rossby waves that travel along the baroclinically unstable areas reach the equator with a larger amplitude, dominate the mid-latitude signal that affects the basic stratification there.

The paper is organized as follows. In section 2 we describe the ocean model and the adjoint method used in the study. The adjoint sensitivity results are presented in section 3 together with an analysis of the sensitivity dynamics. Section 4 analyzes the normal model QG stability of the model background climatology and the results are compared to the sensitivity structure from the adjoint model runs. We conclude in section 5.

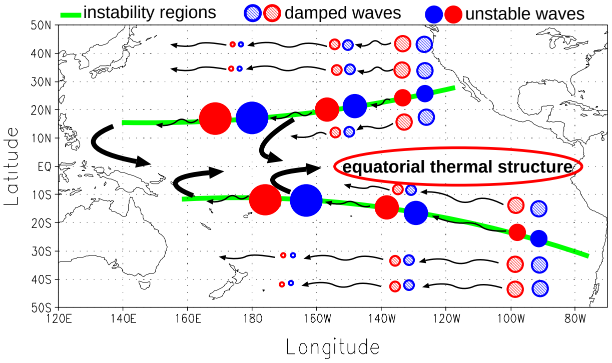

FIG. 1. A schematic figure of the mechanism proposed in this paper for a wave teleconnection from the mid-latitude Pacific to the equator. Mid-latitude planetary Rossby waves travel westward at all latitudes and are damped. The waves that are amplified in baroclinically unstable regions of the sub-tropical gyre arrive to the equator with a larger amplitude and therefore dominate the mid-latitude signal there.

2. The model

The ocean model we use and its adjoint were described in details by Galanti et al. (2002a). It was used for sensitivity studies of the equatorial Pacific ocean-atmosphere instability mechanism (Galanti et al. 2002a), as well as for investigating ENSO predictability based on the adjoint method of data assimilation (Galanti et al. 2002b). Here we give a brief description of the model components.

The ocean model is based on the Geophysical Fluid Dynamics Laboratory (GFDL) modular ocean model (MOM) (Pacanowski and Griffies 1999). The model domain is the Indo-Pacific region, 30°E-70°W, and 50°S-50°N. The model resolution is 3° in longitude, 3° going to 1° at the equator in latitude, and 30 depth levels where the top 15 layers are within the top 200 meters of the ocean. The resolution is such that the equatorial dynamics (Kelvin and Rossby waves) are resolved, while the computational cost is small enough to enable many long model runs.

The model uses a modified Richardson-number dependent vertical mixing scheme (Pacanowski and Philander 1981; Syu and Neelin 2000). In addition, a simplified mixed-layer scheme is applied as in Syu and Neelin (2000). Constant horizontal viscosity and diffusivity are used. The temperature and salinity are restored to the monthly Levitus (1982) climatology within sponge layers at the North and South horizontal boundaries.

The model is spun-up forced by the climatological FSU wind stress (Stricherz et al. 1997; Stricherz and

Legler 1992) and climatological heat fluxes (Esbensen and Kushnir 1981). The model is also restored to the climatological monthly NCEP SST (Reynolds and Smith 1994) and to the climatological monthly Levitus SSS (Levitus 1982) with a restoring time of 10 days. After reaching its mean seasonal climate state (50 years of spin-up), the monthly-mean model air-sea flux is saved to be used as a flux adjustment term. A weak restoring to the surface model climatology of 100 days is applied during the model run. The monthly temperature climatology of the flux corrected model is similar to the Levitus climatology.

An adjoint model for the ocean model was derived with the help of the Tangent linear and Adjoint Model Compiler (Giering 1997; Giering and Kaminski 1998; Marotzke et al. 1999). As the time scale of interest in this work is much longer than the time scale studied in Galanti et al. (2002a), some modifications had to be made to the model and to its adjoint. The model vertical resolution is very coarse in the deep ocean, reaching grid size of about 600 meters in the deepest level. The model thus exhibits a weak numerical instability that arises from the inaccuracy of the finite differencing scheme at the lower levels. In the forward run, this weak numerical instability is damped by the model nonlinearities and is observed as a small amplitude noise near the bottom. During the adjoint run, these instabilities grow since the adjoint model is linear, so that at time scales of more than a few years the instabilities develop and influence the adjoint solution. In order to eliminate this problem we restored the adjoint solution of the temperature and salinity at the deepest model level to zero at each time step. We have run a few tests and found that this restoring does not introduce artifacts into our upper ocean model results which are of interest in this study.

The physical context of the adjoint sensitivity experiments is determined by the formulation of the cost function, and by the choice of the control variables. The cost function is the scalar whose sensitivity is studied with respect to changes in the control variables; it can be any measure of the model state. The cost function we use is the same as the one used in Galanti et al. (2002a). It is a summation over the sub-surface model temperature in the equatorial East Pacific, where the temperature signal of the mature phase of ENSO is maximal,

$$\begin{aligned} J &= \int d^3\mathbf{x}\,dt\,T(\mathbf{x},t) \times \exp\left(-\frac{(x-100°W)^2}{10°^2} \right. \\ &- \left. \frac{(y-0°N)^2}{2°^2} - \frac{(z-60\,m)^2}{(40\,m)^2} - \frac{t^2}{(10\,day)^2} \right) \quad (1) \end{aligned}$$

where $\mathbf{x} = (x,y,z)$. This cost function also reflects the status of the sub-surface thermocline structure, whose changes may lead to decadal ENSO variability. The control variables we will look at are the temperature and salinity fields, as they determine the density field. Note that all adjoint sensitivities appearing in this work are normalized by the volume of the box they represent, in such a way that the surface variables at the equator (smallest box volume) are normalized by a factor of one (see Galanti et al. 2002a; Marotzke et al. 1999, for an extensive discussion). The normalization of the adjoint solution is done only when displaying and analyzing the results, and not during the adjoint model integration.

3. Results

We now present the results from the adjoint model runs, along with results from two complementary experiments of the forward model that are helpful in the interpretation of the sensitivity results.

a. Decadal sensitivities

We ran the ocean model for 20 years, during which it remained around its climatology, and its adjoint over the same period backward in time. The adjoint model calculates the sensitivity of the cost function to perturbations in all model variables at all times between the time of the cost function evaluation and the time of the initial conditions. Fig. 2 shows the sensitivity to temperature perturbations at a depth of 200 meters, 4, 8 and 12 years prior to the time of the cost function evaluation. A positive sensitivity somewhere in the middle panel means that a positive temperature perturbation applied at that location will lead to an increase of the cost function (integrated temperature over the sub-surface east equatorial Pacific) evaluated 8 years later. A negative sensitivity means that a positive perturbation will lead to a decrease of the cost function. The amplitude of the sensitivity indicates, for example, that a perturbation applied four years before the time of the cost function evaluation (Fig. 2a) at 160°E and 15°N is twice as effective in increasing the value of the cost function than a temperature perturbation at 160°E and 13°N at the same time. The main feature seen in the sensitivities is a wave-like pattern (which we will denote 'adjoint waves' from now on) that is formed around latitudes 15°N and 12°S, and travel eastward approximately along lines of constant temperature of the forward model climatology (thick black line in the figure). Upon reaching the east Pacific, the adjoint wave trajectory is bent toward 25°N and 30°S.

The eastward propagation of the adjoint sensitivity waves is further illustrated in Fig. 3 where the sensitivity

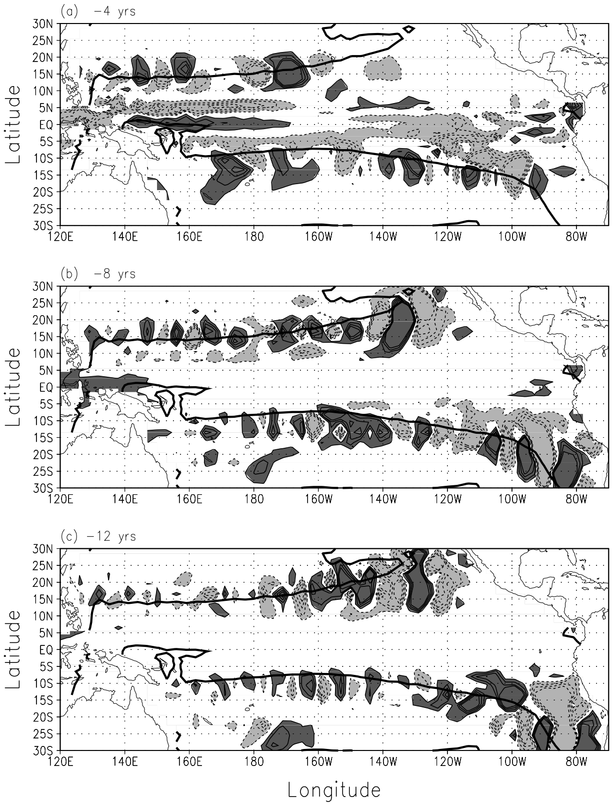

FIG. 2. Sensitivity to temperature perturbations at a depth of 200m, at time intervals of: (a) 4 years, (b) 8 years, and (c) 12 years, before time of cost function evaluation. Values larger (smaller) than 0.005 (-0.005) are shaded with dark (light) gray. The thick black line denotes the 16°C isotherm of the forward model climatology.

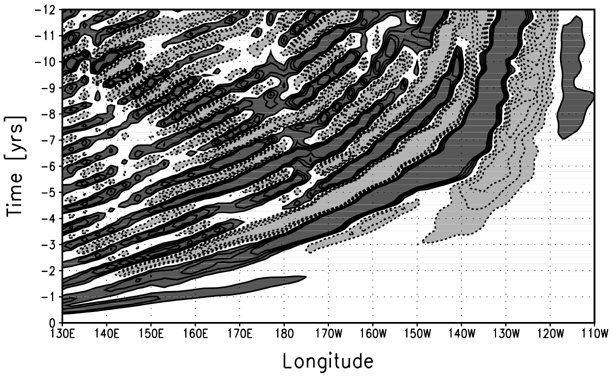

FIG. 3. Sensitivity to temperature perturbations at 15°N and depth of 200m as function of longitude and time (in years before time of cost function evaluation). Values larger (smaller) than 0.005 (-0.005) are shaded with dark (light) gray.

to temperature perturbation at 15°N and a depth of 200 meters is plotted as function of longitude and time. The velocity of the 'adjoint waves' west of 160W is about $4cm/sec$ and east of 160°W is about $2cm/sec$.

The sensitivities shown in Fig. 2 are the main result of this paper. As explained above, the adjoint model calculates the sensitivity of the cost function to perturbations to the model variables at different times and locations. Physically, the sensitivities in Fig. 2 indicates that temperature perturbations applied off the equator would influence the subsurface temperature in the east equatorial Pacific a few years later. This, of course, indicates some teleconnection mechanism between the equatorial and off equatorial areas of the Pacific ocean, which is what we are after in this study.

Another thing to remember is that the adjoint model is integrated backward in time. When interpreting a sensitivity pattern that propagates in time, the direction of propagation should therefore be reversed; the 'adjoint waves' we see propagating *eastward* are therefore an indication of a sensitivity to physical Rossby waves that propagate *westward*.

Fig. 4 shows a cross section along 15°N, at times of 4, 8, and 12 years before the time of cost function evaluation. The temperature sensitivities are located around a depth of 200 meters, and are also vertically tilted to the east. The 16°C isotherm of the forward model climatology is also plotted for reference. The main features seen in Fig. 4 are eastward tilted wavelike sensitivities; these features indicate that applying perturbations in the forward model that have the same spatial eastward tilt will be most efficient in increasing the value of the cost function (that is, the subsurface equatorial temperature) a few years later. We will show in the following sections that these are sensitivities to mid-latitude long Rossby waves, and that baroclinic instability, hinted by this tilt, plays an important role in their development and amplification. A meridional cross section of the temperature anomalies shows that the sensitivities tend to be located in regions where the climatological meridional temperature gradient is largest (not shown), and we will discuss the relevance of this to baroclinic instability in the followings. The sensitivities in the southern hemisphere are somewhat less pronounced and are stronger at the east Pacific, around 25°S.

We can conclude at this stage that at time scales from 2 to 15 years, the largest sensitivity of the East Pacific equatorial thermocline is to perturbations that travel westward (in the forward model) in the vicinity of 15°S and 12°N. These sensitivities seem to have the shape and propagation properties of mid-latitude long Rossby waves. Note that the sensitivity signal seems to propa-

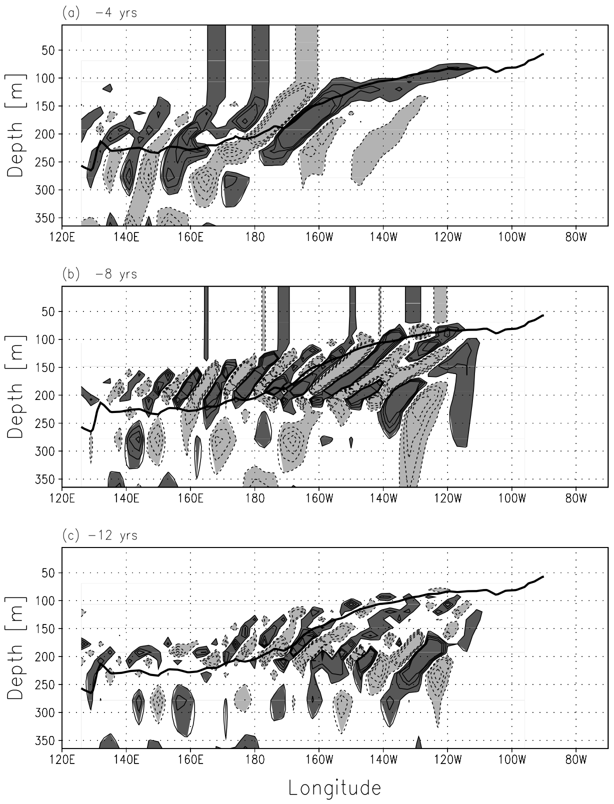

FIG. 4. Sensitivity to temperature perturbations at 15°N as function of longitude and depth, at time intervals of: (a) 4 years, (b) 8 years, and (c) 12 years, before the time of cost function evaluation. Values larger (smaller) than 0.005 (−0.005) are shaded with dark (light) gray. The thick black line denotes the 16°C isotherm of the forward model climatology.

gate from the mid-latitude not by advection (e.g. Gu and Philander 1997; Harper 2000), but rather via a dynamical process that involves planetary wave propagation.

b. *Are these actually waves?*

The first question we need to address is whether the above propagation signal of the sensitivities is really due to waves as it appears to be. Since the cost function is a summation over the east equatorial temperature, this question can be resolved by separating the sensitivities into a *dynamical* sensitivity and a *kinematic* sensitivity (Marotzke et al. 1999). A change in temperature can be due to a "dynamical" process such as internal wave propagation which merely moves the isopycnal layers vertically. We clearly want to verify that our sensitivities correspond to such a dynamical sensitivity. Alternatively, the temperature can vary due to a "kinematic" process such as an advective or diffusive along-isopycnal intrusion process that modifies the temperature and salinity, leaving the density unchanged (Munk 1981). In both cases (of dynamical and kinematic sensitivities), the temperature and salinity sensitivities are not independent and can be shown to be related via the thermal and salinity expansion coefficients (Marotzke et al. 1999),

$$\alpha \equiv -\frac{1}{\rho}\left(\frac{\partial\rho}{\partial T}\right)_S; \qquad \beta \equiv \frac{1}{\rho}\left(\frac{\partial\rho}{\partial S}\right)_T. \tag{2}$$

Begin by writing the cost function J as a function of the density ($\rho(T,S)$) and of the temperature (T) fields,

$$J = J(\rho(t,S),T). \tag{3}$$

In writing the cost this way, we separate the influence on the cost function into the part that comes from vertically moving the isopycnal surfaces ($\rho(T,S)$), and the part that comes from intrusion processes that modify the temperature, leaving the density unchanged. The sensitivity of the cost function J to the temperature T, at a constant salinity, is therefore

$$\begin{aligned}\left(\frac{\partial J}{\partial T}\right)_S &= \left(\frac{\partial J}{\partial\rho}\right)_T\left(\frac{\partial\rho}{\partial T}\right)_S + \left(\frac{\partial J}{\partial T}\right)_\rho \\ &= -\alpha\rho\left(\frac{\partial J}{\partial\rho}\right)_T + \left(\frac{\partial J}{\partial T}\right)_\rho \qquad (4)\end{aligned}$$

where the first and second terms on the rhs of (4) are the dynamical and kinematic sensitivities, respectively. The sensitivity of the cost function J to the salinity S is

$$\left(\frac{\partial J}{\partial S}\right)_T = \left(\frac{\partial J}{\partial\rho}\right)_T\left(\frac{\partial\rho}{\partial S}\right)_T = \beta\rho\left(\frac{\partial J}{\partial\rho}\right)_T. \tag{5}$$

The adjoint model actually calculates only $(\partial J/\partial T)_S$ and $(\partial J/\partial S)_T$. These may be used to calculate the two sensitivities by using (2), (4) and (5), so that

$$\begin{aligned}-\alpha\rho\left(\frac{\partial J}{\partial\rho}\right)_T &= -\frac{\alpha}{\beta}\left(\frac{\partial J}{\partial S}\right)_T \text{(dyn.)} \qquad (6)\\ \left(\frac{\partial J}{\partial T}\right)_\rho &= \left(\frac{\partial J}{\partial T}\right)_S + \frac{\alpha}{\beta}\left(\frac{\partial J}{\partial S}\right)_T \text{(kin.)} \qquad (7)\end{aligned}$$

Fig. 5 shows the dynamic (6) and kinematic (7) sensitivities to temperature perturbations. It is clear that most of the sensitivity calculated by the adjoint model is dynamical. Kinematic sensitivity can be seen only around (15°S,140°W) and is much smaller than the dynamic sensitivity. We can therefore conclude that the adjoint sensitivities we observe in the model at time scales of 2-15 years are indeed dynamical sensitivities due to internal planetary wave motions, rather than the long-isopycnal advection processes.

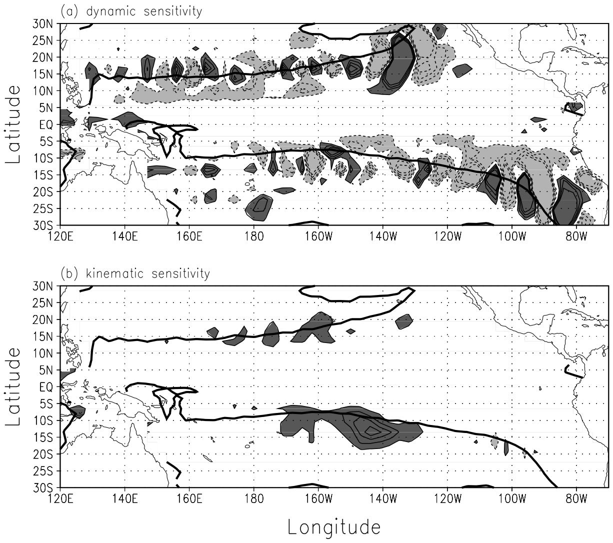

FIG. 5. Demonstrating that the adjoint signal is indeed due to waves: Dynamical sensitivity (a) vs. kinematic sensitivity (b) (see equations 6, 7) 8 years before the time of the cost function evaluation. Dynamic sensitivity which corresponds to wave motions that vertically move the isopycnals is significantly larger than kinematic sensitivity which corresponds to long-isopycnal advection which does not change the density field.

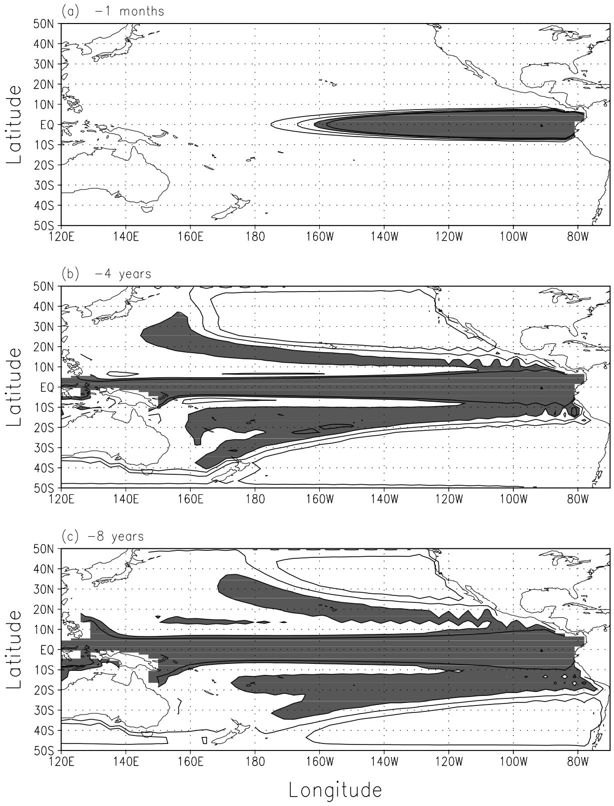

FIG. 6. Sensitivities to temperature perturbations at a depth of 200 meter, for the idealized model with horizontally uniform stratification. (a) 1 month, (b) 4 years , and (c) 8 years before the time of the cost function evaluation. Contour intervals in panels (a), (b), and (c) are 0.001, 0.00075, and 0.0005, respectively. Values larger than 0.003, 0.002, and 0.0015 are shaded with dark gray in panels (a), (b), and (c), respectively.

Another issue of importance is the relevance of the adjoint sensitivities to the actual ocean dynamics. That is because the adjoint model indicates what are the perturbations to which the sensitivity is maximal, yet does not provides any information on whether such perturbations are likely to occur. Given that we see sensitivities to upper ocean temperature perturbations in the mid-latitude Pacific ocean, we can be fairly confident that such perturbations will indeed occur due to natural decadal variability in that area. It is therefore likely that the sensitivity we see here will be excited by temperature anomalies that naturally occur, and is therefore physically relevant.

c. What sets the path of propagation of the sensitivities?

An a-priori consideration of the sensitivity problem would lead one to the expectation that Rossby waves from the entire mid-latitude Pacific ocean should propagate westward until they reach the western boundary. From that point the signal can propagate to the equator, and there be transformed into an equatorial kelvin wave which affects the thermocline structure. Why then is it that only certain latitude bands around 15°N and 12°S affect the equator in our sensitivity runs? In order to address this question, we run an experiment in which the ocean model has the same geometry and bathymetry. The temperature initial conditions were set to a horizontally uniform idealized vertical profile that mimics a mixed layer (150 m deep), a main thermocline (at a depth of 200 m) and a weakly stratified deep ocean. The salinity was set to a uniform value of 35 PSU. No wind is applied. The adjoint of this model was then run with a similar cost function to that used above, centered at the depth of the idealized thermocline in the East Pacific.

Fig. 6 shows that in this model the sensitivities indeed propagate from all latitudes as Rossby Waves and affect the Eastern pacific thermocline. However, all sensitivities decay in the model within 2-3 years, unlike the case in our model with observed climatological background (Fig. 2), where these sensitivities persist for 10-15 years. Another difference is that sensitivities in our standard adjoint model run are restricted to two bands at 15°N and 12°S, while in the idealized model they are spread over more latitudes. A final difference between the standard and idealized runs is that the sensitivities in the standard run propagate eastward along 15°N and then turn northward up to 25°N, while in the idealized model the propagation is purely eastward.

We will show below that baroclinic instability amplifies the sensitivities in our standard adjoint model run. Given this information and the results of the idealized experiment we learn two important lessons. First, that we see significant sensitivities only at 15°N (and 12°S) because there they are amplified by baroclinic instability. In terms of the forward model dynamics, Rossby waves that start everywhere else are damped along their path to the western boundary and then to the equator, while those starting along 15N°(and 12°S) are amplified by baroclinic instability and therefore survive and manage to get to the equator. Baroclinic instability exists along 15°N (and 12°S) because of the horizontal variation in the stratification and corresponding vertical shear due to the oceanic mid-latitude wind driven gyres. The second lesson we learn here is that the specific curved path taken by the sensitivity waves along 15°N (and 12°S) toward 25°N and 25°S is again due to the structure of the background circulation and density field felt by the propagating waves, and imposed by the mid-latitude gyre circulation.

d. Sensitivities along the equator - the mid-latitude–equator connection

So far we showed the sensitivity of the equatorial Pacific sub surface thermal structure to mid-latitude perturbations at a time scale of a few years, but we are yet to show where and how these perturbations affect the equatorial region. Fig. 7 shows the sensitivity of the sub-surface east Pacific thermocline (i.e. the cost function, egn 1) to temperature perturbations along the equator at a depth of 2200m, for the first 24 months prior to the cost function evaluation. The thick black lines indicate the approximate propagation of the sensitivities with time and longitude. The 2000m depth is chosen because the wave signal is the clearest there. It can be seen that the subsurface temperature (cost function) is sensitive to different baroclinic Kelvin modes that travel all the way from the western Pacific (around 140°E). These modes propagate with different speeds and therefore affect the cost function region at different times.

Some previous studies tried and failed to find correlations between mid-latitude perturbations and equatorial sub-surface temperature signal. they concluded that the oceanic link from mid-latitudes to the equator is weak or non existent. We also were forced here to plot the sensitivities at a depth of 2km in order to see a coherent link between mid-latitudes and the equator. One clearly does not expect such depths to play a significant role in decadal variability. However, Note that in our sensitivity runs the mere fact that the sensitivity signal reached the mid-latitudes indicates that there is some link between the equator and the mid-latitudes, because there is nothing else that can excite mid-latitudes sensitivities in our adjoint model run. This is because the cost function is centered at the equator, and is the only forcing felt by the adjoint model run. It therefore seems that although it is difficult to follow specific anomalies from the mid-latitudes to the equator, the teleconnection between the two regions still exists.

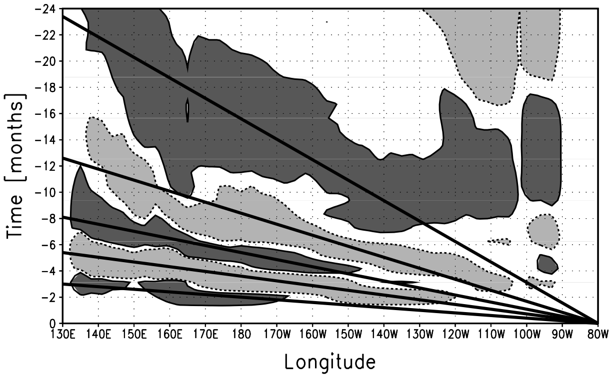

FIG. 7. Sensitivity to temperature perturbations along the equator at depth of 2200 m, as function of months prior to time of cost function evaluation. Values larger (smaller) than 0.001 (-0.001) are shaded with dark (light) gray. The thick black lines indicate the approximate propagation of the sensitivities with time and longitude.

We next try to identify the connection path between the sensitivities showing up along 15°N and those seen earlier at the equator. Fig. 8a shows the sensitivities along the equator during a 12 year adjoint model run; Figure 8b shows the sensitivities at the region of the western boundary of the Pacific, 140°E, from the equator to 15°N; and Fig. 8c shows the sensitivities along 15°N, from 140°E to 80°W. The three panels illustrate the wave path from the 15°N region to the east equatorial region. Following the sensitivities backward, from panel (c) to panel (a) (forward in real time), we can see that a major part of the perturbations that start their way as long mid-latitude Rossby waves travel westward to the western boundary (panel c), then travel as coastal Kelvin waves from 15°N to the equator (panel b), and eventually travel eastward as equatorial Kelvin waves to reach the eastern Pacific and affect the thermal structure there (panel a).

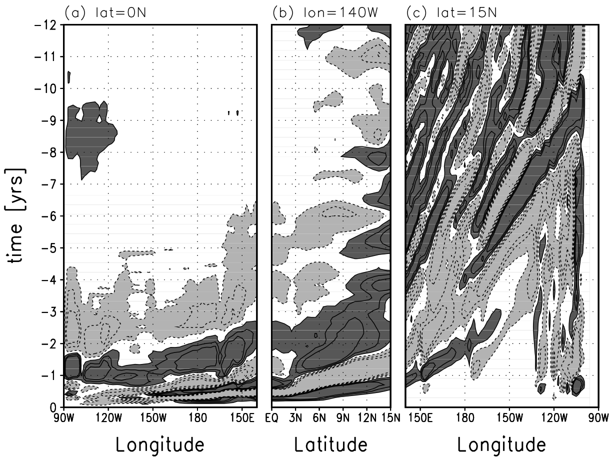

FIG. 8. The connection between the equator and 15°N: the time-space sensitivity to temperature perturbations at depth of 2200 m. (a) sensitivities along the equator (note that longitude axis is reversed). (b) sensitivities along 140°E between 0°N and 15°N. (c) Sensitivities along 15°N. Values larger (smaller) than 0.005 (−0.005) are shaded with dark (light) gray.

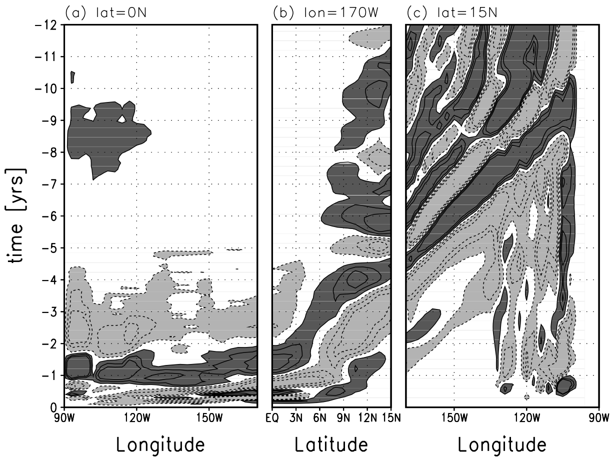

FIG. 9. As in Fig. 8, but for a connection along 170°W. (a) sensitivities along the equator (note that longitude axis is reversed). (b) sensitivities along 170°W between 0°N and 15°N. (c) Sensitivities along 15°N. Values larger (smaller) than 0.005 (−0.005) are shaded with dark (light) gray.

Some of the mid-latitude Rossby wave sensitivities seen in Fig. 8c cannot be related to the above scenario. They seem to be transmitted from the equator to 15N along 170°W as seen in Fig. 9a-c. The precise mechanism that allows this teleconnection is not clear, and may have to do with a distortion of the background potential vorticity field which allows the mid-latitude Rossby wave energy to leak from the mid-latitudes toward the equator before reaching the western boundary.

4. An eigenmode stability analysis in the QG regime

The objective of this section is to demonstrate the role of baroclinic instability in amplifying the sensitivities and shaping their path, as hypothesized in the previous section. We do this by assuming that the sensitivities are locally governed by quasi-geostrophic (QG) dynamics, solving for the QG normal modes based on the forward model climatology, and comparing the eigenmode solutions to the structure of the adjoint sensitivities.

Liu (1999b) showed that in the presence of a background shear flow, instead of the usual baroclinic modes, one finds two sets of modes: "non-Doppler-shifted" modes which resemble the usual free modes, and "advective" modes that tend to propagate following the path of the mean flow (see also Liu 1999a). The waves we see in the adjoint sensitivities seem to be of the advective kind, as they follow closely the mean gyre circulation. In addition to these complications due to the existence of a mean shear, we are also concerned with baroclinic instability and in particular with the existence of critical layers which seem to dominate the structure and growth of our adjoint sensitivity signal.

First, let us define the appropriate variables for the QG theory:

$$\begin{aligned} \rho &= \rho_0 + \bar{\rho}(\mathbf{x}) + \rho'(\mathbf{x},t) && (8) \\ (u,v) &= (\bar{u}(\mathbf{x}), \bar{v}(\mathbf{x})) + (u'(\mathbf{x},t), v'(\mathbf{x},t)) && (9) \\ \psi &= \bar{\psi}(\mathbf{x}) + \psi'(\mathbf{x},t) && (10) \end{aligned}$$

where $\mathbf{x} = (x,y,z)$; $\rho, (u,v)$ and ψ are the density, horizontal velocity, and stream function fields. The averaged densities ρ_0 and $\bar{\rho}(x,y,z)$ were calculated from the model climatological temperature and salinity. The variables $\bar{u}$, $\bar{v}$ are the model climatological horizontal velocities. The buoyancy frequency $N(z)$ was calculated according to

$$N^2 = -\frac{g}{\rho_0}\frac{\partial\bar{\rho}}{\partial z}. \qquad (11)$$

The buoyancy frequency N^2 is treated as if it were only a function of z when taking horizontal derivatives, following the QG approximation. We have set $N^2(z)$ to be no smaller than $10^{-7} sec^{-2}$ (Killworth et al. 1997), and in the mixed layer region to be no smaller than $10^{-4} sec^{-2}$.

Noting that

$$u' = -\frac{\partial\psi'}{\partial y},\ v' = \frac{\partial\psi'}{\partial x};\ \rho' = -\frac{\rho_0 f_0}{g}\frac{\partial\psi'}{\partial z}, \qquad (12)$$

the quasi-geostrophic potential vorticity (PV) equation in the presence of background velocities (and horizontal density gradients) is

$$\left(\frac{\partial}{\partial t}+\bar{u}\frac{\partial}{\partial x}+\bar{v}\frac{\partial}{\partial y}\right)\Big[\frac{\partial^2\psi'}{\partial x^2}+\frac{\partial^2\psi'}{\partial x^2} \tag{13}$$

$$+\frac{\partial}{\partial z}\left(\frac{f_0^2}{N(z)^2}\frac{\partial\psi'}{\partial z}\right)\Big]+\frac{\partial\psi'}{\partial x}\frac{\partial\bar{\Pi}}{\partial y}-\frac{\partial\psi'}{\partial y}\frac{\partial\bar{\Pi}}{\partial x}=\nu\nabla^4\psi'$$

where

$$\bar{\Pi}=f+\beta y+\left(\frac{\partial\bar{v}}{\partial x}-\frac{\partial\bar{u}}{\partial y}\right)-\frac{\partial}{\partial z}\left(\frac{f_0^2}{N(z)^2}\frac{g}{\rho_0 f_0}\bar{\rho}\right) \tag{14}$$

is the background potential vorticity. The term on the *rhs* represents the model eddy-viscosity, where $\nu = 2\cdot 10^4 m^2 sec^{-1}$ is the model horizontal viscosity coefficient. Assuming a solution of the form

$$\psi' = e^{i(kx+ly-\omega t)}h(z), \tag{15}$$

with the boundary conditions being

$$\frac{\partial\psi'}{\partial z}=0 \qquad at\ z=0, z_B, \tag{16}$$

we can write (13) as

$$\frac{\partial}{\partial z}\left(\frac{f_0^2}{N(z)^2}\frac{\partial h}{\partial z}\right)-(\bar{u}k+\bar{v}l-\omega)^{-1}\times \tag{17}$$

$$\Big((\bar{u}k+\bar{v}l-\omega)^2(k^2+l^2)+k\frac{\partial\bar{\Pi}}{\partial y}-l\frac{\partial\bar{\Pi}}{\partial x}$$

$$+\nu(k^2+l^2)^2\Big)h=0,$$

which is the familiar eigen-problem, ω being the eigenvalue and $h(z)$ being the eigen function. We chose to solve the eigen-problem by writing the derivative in z in centered finite difference form and rearranging the equation into a matrix form of a generalized eigen problem

$$Ah=\omega Bh. \tag{18}$$

We solved (18) at each horizontal model grid point, with various choices for k and for $l = 2\pi/50°$ (reflecting the roughly westward average direction of propagation of the adjoint sensitivities). The imaginary part of the eigen frequency from the solution of the eigen problem as function of k and for all horizontal locations in the region 10-20°N and 170-180°W is shown in Fig. 10. There is a maximum growth at a wavelength around 5°. As expected, the solutions of (18) are not simply structured normal modes, but have a more complicated structure due to the background shear, and especially a result of the existence of critical layers. The fastest westward propagating modes are now not necessarily those of a less complex vertical structure (as opposed to the classical normal modes theory) (e.g. Killworth et al. 1997). In any case, our interest here is in finding the eigen solutions that are unstable and growing (like the adjoint sensitivities) and that have a similar vertical structure to that of the adjoint sensitivities.

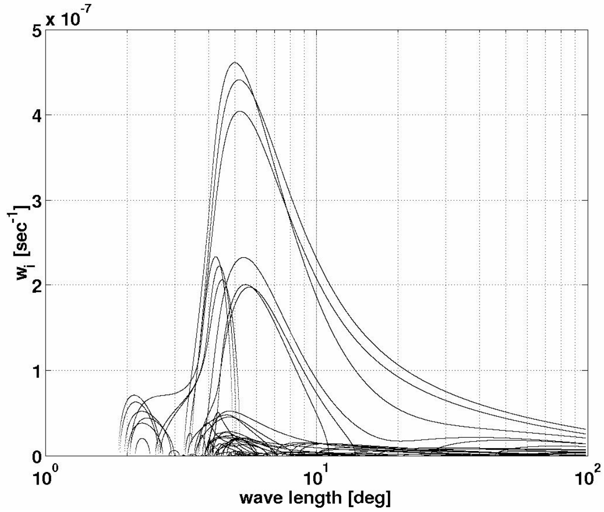

FIG. 10. The imaginary part of the eigen frequency, ω_i, from the solutions of the eigen problem as function of k, for all horizontal locations in the region 10-20°N and 170-180°W. Only the unstable normal modes with a maximum amplitude below 100m are plotted here, eliminating the surface trapped modes that are not relevant to the adjoint sensitivity solution.

Consider now eigen-solutions whose eigenvalue is complex (unstable modes). If a complex eigenvalue exists, there also exist a complex eigenvector, so that (15) may be written as

$$\psi' = [h_R(z)+ih_I(z)]\,e^{\omega_i t}e^{i(kx+ly-\omega_r t)}. \tag{19}$$

Rearranging (19) to separate the real part we find

$$\psi'_r = \left[h_R(z)^2+h_I(z)^2\right]^{\frac{1}{2}}e^{\omega_i t}\cos(kx+ly-\omega_r t+\phi(z)), \tag{20}$$

where

$$\phi(z)=\tan^{-1}\frac{h_I(z)}{h_R(z)}. \tag{21}$$

We can now plot the unstable solution (20, 21) from some specific (x,y), reconstructed over a range of longitude (x) values, as seen in Fig. 11a based on the unstable solution at 180°W and 15°N. Panel (b) of the same figure shows the wave-mean flow energy transfer by the unstable waves, i.e. the term $\overline{v'T'}\partial\bar{u}/\partial z = \overline{\psi'_z\psi'_x}\partial\bar{u}/\partial z$ (Pedlosky 1987), while panel (c) displays the term $\bar{u}+\bar{v}l/k-\omega_r/k$ from (17), showing where critical

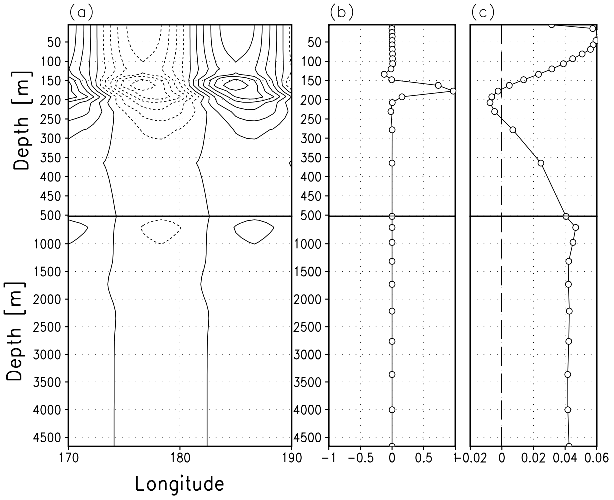

FIG. 11. (a) Reconstructed (in zonal) unstable solution of 180°W 15°N, with zonal wave length of 15°. (b) the wave-mean flow energy transfer $\overline{v'T'}\partial\overline{u}/\partial z$ corresponding to the unstable waves. Note the large energy conversion at the critical layer at roughly 150m depth. (c) $\overline{u}+l/k\cdot\overline{v}-\omega/k$ as function of depth. Note that the vertical axis scale is different between 1-500m and 500 4500m.

layers occur (note that the vertical shear at the latitude bands we are mostly interested in, is dominated by $\overline{u}$, so that the critical layers basically occur when $\overline{u}-\omega/k$ vanishes). The eigenvalue of the unstable solution divided by k is composed of the real $c_r = \omega_r/k = 0.04 m\cdot sec^{-1}$ and imaginary $c_i = \omega_i/k = 0.0016 m\cdot sec^{-1}$, so that the requirement that the imaginary part is much smaller than the real part is satisfied, and the critical layer analysis can be applied (Pedlosky 1987).

There are a few things to note in Fig. 11. First, at the depth range where $\partial\overline{u}/\partial z$ is negative (200-500m) the eigen solution is tilted in many horizontal locations to the east, according to the necessary condition for baroclinic instability (Pedlosky 1987, section 7.3). Second, at a depth of 150m, where there exist a critical layer ($\overline{u}k+\overline{v}l-\omega=0$), there also exists a large energy transfer from the mean flow to the waves (Fig. 11b), as expected for baroclinic instability near a critical layer (Pedlosky 1987, section 7.8). Moreover, the solution is tilted strongly to the west. This is expected to happen in the vicinity of a critical layer if $\partial\overline{u}/\partial z$ is positive (Pedlosky 1987, section 7.8), as indeed occurs at the depth of 150m, near the critical layer in Fig. 11c. The values of ω_i (Fig. 10) indicate that the e-folding growth time for perturbations is of the order of 1 year. However, it turns out that the most unstable modes are actually surface trapped, while the normal modes that have larger amplitude at the depth range of 100-300m, where the sensitivities have a maximum amplitude, have a growth time an order of magnitude longer, and a less obvious peak as function of k than seen in the modes that dominate Fig. 10.

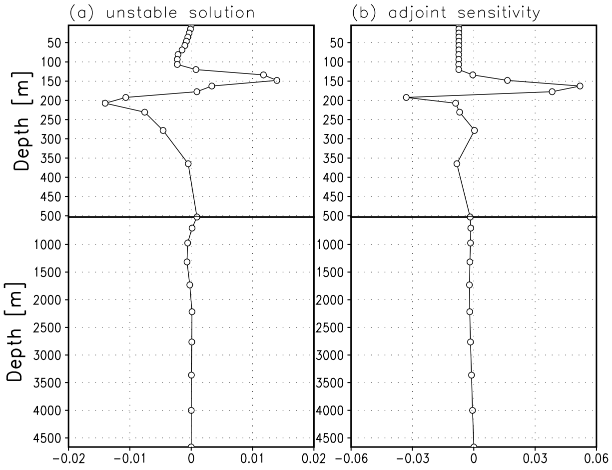

FIG. 12. (a) Vertical structure of temperature anomalies based on the normal mode solution of (18), $T' \sim \frac{1}{\alpha}\frac{\partial\psi'}{\partial z}$, of an unstable solution at 180°W 15°N. (b) The adjoint-calculated sensitivity to temperature perturbations at 15°N, 7 years before time of cost function evaluation.

The sensitivities we see in the adjoint model run (Fig. 2) have a wavelength of about 10-15°. This wave length does not change when we double the various characteristic lengths defining the longitudinal, meridional, vertical and temporal extent of the cost function (1). It therefore seems that the wavelength of the sensitivities is a property of the medium in which the sensitivities propagate. However, even when eliminating the surface trapped modes of the unstable modes (Fig. 10), there is no clear maximum at 15°, but rather a weak peak at 5°. This discrepancy might be a result of the model horizontal resolution which is of 3°; Such a resolution do not permit wavelengths of less than about 15°(5 grid points per wavelength), therefore making the 15°wavelength the most unstable wave in the adjoint solution.

The adjoint sensitivities to temperature perturbations, $(\partial J/\partial T)_S$, are governed by the same dynamics of actual temperature perturbations. Now, the QG stream function calculated in the eigen-problem (18) is related to the temperature roughly as $\psi'_z \sim \rho' \sim \alpha T'$. In order to compare the vertical structure of the unstable mode with the adjoint sensitivity, we therefore need to plot both

$$\left(\frac{\partial J}{\partial T}\right)_S; \quad \frac{1}{\alpha}\frac{\partial\psi'}{\partial z}. \tag{22}$$

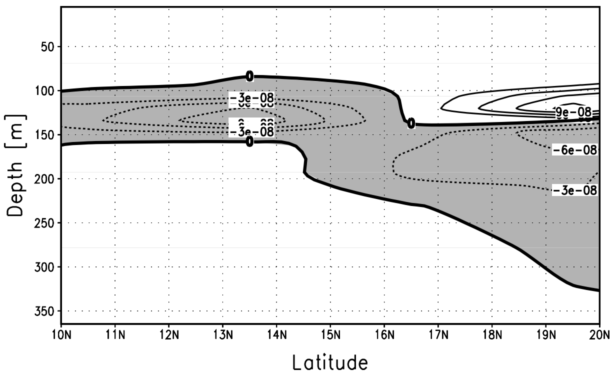

FIG. 13. A meridional cross section of the background meridional PV gradient $\partial\Pi/\partial y$ at 180°W, between 10°N and 20°N. Negative values are shaded with gray.

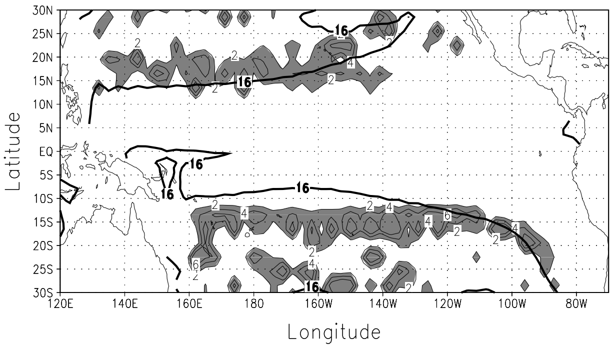

FIG. 14. Maximum imaginary frequency ($\omega_i sec^{-1}$). Values larger than $5 \cdot 10^{-8} sec^{-1}$ are shaded with dark gray, and contour interval is $5 \cdot 10^{-8} sec^{-1}$.

Fig. 12 shows the unstable solution of Fig. 11a, at 180°W, along with a snapshot of the adjoint temperature sensitivity at the same location, seven years prior to the time of the cost function evaluation. The similarity of the two, in particular around the depth of the critical layer makes a very strong case that our adjoint sensitivities are indeed strongly affected by the presence of the critical layer. We note, however, that the normal modes and the adjoint sensitivity do not resemble each other at all times and locations as they do in this figure. The robust result, however, is that both have maximum amplitude at the same depth range and some abrupt vertical gradient near the depth of the critical layer at each horizontal location.

As another test of our hypothesis that the adjoint sensitivities, and therefore the mid-latitude to tropics waves teleconnection mechanism, are strongly influenced by baroclinic instability, we examine whether the necessary conditions for instability are fulfilled. First, Fig. 11b shows that the vertically integrated energy transfer from the mean flow to the wave is positive, therefore the wave can be baroclinicly unstable. Second, we plot the meridional gradient of the background PV ($\partial\Pi/\partial y$) at 180°W (Fig. 13). It can be seen that the necessary condition for instability, requiring that $\partial\Pi/\partial y$ change sign, and therefore vanish on a line in the meridional section (Pedlosky 1987, p. 440), is fulfilled. Third, Fig. 14 shows the maximum imaginary eigen value ω_i as function of location of solution. Again there is a correspondence between the location of unstable regions calculated by the normal mode analysis and between the location of the strongest sensitivities calculated by the adjoint model.

In addition to the instability regions relevant to our sensitivity adjoint model results at the equatorward part of the subtropical gyres around 15N and 12S, our analysis also reveals instability regions at the poleward edges of the subtropical gyres. The reason these regions do not appear as clearly in the adjoint sensitivities is perhaps that the Rossby waves amplified there need to travel a longer distance toward the equator and manage to be damped before getting there.

We conclude this section in noting that all the analyzes performed here strongly support the role of baroclinic instability in shaping the structure and path of propagation as hypothesized in section 3c.

5. Conclusions

We proposed a specific novel mechanism for an ocean wave teleconnection between the mid-latitude Pacific and the equator. According to this mechanism, baroclinically unstable areas of the sub-tropical gyre amplify waves passing via these areas. As a result, these amplified waves dominate the mid-latitude signal at the equator. To do this analysis we have used the adjoint method of sensitivity analysis, as well as a quasi-geostrophic normal mode stability analysis. The comparison between the results of these two tools was especially useful in demonstrating the role of baroclinic instability in amplifying the sensitivity signal arriving at the equator from the mid-latitudes. We demonstrated that critical layers due to the vertical shear of the sub-tropical gyre circulation in the baroclinically unstable areas play an important role in shaping the instability characteristics, and the structure of the sensitivity signal seen in the adjoint model results.

Upon arrival to the equator, the mid-latitude planetary waves can alter the stratification along the equator, and thus create a decadal variability due to decadal-scale signals arriving from mid-latitudes. We did not deal with the question of what generates the mid-latitude decadal signal, and many possibilities have been proposed in the literature (e.g. Gu and Philander 1997; Latif and Barnett 1994).

Our sensitivity analysis tool could in principle indicate also that the equatorial Pacific is sensitive to advection of mid-latitude water, but showed a preferred ocean wave teleconnection. We verified that the sensitivity signal is our model is indeed due to waves by calculating dynamic (due to wave motion that moves the isopycnals) vs kinematic (due to long-isopycnal advection) sensitivities (Marotzke et al. 1999). We also conducted an idealized model run to demonstrate that in the absence of baroclinically unstable regions it is difficult for mid-latitude waves to efficiently affect the equatorial Pacific.

It is obviously possible that some specific characteristics of our results are affected by the particular model used here. For example, the location and extent of the baroclinically unstable mid-latitude regions could be different had we used a different viscosity. Similarly, advection might have been more dominant in a higher resolution model. However, we feel that the basic message here, of a wave teleconnection involving amplification by baroclinic instability, should hopefully be a robust result.

Acknowledgments. We thank Joe Pedlosky for his wonderful GFD book, and Eyal Heifetz for his comments. This study was partially funded by the Office of Global Programs (NOAA), and by the Israeli Science Foundation.

REFERENCES

An, S. I., and B. Wang, 2000: Interdecadal change of the structure of the enso mode and its impact on the enso frequency. *Journal of Climate*, **13**(12), 2044–2055.

Barnett, T., D. Pierce, M. Latif, D. Dommenget, and R. Saravanan, 1999: Interdecadal interactions between the tropics and midlatitudes in the pacific basin. *GRL*, **26**(5), 615–618.

Capotondi, A., and M. A. Alexander, 2001: Rossby waves in the tropical north pacific and their role in decadal thermocline variability. *Journal of Physical Oceanography*, **31**(12), 3496–3515.

Esbensen, S. K., and V. Kushnir, 1981: The heat budget of the global ocean: An atlas based on estimates from surface marine observations. Clim. Res. Inst., Tech. Rep. 29.

Galanti, E., E. Tziperman, M. Harrison, A. Rosati, R. Giering, and Z. Sirkes, 2002a: The equatorial thermocline outcropping - a seasonal control on the tropical Pacific ocean-atmosphere instability strength. *J. Climate*, **15**(19), 2721–2739.

Galanti, E., E. Tziperman, M. Harrison, A. Rosati, and Z. Sirkes, 2002b: A study of enso prediction using a hybrid-coupled model and the adjoint method for data assimilation. *Mon. Weath. Rev.*. Submitted.

Giering, R., 1997: Tangent linear and adjoint model compiler, users manual. http://puddle.mit.edu/∼ralf/tamc, Tech. rep.

Giering, R., and T. Kaminski, 1998: Recipes for adjoint code construction. *Acm Transactions On Mathematical Software*, **24**(4), 437–474.

Gu, D., and S. G. H. Philander, 1997: Interdecadal climate fluctuations that depend on exchanges between the tropics and extratropics. *Science*, **275**(7), 805–807.

Hall, M. C. B., and D. G. Cacuci, 1983: Physical interpretation of the adjoint functions for sensitivity analysis of atmospheric models. *J. Atmos. Sci.*, **40**, 2537–2546.

Harper, S., 2000: Thermocline ventilation and pathways of tropical-subtropical water mass exchange. *Tellus*, **52A**(3), 330–345.

Hazeleger, W., M. Visbeck, M. Cane, A. Karspeck, and N. Naik, 2001: Decadal upper ocean temperature variability in the tropical pacific. *Journal of Geophysical Research-oceans*, **106**(C5), 8971–8988.

Jin, F. F., 2001: Low-frequency modes of tropical ocean dynamics. *Journal of Climate*, **14**(18), 3874–3881.

Killworth, P., D. Chelton, and R. D. Szoeke, 1997: The speed of observed and theoretical long extratropical planetary waves. *J. Phys. Oceanogr.*, **27**, 1946–1966.

Kleeman, R., J. P. Mccreary, and B. A. Klinger, 1999: A mechanism for generating enso decadal variability. *Geophysical Research Letters*, **26**(12), 1743–1746.

Latif, M., and T. P. Barnett, 1994: Causes of decadal climate variability over the North Pacific and North-America. *Science*, **266**, 634–637.

Levitus, S. E., 1982: *Climatological atlas of the world ocean*. NOAA Professional Paper 13, US Government Printing Office, Washington DC.

Liu, Z. Y., 1999a: Forced planetary wave response in a thermocline gyre. *Journal of Physical Oceanography*, **29**(5), 1036–1055.

Liu, Z. Y., 1999b: Planetary wave modes in the thermocline: Non-doppler-shift mode, advective mode and green mode. *Quarterly Journal of the Royal Meteorological Society*, **125**(556), 1315–1339.

Lysne, J., P. Chang, and B. Giese, 1997: Impact of the extratropical pacific on equatorial variability. *Geophysical Research Letters*, **24**(21), 2589–2592.

Marotzke, J., R. Giering, K. Q. Zhang, D. Stammer, C. Hill, and T. Lee, 1999: Construction of the adjoint mit ocean general circulation model and application to Atlantic heat transport sensitivity. *J. Geophys. Res.*, **104**(C12), 29,529–29,547.

Munk, W. H., 1981: Internal waves and small scale processes. *Evolution of Physical Oceanography*, Warren and Wunsch, Eds., MIT Press, Cambridge MA., pp. 264–291.

Pacanowski, R. C., and S. M. Griffies, 1999: *MOM 3.0 Manual*, NOAA/Geophysical Fluid Dynamics Laboratory, Princeton, NJ, USA 08542.

Pacanowski, R. C., and S. G. H. Philander, 1981: Parameterization of vertical mixing in numerical models of tropical oceans. *J. Phys. Oceanogr.*, **11**, 1443–1451.

Pedlosky, J., 1987: *Geophysical Fluid Dynamics.*. 2nd ed., Springer-Verlag, Berlin-Heidelberg-New York.

Reynolds, R. W., and T. M. Smith, 1994: Improved global sea surface temperature analyses using optimum interpolation. *J. Climate*, **7**, 929–948.

Roemmich, D., and J. Gilson, 2001: Eddy transport of heat and thermocline waters in the north pacific: A key to interannual/decadal climate variability? *Journal of Physical Oceanography*, **31**(3), 675–687.

Schneider, N., S. Venzke, A. J. Miller, D. W. Pierce, T. P. Barnett, C. Deser, and M. Latif, 1999: Pacific thermocline bridge revisited. *Geophysical Research Letters*, **26**(9), 1329–1332.

Stricherz, J., D. Legler, and J. J. O'Brien, 1997: Toga pseudostress atlas 1985-1994, volume III: Indian Ocean, 155pp. Florida State University, Tallahassee, FL, Tech. Rep. 155 pp.

Stricherz, J. J. O., J., and D. M. Legler, 1992: Atlas of florida state university tropical Pacific winds for toga 1966-1985. Florida State University, Tallahassee, FL, Tech. rep.

Syu, H., and J. Neelin, 2000: ENSO in a hybrid coupled model. Part I: sensitivity to physical parameterizations. *Clim. Dyn.*, **16**, 19–34.

Trenberth, K. E., and J. W. Hurrell, 1994: Decadal atmosphere-ocean variations in the Pacific. *Climate Dynamics*, **9**(6), 303–319.

Zhang, R. H., T. Kagimoto, and S. E. Zebiak, 2001: Subduction of decadal north pacific thermal anomalies in an ocean gcm. *Geophysical Research Letters*, **28**(12), 2449–2452.

Chapter 5:

A study of ENSO prediction using a hybrid-coupled model and the adjoint method for data assimilation

ELI GALANTI AND ELI TZIPERMAN

Environmental Sciences, Weizmann Institute, Rehovot 76100, Israel

MATTHEW HARRISON AND ANTONY ROSATI

NOAA/GFDL, Princeton, New Jersey

ZIV SIRKES

Institute of Marine Science, University of Southern Mississippi, Stennis Space Center, Mississippi

ABSTRACT

An experimental ENSO prediction system is presented, based on an ocean general circulation model (GCM) coupled to a statistical atmosphere, and the adjoint method of 4D variational data assimilation. The adjoint method is used to initialize the coupled model and predictions are performed for the period of 1980 to 1999. The coupled model is also initialized using two simpler assimilation techniques: forcing the ocean model with observed sea surface temperature and surface fluxes, and a 3D variational assimilation method, similar to that used by the US National Center for Environmental Prediction (NCEP) for operational ENSO prediction. The prediction skill of the coupled model initialized by the three assimilation methods is then analyzed and compared. The effect of the assimilation period used in the adjoint method is studied by using 3,6 and 9 months assimilation periods. Finally, the possibility of assimilating only the anomalies with respect to observed climatology, in order to circumvent systematic model biases is examined.

1. Introduction

Much progress has been made during the past decade both in developing a variety of models and theories for El Niño-Southern Oscillation (ENSO) (Neelin et al. 1998), and in the development of data assimilation methods for the initialization of ENSO predictions (Latif et al. 1998). ENSO prediction models range from statistical models, via intermediate reduced gravity models such as that of Zebiak and Cane (1987), hybrid-coupled models, to fully coupled general circulation models.

Prediction models need to be initialized using the observed data, and the choice of the method by which the observations are to be assimilated into the model is of great importance. Data assimilation methods used in tropical ocean models range from simple nudging techniques to sophisticated optimization methods like the Kalman filter and the 4D variational schemes (Ghil and Malanotte-Rizzoli 1991). Data insertion was used successfully in the CZ-model, for example, where the observed winds were used to drive the ocean model (Cane et al. 1986). Next is the nudging method, where the model fields are nudged towards the observed value with a time scale depending on the assumed model and data errors (Chen et al. 1995; Kirtman and Zebiak 1997). Optimal Interpolation (3D variational assimilation, Derber and Rosati 1989) is currently used operationally in the National Center for Experimental Prediction (NCEP, Behringer et al. 1998). Finally, there are the Kalman filter and smoother (Cane et al. 1996; Fukumori and

Malanotte-Rizzoli 1995; Miller and Cane 1989), and the 4D variational assimilation technique (adjoint method) that avoids some of the computational difficulties of the Kalman Filter by not calculating the error covariance matrices.

Adjoint models are now used for 4D variational data assimilation in intermediate and complex models (e.g. Bennett and McIntosh 1982; Bennett et al. 1998; Kleeman et al. 1995; Thacker and Long 1988; Tziperman and Thacker 1989), and for operational weather prediction (Klinker et al. 2000).

The objective of this paper is to study the potential of the adjoint method of data assimilation for ENSO prediction. We use a prediction system based on a hybrid-coupled model and its adjoint. It is our hope that the use of a sophisticated assimilation method applied to a complicated and reasonably realistic ENSO model may lead to improvements in ENSO prediction skill. In order to estimate the performance of the adjoint assimilation in initializing the coupled model for ENSO prediction, we compare it to a 3D variational assimilation method and to a simple nudging technique, all applied to the same model. The adjoint assimilation method is powerful, yet quite complex. Since is has never been applied to the ENSO prediction problem, there is quite a bit of exploration to do in order to tune and optimize the adjoint method for this particular application. We can only start this tuning and optimization process in the present work, as follows. First, we examine the possibility of assimilating only the anomalous observed fields in (the observed fields minus their seasonal climatology) in order to eliminate systematic climatological model bias, and the prediction skill is compared to that of the full field assimilation. Next, we attempt to find the optimal time window over which the observed data is being assimilated, by repeating the prediction experiments with assimilation periods of 3, 6 and 9 months.

The paper is organized as follows: in section 2 the hybrid-coupled model and data used for the assimilation are described. The prediction experiments based on initialization with the forced ocean model (i.e. using insertion technique to assimilate the wind stress, and nudging to assimilate SST) are presented in section 3, and the prediction experiments based on initialization with the 3Dvar method are presented in section 4. Section 5 presents the setup of the adjoint data assimilation, and the prediction experiments based on initialization with the adjoint method are then presented in section 6. We conclude in section 7.

2. The model and data

The ocean-atmosphere coupled model we use and its adjoint were described in details by Galanti et al. (2002), where it was used for an adjoint sensitivity study of the coupled ocean-atmosphere instability dynamics (see also Galanti and Tzipermann 2002). We therefore give here only a brief description of the model.

The ocean model is based on the GFDL modular ocean model (MOM, Pacanowski and Griffies 1999). The model domain is the Indo-Pacific region, 30°E-70°W, and 50°S-50°N. The model resolution is 3° in longitude, 3° going to 1° at the equator in latitude, and 30 depth levels where the top 15 layers are within the top 200 meters of the ocean. The model uses a modified Richardson-number dependent vertical mixing scheme (Pacanowski and Philander 1981; Syu and Neelin 2000), and constant horizontal viscosity and diffusivity.

The statistical atmospheric model is based on a singular vector decomposition (SVD) using the NCEP SST (Reynolds and Smith 1994), and the wind stress and heat fluxes of the ECMWF re-analysis (Gibson et al. 1997). Only the first three SVD modes are used (Harrison et al. 2002). The coupling of the atmospheric variables to the anomalous SST is done between 20°S and 20°N, while outside of this area only the climatological atmospheric fields are used to force the ocean.

The coupled model is run as follows: at each time step, the SST anomalies are calculated with respect to the monthly climatological SST of the uncoupled ocean model. Next, the wind stress and heat flux anomalies are derived from the SST anomalies using the statistical atmospheric model. Finally, the calculated wind stress and heat flux anomalies are added to the monthly climatological FSU wind stress and to the climatological model heat flux, respectively, to be used as forcing for the ocean model.

The model exhibits interannual variability similar to, although weaker than, the observed ENSO variability (see Galanti et al. 2002, for figures). The simulated SST anomalies are mainly in the east and central Pacific, the oscillation time scale is of 3-4 years and the maximum of the warm events is reached during November-December, in a reasonable agreement with observations.

As the main goal of this study to try to understand the effect of the adjoint assimilation on the prediction skill of the coupled model, we chose for the data to be assimilated the three most necessary variables for describing ENSO's dynamics and evolution: the SST, the subsurface temperatures (reflecting the thermocline depth), and the winds. The SST data used here are the weekly NCEP SST (Reynolds and Smith 1994), the subsurface temperature are the daily TAO mooring observations (McPhaden et al. 1998), and the winds are the monthly NCEP reanalysis (Kalnay et al. 1996). The data cover the period of between 1980 and 1999.

3. Prediction with initial conditions from a forced ocean-only simulation

The focus of this study is the comparison of the predictability skill based on initialization using the adjoint method with less complicated methods of data assimilation and initialization. The first initialization considered here is using a forced ocean run as follows. The ocean model, after being spun up, was forced with the NCEP winds, and its SST was restored to the NCEP SST with a 5 day restoring time scale. The model state was saved at the beginning of each month to serve as the initial conditions for ENSO prediction; this type of initialization will be referred to as the "simulation run". Fig. 1 shows the observed heat content initial conditions (integrated from the surface to depth of 250m) along the equator, together with the ocean model heat content obtained using the simulation (panel b). Also shown are the 3Dvar assimilation (panel c), and the adjoint assimilation (panel d), both to be described below. Note that only the heat content initial conditions for January and July are shown, because initial conditions for other months were not calculated with the adjoint method (see section 5b). It can be seen that the initial conditions produced by the simulation run (Fig. 1b) capture some of the observed features of the subsurface temperature along the equator, but in some cases, for example in 1990-1995, it fails to produce the observed subsurface temperature.

Fig. 2a shows 2 year segments of NINO3 index as predicted by the coupled model initialized by January initial conditions from the forced ocean simulation run, compared to the observed NINO3 index. The correlation of the predicted NINO3 index with the observed is shown in Fig. 3a (dashed line), together with the observed persistence (thick solid line). The *rms* error of the prediction (dash) together with the *rms* error of the persistence (thick solid) are shown in Fig. 3b (dashed line). The prediction skill for the first 5 months is similar to that of the persistence, suggesting that the coupled model dynamics are not very influential on this time scale. At time intervals longer than 6 months, the skill of persistence drops while the model prediction shows a correlation of about 0.5; surprisingly, this skill does not drop and remains at that level for the duration of the two year prediction. We will return to discuss this point later on when comparing the different assimilation schemes. The *rms* error of the predictions shows a behavior consistent with the correlation and reinforces the fact that the model prediction skill does not drop significantly at longer lead times. The prediction skill with initialization in July (Fig. 4a and Figs. 5a, 5b) shows a similar picture, except that the skill (of both model and persistence) drops after about 8 months at late winter of the second year (McPhaden et al. 1998).

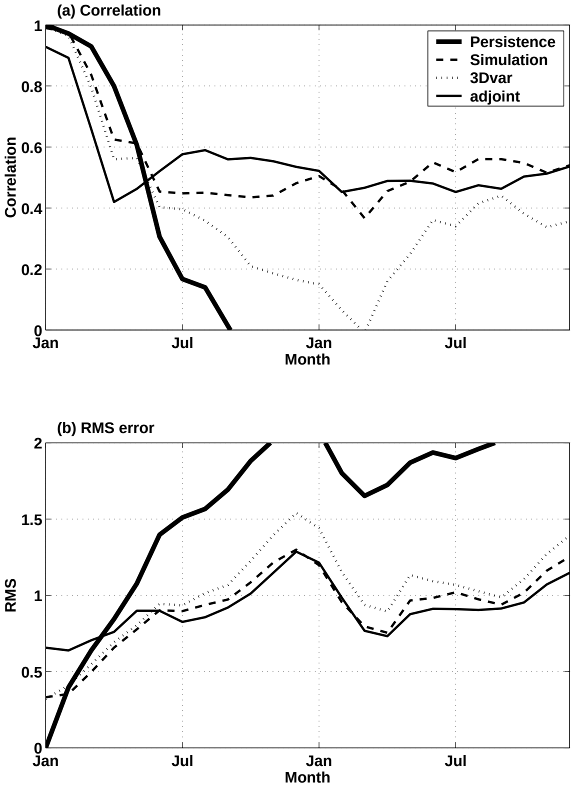

FIG. 3. Prediction skill of the coupled model for the different initialization schemes. (a) Correlation between the predicted NINO3 and the observed as function of the month of prediction. (b) the *RMS* error of the predicted NINO3. Shown are the calculated persistence (thick solid line), prediction with simulation i.c. (dashed line), prediction with 3Dvar i.c. (dotted line), and prediction with adjoint i.c. (thin solid line).

4. Prediction with initial conditions obtained from a 3Dvar assimilation

The next assimilation method to be considered is the 3D variational assimilation, also known as optimal interpolation (Derber and Rosati 1989; Rosati et al. 1997) which is similar to one used today for the NCEP ENSO operational prediction initialization (Behringer et al. 1998). Note that all assimilation methods are applied to the same model in order to enable a consistent comparison

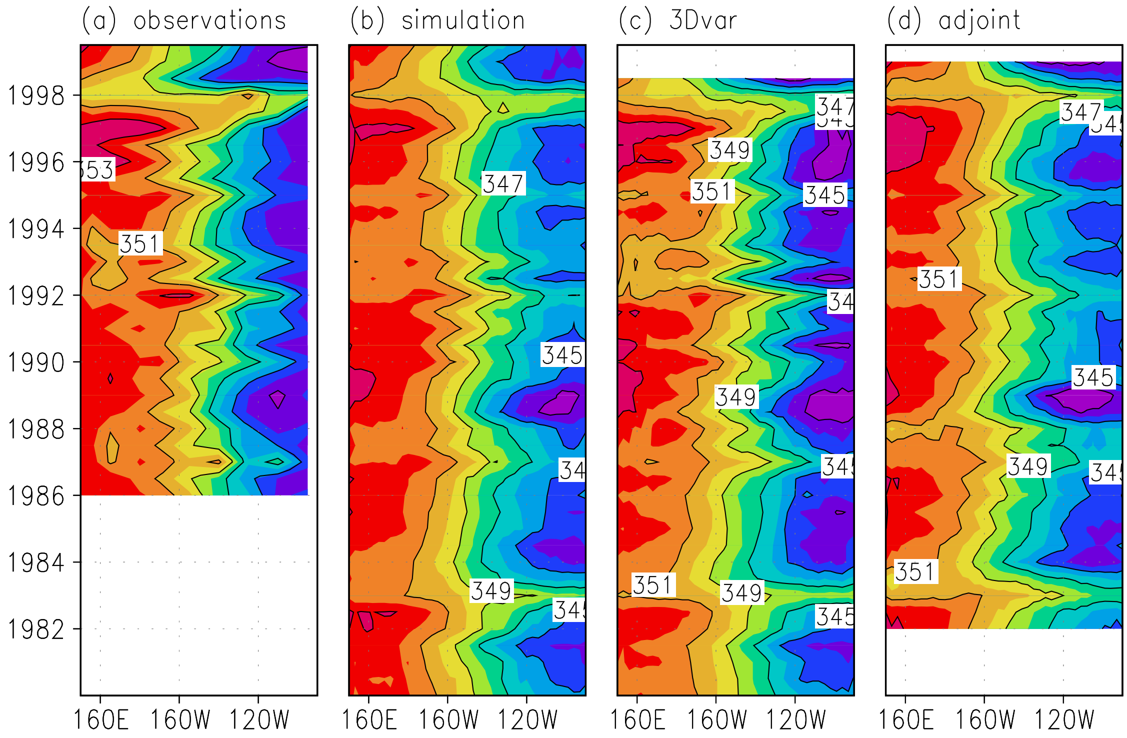

FIG. 1. The ocean model heat content (in $10^9 Jm^{-2}$) along the equator, integrated from the surface to depth of 250m, as obtained from the different initialization schemes: (a) the observed heat content (TAO array), (b) initialization using the forced ocean model, (c) initialization using the 3Dvar assimilation, and (d) initialization using the adjoint assimilation. Contour interval is $2 \cdot 10^9 Jm^{-2}$. The adjoint initialization produces initial conditions every six months (in January and July), and all four plots are therefore given at this temporal resolution.

of the assimilation and prediction skills. The 3Dvar assimilation scheme uses the same SST and winds products as the simulation, as well as the TAO subsurface temperature (see section 2).

Fig. 2b shows the 2 year segments of NINO3 index as predicted by the coupled model with the 3Dvar January initializations. The correlation of the predicted Nino3 index with the observed one is showed in Fig. 3a (dotted line), and the *rms* error of the prediction is shown in Fig. 3b (dotted line). During the first 5 months of the prediction, there is no difference between the skill of the simulation-based prediction (dash) and that of the 3Dvar based prediction (dots); both are similar to persistence (thick solid). From 6 months till the end of the prediction, the 3Dvar has a lower correlation and larger *rms* error compared to the simulation based prediction. The same behavior is seen in the predictions starting in July (Fig. 4c and Figs. 5a, 5b, dotted lines), although to a lesser extent; the correlation drops more than the simulation based prediction and the *rms* error is larger.

Consider the effect of the 3Dvar assimilation on the equatorial heat content initial conditions (Fig. 1c) in comparison to the initial conditions obtained from the simulation run (Fig. 1b), and the observed temperature (Fig. 1a). The assimilation of the subsurface temperature into the model forces the model temperature to get closer to the observed subsurface temperature more than in the simulation run where the model is forced with surface fluxes only. Nevertheless, even within the 6 months prediction period, where the initial ocean state dominates the skill, the 3Dvar assimilation does not improve the prediction skill of the coupled model over the simulation based initial conditions. It therefore seems that the assimilation of the SST into the ocean model is sufficient for forcing both the surface and the subsurface temperature fields which influence the NINO3 index during the first 6 months of prediction. Beyond the first 6 months of the prediction, the coupled model dynamics come into play, and there the assimilation of the subsurface temperature proves to actually degrade the prediction skill. A possible reason for this behavior is the inconsistency of the 3Dvar assimilation with the coupled model dynamics (see section 6b).

The above possible explanations for the low predic-

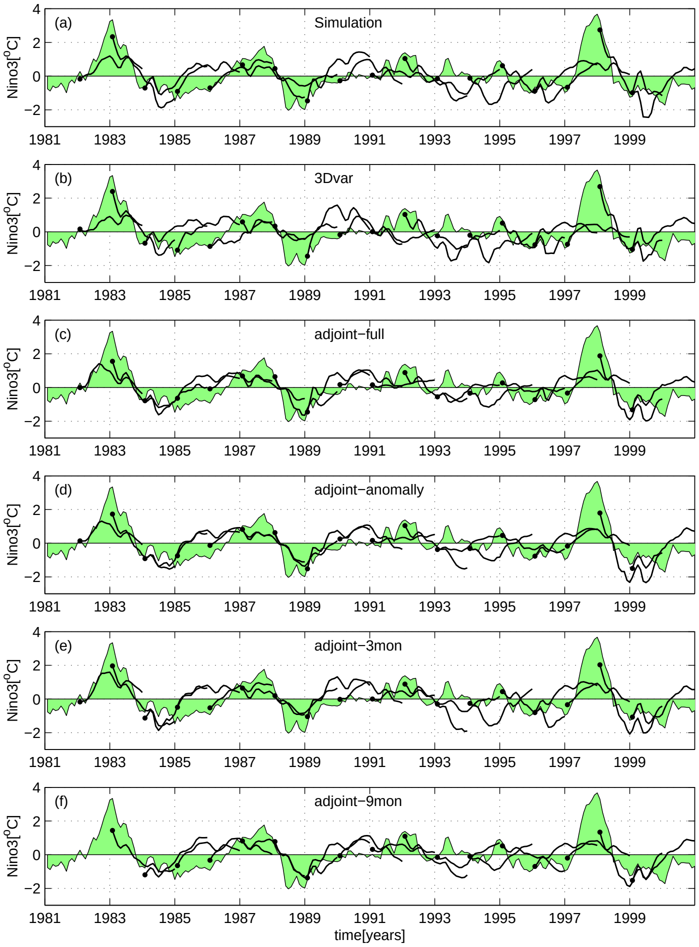

FIG. 2. The NINO3 index as predicted by the coupled model (thick segments), on top of the observed NINO3 index (shaded area); each segment shows 2 years of prediction and the beginning of each prediction is marked with a filled circle. The different panels show the prediction done with initial conditions obtained from the different initialization schemes: (a) simulation (section 3), (b) 3Dvar (section 4), (c) adjoint - full fields (section 6a), (d) adjoint - anomaly (section 6c) assimilation, (e) adjoint - 3 months optimization period (section 6d), and (f) adjoint - 9 months optimization period (section 6d).

tion skill obtained with 3Dvar initialization should be considered especially with respect to the results of Rosati et al. (1997), where the skill of the ENSO prediction based on the same 3Dvar initialization scheme was much better than in our case. There are several possible reasons for this discrepancy: One major difference is that the atmospheric model of Rosati et al. (1997) is a general circulation model, while ours is statistical. Another important difference is that their ocean model horizontal resolution is 3 times finer than ours. These differences and their affect on the prediction skill justify further study, that is out of the scope of the present work. Finally, we note that Rosati et al. (1997) study the predictability for the period 1979-1988, while our prediction period is 1980-1989. We have calculated the skill of our model for the 1980-1988 predictions (not shown) and the skill remained relatively low, so that the slight difference in the period considered does not seem to be significant.

5. Setup of the adjoint assimilation

In this section we describe the setup of the coupled model initialization using the adjoint method (4D variational assimilation). For further discussion of the adjoint method of data assimilation see, for example, Tziperman and Thacker (1989), Tziperman et al. (1992a) or Marotzke (1992).

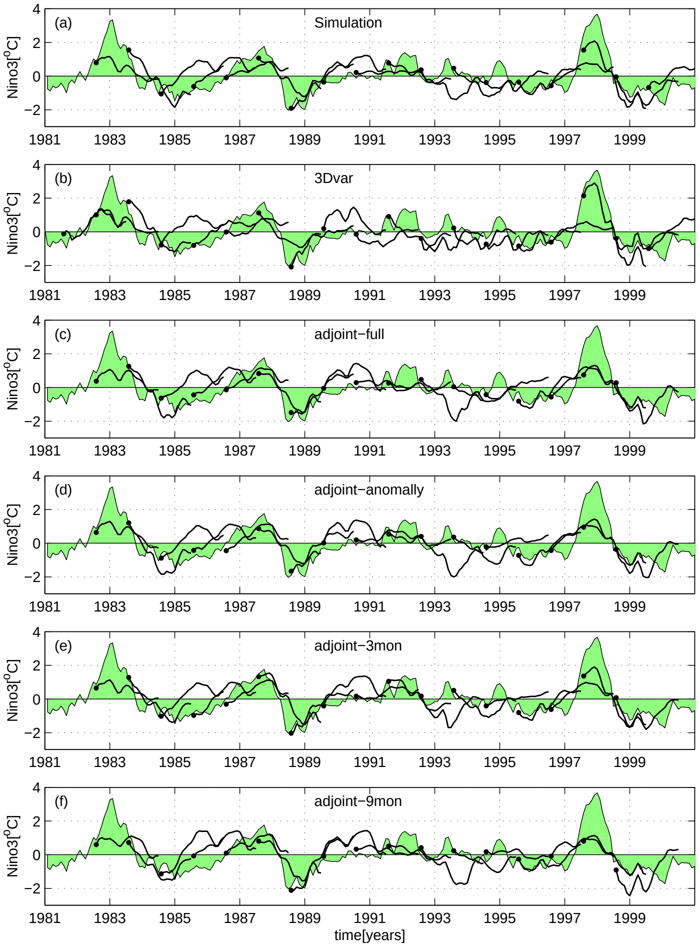

FIG. 4. Same as Fig. 2, but for predictions from July initial conditions.

a. The cost function

The adjoint method of data assimilation is based on the minimization of a cost function, which is a measure of the distance between the model solution and the observations, over a certain spatial and temporal domain. The cost function used in this study is based on the square of the difference between the observations and the model solution for the temperature (T), SST, and wind stress components (τ). Each contribution to the cost function is weighted according to the relevant error estimates (Tziperman et al. 1992a):

$$\begin{aligned}\mathbf{J} = & \sum_i W_i^{TAO}\left[T_i^{TAO} - A_i\left(T^{model}\right)\right]^2 \\ + & \sum_j W_j^{REYNOLDS}\left[SST_j^{REYNOLDS} - B_j\left(SST^{model}\right)\right]^2 \\ + & \sum_k W_k^{NCEP}\left[\tau_k^{NCEP} - C_k\left(\tau^{model}\right)\right]^2 \qquad (1)\end{aligned}$$

where each of the indices i, j, k represents the summation over the spatio-temporal domain of the observations (and wind stress vector components), and the matrices A_i, B_j, C_k transform the model variables into the observations spatio-temporal coordinates i, j, k (Derber and Rosati 1989). The model temperature and wind are bilinearly interpolated to the observational locations from the nearest horizontal points. In the vertical, the observations are interpolated into the model grid.

The weights for the TAO mooring terms are (following Tziperman et al. 1992b)

$$W_i^{TAO} = \frac{dx_i dy_i dz_i}{L_{hor}^{TAO} L_{ver}^{TAO}} \frac{1}{W_s^{TAO}} \frac{1}{(E_i^{TAO})^2} \qquad (2)$$

where $dx_i dy_i dz_i$ is the model grid volume element, $L_{hor}^{TAO} = 400km$ and $L_{ver}^{TAO} = 1/(2 \cdot dz_i)$ are estimated horizontal and vertical correlation length scales, $W_s^{TAO} = 1$ (non dimensional) is the reciprocal of the observation sampling

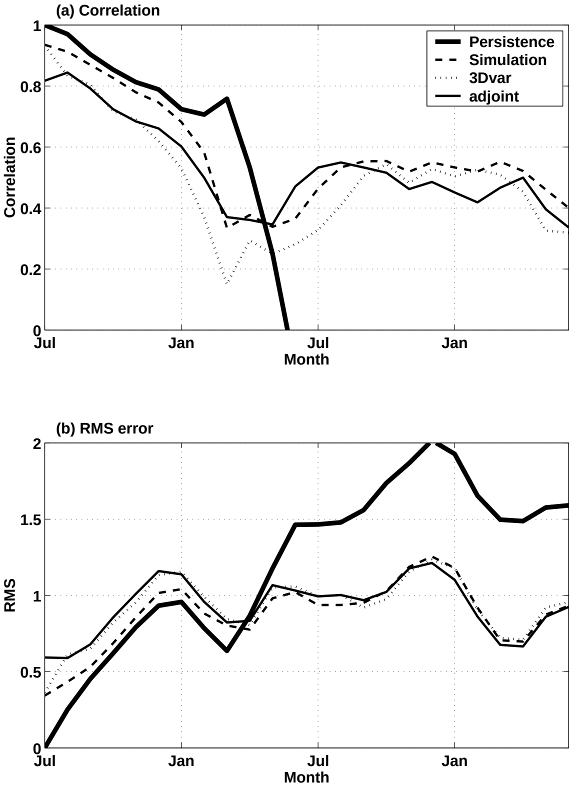

FIG. 5. Same as Fig. 3, but for predictions from July initial conditions.

rate (which is 1/day) normalized by one day, and E_i^{TAO} is the estimated error of the observations. The observational error estimate is set to be the standard deviation of the observed temperature,

$$E_i^{TAO} = STD\left(T_i^{TAO} - \tilde{T}_i^{TAO}\right) \tag{3}$$

where $\tilde{T}_i^{TAO}$ is the observed temperature smoothed by a running average of three months. This error estimate is simply the standard deviation of the high frequency part of the observed temperature. The high frequency variability of the observations cannot be resolved by the hybrid-coupled model, and is therefore treated as a combined observational/model error.

The weights for the Reynolds SST terms are set as

$$W_j^{REYNOLDS} = \frac{dx_j dy_j}{L_{hor}^{REYNOLDS}} \frac{1}{W_s^{REYNOLDS}} \frac{1}{(E_j^{REYNOLDS})^2} \tag{4}$$

where $L_{hor}^{REYNOLDS} = 400km$ is the observations horizontal correlation scale, $W_s^{REYNOLDS} = 1/7$ (non dimensional) is the reciprocal of the weekly observational sampling rate normalized by one day, and $E_j^{REYNOLDS}$ is the estimated error of the observations. The SST error estimate is set to be

$$E_j^{REYNOLDS} = STD\left(SST_j^{REYNOLDS} - \widetilde{SST}_j^{REYNOLDS}\right) \tag{5}$$

where $\widetilde{SST}_j^{REYNOLDS}$ is again the observed SST smoothed by a running average of three months.

The weights for the NCEP wind stress terms are

$$W_j^{NCEP} = \frac{dx_j dy_j}{L_{hor}^{NCEP}} \frac{1}{W_s^{NCEP}} \frac{1}{(E_j^{NCEP})^2} \tag{6}$$

where $L_{hor}^{NCEP} = 1000km$ is an estimated horizontal correlation scale, $W_s^{NCEP} = 1/30$ (non dimensional) is the reciprocal of the observations sampling rate normalized by one day, and $E_j^{NCEP} = 0.1dyn/cm^2$ is the estimated error of the observations.

b. Optimization and prediction procedures

In this study, we choose to regard the model dynamics as strong constraints to the assimilation, i.e. we do not try to correct the model dynamics but optimize only the model initial conditions. There are advantages and disadvantages to the strong constraints assumption, as well as to the weak constraints assumption, where one optimizes some aspects of the model dynamics as well (Bennett 1992). If one's goal is to obtain an optimal estimate of the ocean state, then the weak constraint assumption is perhaps more suitable since it allows for the ocean dynamics to be adjusted to compensate for model errors. On the contrary, if the goal is to predict the state of the Equatorial Pacific ocean-atmosphere system, then the strong constraint assumption may be preferable: with the weak constraint assumption, the model dynamics (mixing parameters, surface fluxes, etc.) are being adjusted during the assimilation, yet we have no knowledge about how to correct the model dynamics during the prediction phase. The result may be an "initial shock" that the coupled model will exhibit in the transition from assimilation to prediction periods. This can be avoided by using the strong constraints assumption, where the same model dynamics are used throughout.

Furthermore, we optimize the initial conditions for the temperature field only. The salinity field is a less important dynamical variable for the Equatorial Pacific than the temperature and the velocity fields adjust to the temperature field within one pendulum day, and therefore need not be optimized for (Rosati et al. 1997; Sirkes et al. 1996). The initial guess for the temperature initial conditions to be calculated by the adjoint iterative minimization is taken as the analysis obtained from the simulation run.

The optimization itself is done using a quasi Newton limited memory BFGS algorithm for the minimization of the cost function (Gill et al. 1981), and we run the optimization for 10 iterations, which was found to be sufficient for satisfactory convergence (section 6). The adjusted optimal initial conditions for the temperature are then used to run the couple model again for the assimilation time interval to obtain the initial conditions for the prediction.

Two approaches to the adjoint methods of data assimilation are examined here. In the first approach, the full observed and model fields are being used in the cost function, while in the second, only anomaly fields with respect to the monthly climatology are used to calculate the cost function. In the first approach, the cost function is constructed from the difference between the observed fields and the model fields, therefore if a seasonal or time independent climatological bias exists in the model, the assimilation process will try to correct this bias. Correcting the model climatological bias, however, might have some undesired effects on the prediction skill, as explained below. In the second approach, the climatology of each field is therefore subtracted (i.e., the model climatology is subtracted from the model solution, and the observed climatology is subtracted from the observed fields). The cost function is now composed of the difference between the anomalous fields, so that the climatological model bias does not affect the assimilation anymore.

Another issue that will be discussed below (section 6d) is the time period over which the assimilation is done. Throughout the paper we will use a time interval of 6 months unless indicated otherwise.

6. ENSO prediction based on adjoint assimilation

In this section we initialize the couple model prediction runs with initial conditions obtained from the adjoint assimilation scheme. Initial conditions are obtained from an adjoint optimization done over the 6 months prior to the time of the initialization, and the cost function is based on the full observed and model fields.

The behavior of the cost function and its components during the optimization is shown in Fig. 6a. The cost function shown is an average over all the January and July adjoint initializations. The cost function value is reduced by a factor of two after ten iterations and the rate of convergence decreases substantially toward the tenth iteration. This may not seem a large reduction, but note that we start the optimization with a fairly good initial guess for the optimal initial conditions, obtained from the forced simulation runs, so we don't expect the optimization to significantly reduce the cost from its initial value. The averaged contribution to the final cost function by the SST penalty terms in (1) is about 60%, the contribution by the TAO array data is about 30%, and the wind penalty terms contribute about 10%. Note that the relative contributions of the SST and the TAO array to the cost function are different during the eighties where most of the cost function is determined by the SST data-model misfit, while during the nineties when the TAO array expanded, the contributions to the cost function by the SST and the TAO array are about the same. Another interesting aspect of the optimization is that the model winds are hardly being optimized (their penalty term is not reduced much by the optimization). There are two reasons for that: one is that the relative contribution of the winds to the cost function is small. The second reason is that the winds derived from the statistical atmospheric model depend on the model SST in a simple and perhaps not very realistic manner. Optimizing the wind therefore implies that the model SST would need to be corrected in a way that deviates from the observed SST. That, in turn, will result in a large increase of the cost function due to the direct SST penalty terms. The optimization therefore prefers the optimization of the SST over the optimization of the winds, explaining the lack of significant reduction in the winds penalty terms. The absolute value of the cost function gradient with respect to the temperature initial conditions decreases during the optimization by a factor of four (Fig. 6b), where most of the reduction occurs during the first 4 iterations.

In the following subsections we discuss several variations in the procedure of the adjoint data assimilation approaches used to initialize the coupled model. We also study the 1997-8 ENSO event as predicted by the coupled model initialized by the different adjoint assimilation variants.

a. Assimilation using the full observed fields

Consider first the prediction skill when the full observed fields are used in the cost function, for January initial conditions (Fig. 2c and Figs. 3a, 3b). In the first 5 months, the correlation between the predicted NINO3 and the observed NINO3 is smaller than that of the prediction based on initial conditions calculated by the simulation run, simply because the adjoint initialization takes into account the model dynamics which prevent the model from getting as close to the observations as in the case of the forced simulation run (section 3, Fig. 3a). During months 6-12 of the prediction, where the model dynamics come into play, the adjoint based prediction has a somewhat better correlation with observations than

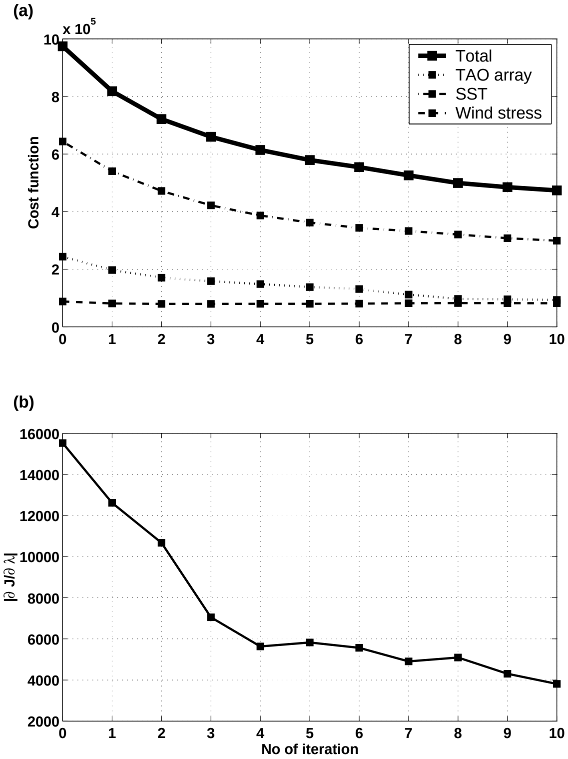

FIG. 6. (a) The reduction in the cost function value and its components as function of number of iterations; The dotted line, dash-dotted line, and dashed line show the contribution of the TAO array, SST, and wind stress to the cost function, respectively. (b) The reduction in the norm of the cost function gradient as function of number of iterations.

the simulation based prediction, however the *rms* error of the prediction is similar in both cases (Fig. 3b). The results from the prediction with July initial conditions (Fig. 4c and Figs. 5a, 5b) show a somewhat different picture. Similar results are found for the January initial conditions, where during the first 6 months the simulation-based prediction has a better skill than the adjoint based prediction, but at longer time scales, the skill of the adjoint-based prediction is similar to that of the simulation-based prediction. This behavior might be a result of the "spring barrier" (Webster 1995); i.e. by the time the model dynamics start to play an important role, the spring barrier erases the additional skill due to the hopefully superior initial conditions calculated by the adjoint method.

The main point of this section is that the adjoint initialization does seem to have the potential for improving the prediction skill of the coupled model, as shown in the case of the January initialization and by the comparison to the 3Dvar scheme. We note that the discrepancies between our results for the 3Dvar initialization and those of Rosati et al. (1997) raise important questions regarding the effects of the model used on the prediction Skill. Therefore, a better evaluation of the prediction skill based on adjoint initialization, especially compared to the 3Dvar assimilation, requires using the higher resolution used in operational prediction, a task which is beyond the scope of the present study.

b. The 1997-8 event

Let us now focus on the 1997-8 event and compare the predictions from initial conditions obtained from the three different assimilation schemes. Fig. 7 shows the temperature at 140W,0N as function of depth as predicted by the coupled model initialized with the three assimilation methods, the simulation, 3Dvar, and adjoint. Also shown is the observed temperature at that location. Looking at the predicted temperature at December 1997, we see the 3Dvar based prediction has the coldest temperature whereas the predicted temperature based on the adjoint initialization is the warmest (and thus closest to the observations).

We now turn to look at the predicted temperature anomalies of the 1997-8 event at the same location (Fig. 8), where the anomalies were calculated with respect to the seasonal prediction climatology of each prediction experiment. It can be seen that the 3Dvar based prediction hardly predicts an event, while the simulation based prediction predicts a weak event, and the adjoint a somewhat stronger and more realistic one (although is fails to switch from the El Niñoevent to the following La Niña).

These results demonstrate the importance of initializing the coupled model in a way that is consistent with the coupled model dynamics. The 3Dvar initialization results in model temperature initial conditions that are the closest to the observations of all three assimilation schemes used here. However, the model climatology has a bias so that its climatology is different from the observed one. As a result, initial conditions that correspond for example to the observed climatology with no anomaly, correspond in the model to the model climatology plus a strong artificial anomaly that is equal to the model bias. Now, the coupling to the atmosphere in the model is done via the SST anomalies, therefore the artificially strong model anomaly is amplified by the ocean-atmosphere coupling and the resulting prediction skill is deteriorated. This error growth mechanism, a combination of the model climatological bias and instability dynamics, may be the reason for the differences between the 3Dvar based prediction skill obtained with our model, and the prediction skill obtained by Rosati et al.

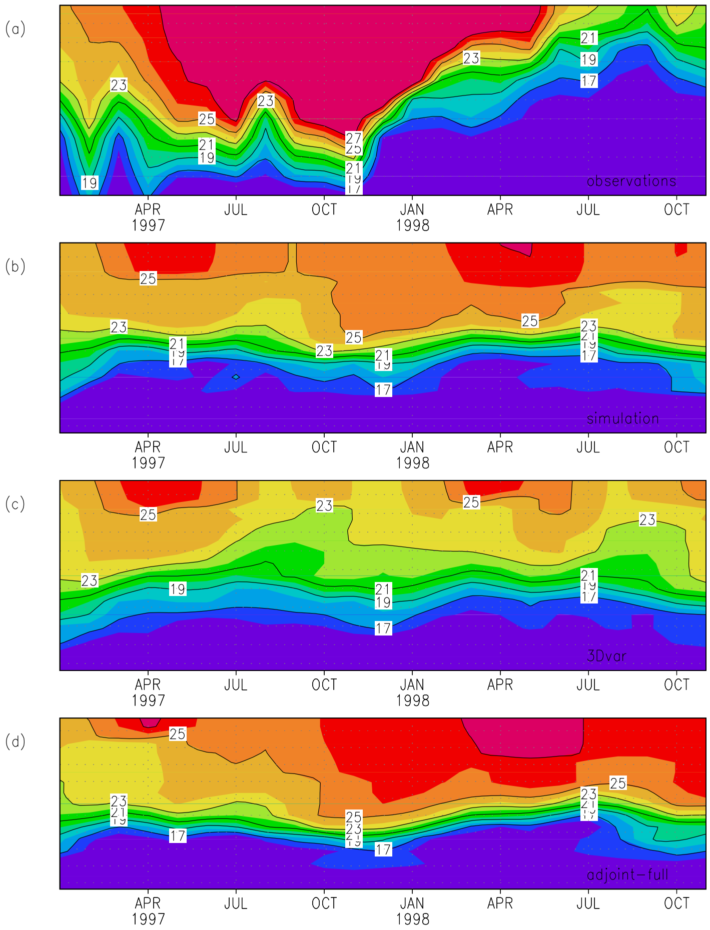

FIG. 7. The prediction of the 1997-8 ENSO event (temperature) at 140W and 0N as function of depth, using January initial conditions obtained from: (b) simulation run, (c) the 3Dvar assimilation, and (d) the adjoint assimilation. Panel (a) shows the observed temperature.

(1997) using a higher resolution model with a smaller climatological bias. The adjoint assimilation, on the other hand, takes into account the errors in the model dynamics and therefore allows only for the part of the observed temperature that is consistent with the model dynamics to influence the model trajectory. The initial conditions are therefore not as close to the observations, but the resulting predictability is somewhat better.

c. *Assimilation using the anomalous observed fields*

In this subsection and the next one, we study various versions of the adjoint assimilation scheme. The prediction skill resulting from the different adjoint assimilation variants is shown in Figs. 9 and 10, and their predicted time series are shown in Figs. 2d-f and 4d-f. In the first variant to be considered here, we modify the cost function to be composed of the difference between the model anomalous fields (calculated with respect to the coupled model monthly climatology) and the observed anomalous fields (calculated with respect to their observed monthly climatology). Comparing the January prediction skill to that of the full fields (Fig. 9), we see that the initialization using the anomalous assimilation improved the prediction skill at time intervals of 3-6 months, and is similar to the prediction skill based on the initialization using the full fields assimilation during other prediction months. The above differences are clearly small, and even less clear in the July experiments (Fig. 10).

The motivation for the assimilation of the anomalous fields comes from the fact that the model climatology is somewhat different from that of the observed data. As explained at the end of the previous section, this results in a deteriorated predictability. The adjoint corrects this to some degree by not getting too close to the observed

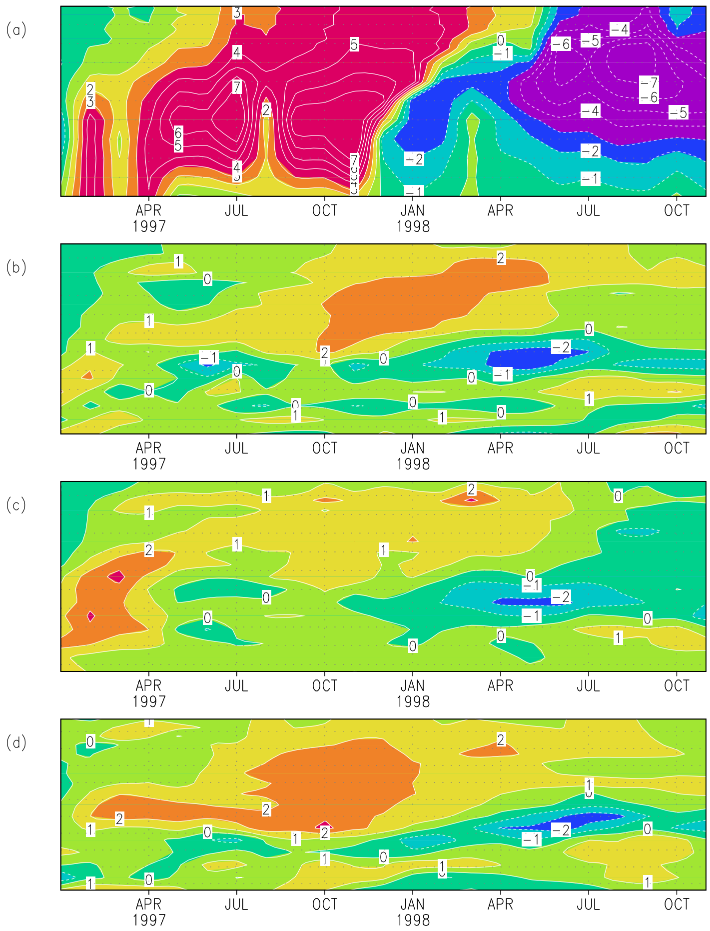

FIG. 8. Same as Fig. 7 but showing the temperature anomalies. Note that the anomalies were calculated with respect to each type of prediction separately.

initial conditions, as explained above. However, this can be further corrected by assimilating only the anomalies with respect to the corresponding climatologies of the model and the data. In this case, the model bias does not enter and does not cause the error growth described above. Note that assimilation of anomalous fields is routinely done with anomaly based models (e.g. Chen et al. 1995) where the assimilation of anomalies is required. But in hybrid-coupled models and fully coupled models, only the full fields are normally assimilated. One may expect the assimilation of anomalies to improve prediction where climatological model bias causes it to deteriorate. Anomaly assimilation is not expected to correct predictability errors due to model bias in the variability rather than in the model climatology. That is, if the model ENSO events are too weak or occur in the wrong place, assimilating the anomalies will not improve the prediction skill.

The results of the anomaly assimilation are clearly not impressive here. It seems that in our model the bias due to the model climatology, which is corrected by the anomaly assimilation, is less significant than the bias in the model variability which is not affected by the anomaly assimilation. We therefore expect that the anomaly assimilation using the adjoint method may actually have the potential to more significantly improve the prediction skill, in situation where the model variability bias is less than in our coarse model. A more thorough examination of the subject using higher resolution models is needed.

d. Optimization period

It is not obvious how one should determine the time interval over which the assimilation should be performed; in general, a too short assimilation period would effectively turn the 4D assimilation into a 3D scheme, thus

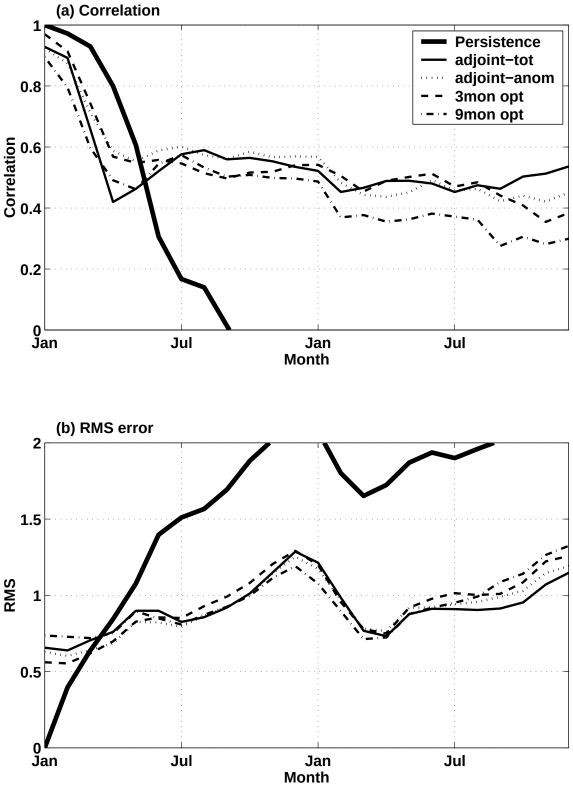

FIG. 9. Skill of the coupled model for the different adjoint initialization schemes. (a) Correlation between the predicted NINO3 and the observed as function of the month of prediction. (b) the *RMS* error of the predicted NINO3. .

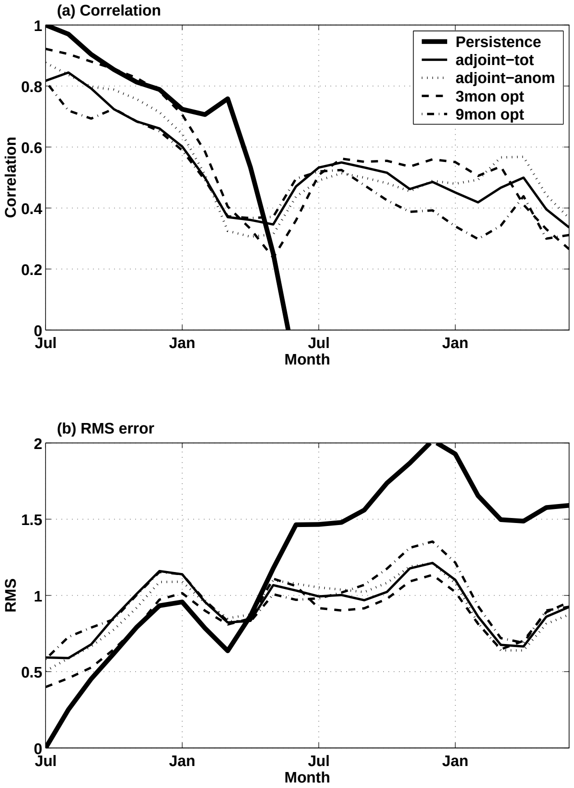

FIG. 10. Same as Fig. 9, but for prediction from July initial conditions.

not taking advantage of the known model dynamics. Using a too long assimilation period, on the other hand, runs into the inherent predictability limits of the system. That is, whether ENSO is chaotic (Jin et al. 1994; Tziperman et al. 1994) or noise driven (Moore and Kleeman 1996; Penland and Sardeshmukh 1995), it has some inherent predictability time scale. If the assimilation period is longer than this time scale, then the initial conditions calculated at the beginning of the assimilation period cannot determine the state of the model at the end of the assimilation period. In this case, the initialization is clearly also meaningless for the prediction period. The standard time interval used in this study is of 6 months. We now repeat the anomalous adjoint assimilation of section c, but with an assimilation period of 3 months (Figs. 2e and 4e). The prediction skill of prediction from January and July initialization are shown in Figs. 9 and 10 (dashed lines) respectively. In both seasons the initialization with 3 months assimilation period is doing better during the first 6 months of the prediction, but at longer times the 6 months assimilation has better skill. A 3 months assimilation period is not enough for the model dynamics to play a significant role, and the initial conditions obtained from the 3 months assimilation are therefore more affected by — and are closer to — the observations. This results in a better skill during the first few months of prediction since the model dynamics are less important then. At longer times (more than 6 months) the model dynamics come into play and the 6 months initialization results in a better skill.

Next, we increase the optimization period to 9 months, and initialize the coupled model with both January and July initial conditions (Figs. 9 and 10, dash-dotted lines). The prediction skill obtained with the 9 months optimization is similar to that of the 6 months optimization, especially at time scales longer than half a year. It seems, therefore, that an assimilation period of 6 months may be near optimal for our model. Lacking, however, a good theoretical understanding of what sets ENSO's predictability time, and therefore what should be the optimal assimilation period, we do not know how robust would this result be to model details such as resolution, etc.

7. Conclusions

In this study we investigated an experimental ENSO prediction system based on an ocean GCM coupled to a statistical atmosphere, and the adjoint method of 4D variational data assimilation. The coupled model is initialized using the adjoint method in order to perform predictions from 1980 to 1999. In order to compare the prediction skill of the system, two simpler assimilation techniques were also used to initialize the coupled model: forcing the ocean model with observed SST, wind stress and surface fluxes, and the 3D variational assimilation method of Rosati et al. (1997). In addition, we examined the issue of the period over which the adjoint assimilation is to be conducted by initializing the model with assimilation periods of 3, 6 and 9 months and comparing the resulting prediction skill. Another issue examined here is the assimilation of the full observed fields vs. the assimilation of the anomalous (with respect to model and observed monthly climatologies) fields.

A comparison between the skill of the coupled model when initialized with the adjoint method, and the skill of the coupled model initialized using a forced ocean model and the 3Dvar assimilation method, shows that the adjoint method does seem to have the potential of improving simpler assimilation schemes. The improved skill is mainly at prediction intervals of more than 6 months, where the coupled model dynamics start to influence the model solution. At shorter prediction time intervals, the initialization using the forced ocean model or the 3Dvar assimilation may result in a better prediction skill. This occurs because both simpler assimilation methods calculate initial conditions that are closer to the observed temperature at the beginning of the prediction period, while the adjoint method allows the initial conditions to deviate further away from the observations, based on the model dynamics. In the first few months of the prediction, the initial conditions dominate the prediction skill and therefore the simpler methods do better. It is also important to note that substantial discrepancies exist between our results for the 3Dvar initialization and those of Rosati et al. (1997) who used a higher resolution ocean model and an atmospheric GCM. This raises important questions regarding the effects of model resolution and atmospheric model used on the performance of the different assimilation schemes considered here, which will need to be addressed in a future studies.

A detailed analysis of ENSO prediction experiments for the 1997-8 event, for which the adjoint method again performed better than the other two schemes considered here, strengthens the above conclusion regarding the potential of the adjoint method.

We explained that defining the cost function to be the difference between the observed and model anomalous fields (with respect to the model and observed climatologies, and instead of using the full fields) may eliminate the effects of systematic model bias and therefore improve predictability skill. In our experiments here, however, the assimilation of anomalies did not have a substantial effect on the prediction skill of the coupled model. This seems to indicate that in our model the bias due to the model climatology, which is corrected by the anomaly assimilation, is less significant than the bias in the model variability which cannot be eliminated using the anomaly assimilation.

Changing the optimization period from 6 months to 3 months and to 9 months showed that the period of 6 months seems to be a near optimal choice for our model. Shortening the optimization period to 3 months resulted in a better skill at short prediction times (up to 6 months), but reduced the skill at longer prediction times. Increasing the optimization interval to 9 months resulted in a reduced skill in all time intervals. Lacking a sufficient theoretical understanding of what sets ENSO's predictability limit, and therefore of the issue of optimal assimilation time, we cannot judge how robust these results are to model details and resolution.

All aspects of initialization and prediction studied here clearly need to be further investigated using higher resolution models in order to optimize the use of the adjoint method for ENSO prediction. This is especially relevant in view of the discrepancies between our results for the 3Dvar initialization and those of Rosati et al. (1997). Nevertheless, we feel that it is reasonable to hope that the adjoint method may out perform other assimilation schemes at higher ocean resolutions, as it did at the coarse resolution used here. The results here therefore seem sufficiently encouraging to justify a further study.

Acknowledgments. This study was partially funded by the Office of Global Programs, NOAA, and by the Israeli Science Foundation. ZS is partially supported by the NOAA CLIVAR Atlantic program.

REFERENCES

Behringer, D. W., M. Ji, and A. Leetmaa, 1998: An improved coupled model for enso prediction and implications for ocean initialization. part i: The ocean data assimilation system. *Monthly Weather Review*, **126**(4), 1013–1021.

Bennett, A. F., 1992: *Inverse methods in physical oceanography*. Cambridge Monographs, Cambridge University Press.

Bennett, A. F., and P. C. McIntosh, 1982: Open ocean modelling as an inverse problem: tidal theory. *J. Phys. Oceanogr.*, **12**, 1004–1018.

Bennett, A. F., B. S. Chua, D. E. Harrison, and M. J. McPhaden, 1998: Generalized inversion of tropical atmosphere-ocean data and a coupled model of the tropical Pacific. *J. Climate*, **11**, 1768–1792.

Cane, M. A., S. E. Zebiak, and S. C. Dolan, 1986: Experimental forecasts of El Niño. *Nature*, **321**, 827–832.

Cane, M. A., A. Kaplan, R. N. Miller, B. Tang, E. Hackert, and A. J. Busalacchi, 1996: Mapping tropical Pacific sea level: Data assimilation via a reduced state space kalman filter. *J. Geophys. Res.*, **101**, 22,599–22,617.

Chen, D., S. E. Zebiak, A. J. Busalacchi, and M. A. Cane, 1995: An improved procedure for El Niño forecasting: Implications for predictability. *Science*, **269**, 1699–1702.

Derber, J., and A. Rosati, 1989: A global oceanic data assimilation system. *J. Phys. Oceanogr.*, **19**, 1333–1347.

Fukumori, I., and P. Malanotte-Rizzoli, 1995: An approximate Kalman Filter for ocean data assimilation: an example with an idealized Gulf-Stream model. *Journal of Geophysical Research-oceans*, **100**(C4), 6777–6793.

Galanti, E., and E. Tzipermann, 2002: A mid-latitude enso teleconnection mechanism via long rossby waves. *J. Phys. Oceanogr.*. Submitted.

Galanti, E., E. Tziperman, M. Harrison, A. Rosati, R. Giering, and Z. Sirkes, 2002: The equatorial thermocline outcropping - a seasonal control on the tropical Pacific ocean-atmosphere instability strength. *J. Climate*, **15**(19), 2721–2739.

Ghil, M., and P. Malanotte-Rizzoli, 1991: Data assimilation in meteorology and oceanography. *Advances in Geophysics*, **33**, 141–266.

Gibson, J., S. Kallberg, S. Uppala, A. Nomura, A. Hernandez, and E. Serrano, 1997: ECMWF reanalysis project report series no.1 technical report 1. ECMWF, Shinfield Park, Reading, U.K., Tech. rep.

Gill, P. E., W. Murray, and M. H. Wright, 1981: *Practical Optimization*. Springer-Verlag, Heidelberg,.

Harrison, M. J., A. Rosati, B. J. Soden, E. Galanti, and E. Tziperman, 2002: An evaluation of air-sea flux products for enso simulation and prediction. *Monthly Weather Review*, **130**(3), 723–732.

Jin, F.-F., D. Neelin, and M. Ghil, 1994: ENSO on the devil's staircase. *Science*, **264**, 70–72.

Kalnay, E., et al., 1996: The NCEP/NCAR 40-year reanalysis project. *Bulletin of the American Meteorological Society*, **77**(3), 437–471.

Kirtman, B. P., and S. E. Zebiak, 1997: Enso simulation and prediction with a hybrid coupled model. *Monthly Weather Review*, **125**(10), 2620–2641.

Kleeman, R., A. M. Moore, and N. R. Smith, 1995: Assimilation of subsurface thermal data into an intermediate tropical coupled ocean-atmosphere model. *Mon. Weath. Rev.*, **123**, 3103–3113.

Klinker, E., F. Rabier, G. Kelly, and J. F. Mahfouf, 2000: The ECMWF operational implementation of four-dimensional variational assimilation. III: Experimental results and diagnostics with operational configuration. *Q. J. R. Meteorol. Soc.*, **126**(564), 1191–1215.

Latif, M., et al., 1998: A review of the predictability and prediction of ENSO. *J. Geophys. Res.*, **103**(C7), 14,375–14,393.

Marotzke, J., 1992: The role of integration time in determining a steady state through data assimilation. *J. Phys. Oceanogr.*, **22**, 1556.

McPhaden, M. J., et al., 1998: The tropical ocean global atmosphere observing system: A decade of progress. *J. Geophys. Res.*, **103**(C7), 14,169–14,240.

Miller, R. N., and M. A. Cane, 1989: A Kalman filter analysis of sea level heights in the Tropical Pacific. *J. Phys. Oceanogr.*, **19**, 773–790.

Moore, A. M., and R. Kleeman, 1996: The dynamics of error growth and predictability in a coupled model of ENSO. *Q. J. R. Meteor. Soc.*, **122**, 1405–1446.

Neelin, J. D., D. S. Battisti, A. C. Hirst, F.-F. Jin, Y. Wakata, T. Yamagata, and S. Zebiak, 1998: ENSO theory. *Special Joint issue of J. Geophys. Res. Atmospheres and J. Geophys. Res. Oceans*, **103**(C7), 14,261–14,290.

Pacanowski, R. C., and S. M. Griffies, 1999: *MOM 3.0 Manual*, NOAA/Geophysical Fluid Dynamics Laboratory, Princeton, NJ, USA 08542.

Pacanowski, R. C., and S. G. H. Philander, 1981: Parameterization of vertical mixing in numerical models of tropical oceans. *J. Phys. Oceanogr.*, **11**, 1443–1451.

Penland, C., and P. D. Sardeshmukh, 1995: The optimal-growth of tropical sea-surface temperature anomalies. *J. Climate*, **8**(8), 1999–2024.

Reynolds, R. W., and T. M. Smith, 1994: Improved global sea surface temperature analyses using optimum interpolation. *J. Climate*, **7**, 929–948.

Rosati, A., K. Miyakoda, and R. Gudgel, 1997: The impact of ocean initial conditions on ENSO forecasting with a coupled model. *Mon. Weath. Rev.*, **125**, 752–772.

Sirkes, Z., E. Tziperman, and C. W. Thacker, 1996: Combining data and a global primitive equation ocean general circulation model using the adjoint method. *Modern approaches to data assimilation in ocean modeling, Malanotte-Rizzoli, P. Ed., Elsevier*.

Syu, H., and J. Neelin, 2000: ENSO in a hybrid coupled model. Part I: sensitivity to physical parameterizations. *Clim. Dyn.*, **16**, 19–34.

Thacker, W. C., and R. B. Long, 1988: Fitting dynamics to data. *J. Geophys. Res.*, **93**, 1227–1240.

Tziperman, E., and W. C. Thacker, 1989: An optimal-control adjoint-equations approach to studying the oceanic general-circulation. *J. Phys. Oceanogr.*, **19**(10), 1471–1485.

Tziperman, E., W. C. Thacker, R. B. Long, and S. M. Hwang, 1992a: Oceanic data-analysis using a general-circulation model .Part 1. simulations. *J. Phys. Oceanogr.*, **22**(12), 1434–1457.

Tziperman, E., W. C. Thacker, R. B. Long, S. M. Hwang, and S. R. Rintoul, 1992b: Oceanic data-analysis using a general-circulation model .2. a North-Atlantic model. *J. Phys. Oceanogr.*, **22**(12), 1458–1485.

Tziperman, E., L. Stone, M. A. Cane, and H. Jarosh, 1994: El-nino chaos: Overlapping of resonances between the seasonal cycle and the pacific ocean-atmosphere oscillator. *Science*, **264**(5155), 72–74.

Webster, P. J., 1995: The annual cycle and the predictability of the tropical coupled ocean-atmosphere system. *Meteorol. and Atmos. Phys.*, **56**, 33–35.

Zebiak, S. E., and M. A. Cane, 1987: A model El Niño-Southern Oscillation. *Mon. Weath. Rev.*, **115**, 2262–2278.

Chapter 6:
Summary and conclusions

In this thesis I applied the adjoint method of sensitivity studies and data assimilation to a hybrid coupled model of the Indo-Pacific, in order to obtain new insights into the dynamics of ENSO, and in order to make the first steps toward developing a new 4D variational data assimilation and ENSO prediction system. In addition, a simple ENSO toy model was used to study ENSO's locking to the seasonal cycle. Using the above models I have studied El Niño's tendency to reach its peak toward the end of the year (chapter 2, Galanti and Tziperman 2000), the seasonal instability dynamics of the equatorial Pacific ocean-atmosphere system (chapter 3, Galanti et al. 2002a), and mechanisms involved in generating the decadal variability ENSO exhibits (chapter 4, Galanti and Tzipermann 2002). In addition, the predictability and prediction of ENSO was investigated within the framework of the hybrid-coupled model and the adjoint method of data assimilation (chapter 5, Galanti et al. 2002b).

The positive feedback allowing the growth of anomalous conditions in the tropical Pacific, that eventually can develop into an ENSO event, can be described as follows (Battisti 1988; Neelin et al. 1998; Suarez and Schopf 1988) (Fig. 1): a positive SST perturbation in the East Pacific excites westerly wind anomalies in the Central Pacific. These wind anomalies then excite downwelling Kelvin waves that propagate eastward. Upon reaching the East Pacific, the subsurface perturbations in the thermocline affect the sea surface temperature. The seasonality in the ocean-atmosphere coupling strength must, therefore, be due to a seasonal modulation in the effectiveness of one of the above processes. The response of the winds to SST anomalies is affected by the Inter Tropical Convergence Zone (ITCZ) location and strength and by the mean SST. The creation of oceanic thermal and dynamical signal (mainly equatorial Kelvin waves) by the winds is affected by the equatorial thermal structure as it affect the waves vertical structure and propagation speed. The connection between the sub-surface temperature anomalies and the surface SST anomalies in the East Equatorial Pacific is affected by the thermal structure and mean upwelling there. In this thesis I study the effect of the different climatological fields shown in Fig. 1 on the characteristics of ENSO, and investigate possible causes for their long term modification.

Chapter 2 (Galanti and Tziperman 2000) deals with the effect of the seasonal changes in the ITCZ location on the instability dynamics of the coupled ocean-atmosphere tropical Pacific system (Fig. 1), and its effect on the ENSO dynamics. We found that mechanism of ENSO locking to the seasonal cycle relies on the seasonal excitation of the Kelvin and the Rossby waves by wind stress anomalies in the central Pacific basin. The peak time of the events is set by the dynamics to allow a balance between the warming and cooling trends due to downwelling Kelvin and upwelling Rossby waves. This balance is obtained because the warming trend due to the large amplitude Kelvin waves, amplified by a weak boreal winter-time ocean-atmosphere coupling strength, balances the cooling trend due to weak Rossby waves, amplified by a strong boreal summer-time coupling strength. The comparison of ENSO's phase locking in the fast SST limit and in the mixed mode regime demonstrated that the adjustment time of SST to changes in thermocline depth can shift the event peak time by about two months in our idealized models. This SST adjustment time may therefore be an important part of the mechanism responsible for the phase locking of observed ENSO events.

In chapter 3 we further studied the instability dynamics, especially with regards to the seasonal variations the thermocline outcropping exhibits in the East Pacific (Fig. 1). The problem of identifying a mechanism for the seasonal changes in the tropical Pacific ocean-atmosphere instability strength was studied using the hybrid coupled model, composed of an ocean GCM coupled to a statistical atmosphere, which allows us to examine physical processes not represented in simple and intermediate models (such as the one used in chapter 2).

Most of the simple and intermediate ENSO models represent the subsurface thermal structure of the equatorial Pacific by an upper warm layer and a deeper cold layer. The interaction between the surface and subsurface is commonly assumed to be a function of the movements of the thermocline separating the two layers. More specifically, the term that affects the SST in the CZ-like models (Zebiak and Cane 1987), is the advection by the upwelling that relates changes in SST to the thermocline depth. Vertical mixing is not explicitly included but is clearly implied in this parameterization via the way the upwelling affects the SST if the thermocline nears the surface. While having the advantage of simplicity, these models do not include the seasonal movements of the

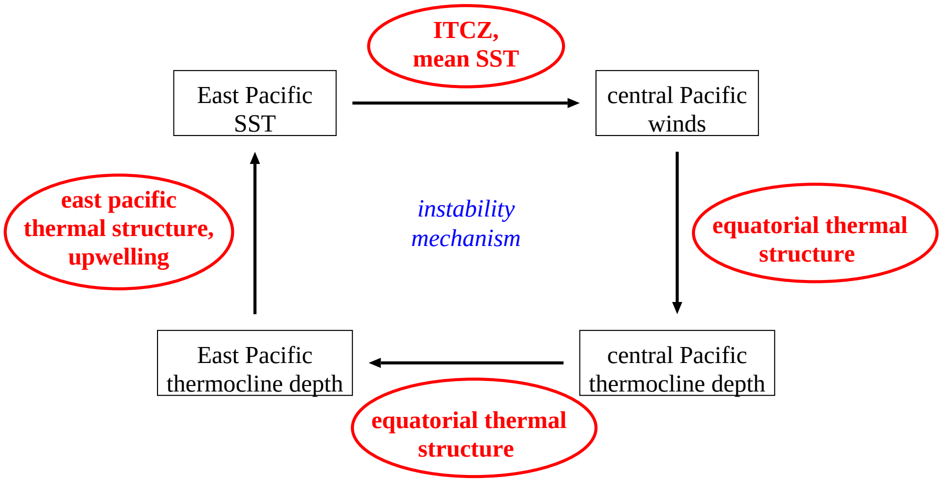

FIG. 1. A schematic figure showing the basic instability mechanism in the equatorial Pacific coupled ocean-atmosphere system. The red ovals show the different climatological fields that affect the different parts of the instability cycle. The effect of the ITCZ location of the instability cycle and ENSO's locking to the seasonal cycle is studies in chapter 2. The effect of the thermocline outcropping (East Pacific thermal structure) on the sub-surface surface connection and therefore on the instability cycle is studies in chapter 3. The causes for decadal changes in the equatorial thermal structure are studied in chapter 4.

thermocline and its outcropping, and they also lack the explicit effect of this vertical thermocline movement on the vertical mixing between the surface and the subsurface waters.

We showed that an important factor determining the strength of the coupled ocean-atmosphere instability and its seasonal variations is the strength of the East Pacific SST response to changes in the thermal structure beneath it (chapter 3, Galanti et al. 2002a). We found that the outcropping of the thermocline in the east equatorial Pacific controls the SST response to subsurface temperature anomalies. When a warm thermocline deepening signal reaches the East Pacific as downwelling Kelvin waves, its influence on the surface (SST) depends on the exposure of the thermocline at the surface; a thermocline deepening signal that arrives in late winter to spring time, when there is a strong stratification and therefore weak vertical mixing between the thermocline and the surface, will not affect the vertical mixing and will therefore not affect the SST. On the other hand, a warm thermocline deepening signal that arrives in fall and early winter, when the thermocline is then exposed to the surface, the stratification is weak and vertical mixing between the thermocline and the surface is strong, will be able to weaken the mixing between the cold subsurface water and the surface water, and induce an SST warming. The seasonal ocean-atmosphere coupling strength is therefore influenced by the seasonal changes in the East pacific thermocline outcropping.

The modulation of the subsurface to surface connection by the seasonal changes in the thermocline outcropping is relevant also to the effect of vertical thermocline movements through the ENSO cycle. Our discussion of the role of thermocline outcropping and vertical mixing may therefore also be relevant to the analysis of (Van-Oldenborgh et al. 1999) which found changes in ENSO's sensitivity during different phases of the ENSO cycle.

Neelin et al. (2000) showed that changing the mixed layer parameterization in their model, shifted the peak of the model ENSO events by a few months, although they could not explain this in terms of a specific physical mechanism. Galanti and Tziperman (2000) (chapter 2) presented a mechanism that is based on the seasonal variations of the ocean-atmosphere instability strength that affects the amplification of ocean waves. This study shows that the coupled instability strength and its seasonal variations are strongly affected by the mixed layer processes through the thermocline outcropping dynamics. We therefore suggest here that the mixed layer parameterization affects the coupled instability strength and its seasonal variations (via the thermocline outcropping mechanism). Therefore the mixed layer parameterization affects the seasonal amplification of ocean waves, and may influence the phase locking of ENSO as observed by Neelin et al. (2000), based on the dynamical explanations of Tziperman et al. (1998) and Galanti and Tziperman (2000) (chapter 2).

ENSO's decadal variability is characterizes by changes in the frequency and strength of the events on a decadal time scale. The causes for ENSO decadal variability are believed to be changes in the mean state of the equatorial thermal structure and accompanying tropical winds that affect the ocean-atmosphere instability strength (chapter 3, Galanti et al. 2002a; Gu and Philander 1997). In chapter 4 we studied the possible causes for a decadal change in the equatorial thermal structure. A specific novel mechanism for an ocean wave teleconnection between the mid-latitude Pacific and the equator was proposed (chapter 4, Galanti and Tzipermann 2002). According to this mechanism, baroclinically unstable areas of the sub-tropical gyre amplify waves passing via these areas. As a result, these amplified waves dominate the mid-latitude signal at the equator. To do this analysis we have used the adjoint method of sensitivity analysis, as well as a quasi-geostrophic normal mode stability analysis. The comparison between the results of these two tools was especially useful in demonstrating the role of baroclinic instability in amplifying the sensitivity signal arriving at the equator from the mid-latitudes. We demonstrated that critical layers due to the vertical shear of the sub-tropical gyre circulation in the baroclinically unstable areas play an important role in shaping the instability characteristics, and the structure of the sensitivity signal seen in the adjoint model results.

Upon arrival to the equator, the mid-latitude planetary waves can alter the stratification along the equator, and thus create a decadal variability due to decadal-scale signals arriving from mid-latitudes. We did not deal with the question of what generates the mid-latitude decadal signal, and many possibilities have been proposed in the literature (e.g. Gu and Philander 1997; Latif and Barnett 1994).

Our sensitivity analysis tool could in principle indicate also that the equatorial Pacific is sensitive to advection of mid-latitude water, but showed a preferred ocean wave teleconnection. We verified that the sensitivity signal is our model is indeed due to waves by calculating dynamic (due to wave motion that moves the isopycnals) vs kinematic (due to long-isopycnal advection) sensitivities (Marotzke et al. 1999). We also conducted an idealized model run to demonstrate that in the absence of baroclinically unstable regions it is difficult for mid-latitude waves to efficiently affect the equatorial Pacific.

It is obviously possible that some specific characteristics of our results are affected by the particular model used here. For example, the location and extent of the baroclinically unstable mid-latitude regions could be different had we used a different viscosity. Similarly, advection might have been more dominant in a higher resolution model. However, we feel that the basic message here, of a wave teleconnection involving amplification by baroclinic instability, should hopefully be a robust result.

In additions to the above studies that focused on the dynamics of the tropical Pacific ocean-atmosphere coupled system, we also investigated an experimental ENSO prediction system based on an ocean GCM coupled to a statistical atmosphere, and the adjoint method of 4D variational data assimilation (chapter 5, Galanti et al. 2002b). The coupled model is initialized using the adjoint method in order to perform predictions from 1980 to 1999. In order to compare the prediction skill of the system, two simpler assimilation techniques were also used to initialize the coupled model: forcing the ocean model with observed SST, wind stress and surface fluxes, and the 3D variational assimilation method of Rosati et al. (1997). In addition, we examined the issue of the period over which the adjoint assimilation is to be conducted by initializing the model with assimilation periods of 3, 6 and 9 months and comparing the resulting prediction skill. Another issue examined here is the assimilation of the full observed fields vs. the assimilation of the anomalous (with respect to model and observed monthly climatologies) fields.

A comparison between the skill of the coupled model when initialized with the adjoint method, and the skill of the coupled model initialized using a forced ocean model and the 3Dvar assimilation method, shows that the adjoint method does seem to have the potential of improving simpler assimilation schemes. The improved skill is mainly at prediction intervals of more than 6 months, where the coupled model dynamics start to influence the model solution. At shorter prediction time intervals, the initialization using the forced ocean model or the 3Dvar assimilation may result in a better prediction skill. This occurs because both simpler assimilation methods calculate initial conditions that are closer to the observed temperature at the beginning of the prediction period, while the adjoint method allows the initial conditions to deviate further away from the observations, based on the model dynamics. In the first few months of the prediction, the initial conditions dominate the prediction skill and therefore the simpler methods do better. It is also important to note that substantial discrepancies exist between our results for the 3Dvar initialization and those of Rosati et al. (1997) who used a higher resolution ocean model and an atmospheric GCM. This raises important questions regarding the effects of model resolution and atmospheric model used on the performance of the different assimilation schemes considered here, which will need to be addressed in a future studies.

A detailed analysis of ENSO prediction experiments for the 1997-8 event, for which the adjoint method seems to performed somewhat better than the other two schemes considered here, strengthens the above conclusion regarding the potential of the adjoint method.

We explained that defining the cost function to be the difference between the observed and model anomalous fields (with respect to the model and observed climatologies, and instead of using the full fields) may eliminate the effects of systematic model bias and therefore improve predictability skill. In our experiments here, however, the assimilation of anomalies did not have a substantial effect on the prediction skill of the coupled model. This seems to indicate that in our model the bias due to the model climatology, which is corrected by the anomaly assimilation, is less significant than the bias in the model variability which cannot be eliminated using the anomaly assimilation.

Changing the optimization period from 6 months to 3 months and to 9 months showed that the period of 6 months seems to be a near optimal choice for our model. Shortening the optimization period to 3 months resulted in a better skill at short prediction times (up to 6 months), but reduced the skill at longer prediction times. Increasing the optimization interval to 9 months resulted in a reduced skill in all time intervals. Lacking a sufficient theoretical understanding of what sets ENSO's predictability limit, and therefore of the issue of optimal assimilation time, we cannot judge how robust these results are to model details and resolution.

All aspects of initialization and prediction studied here clearly need to be further investigated using higher resolution models in order to optimize the use of the adjoint method for ENSO prediction. This is especially relevant in view of the discrepancies between our results for the 3Dvar initialization and those of Rosati et al. (1997). Nevertheless, we feel that it is reasonable to hope that the adjoint method may out perform other assimilation schemes at higher ocean resolutions, as it did at the coarse resolution used here. The results here therefore seem sufficiently encouraging to justify a further study.

REFERENCES

Battisti, D. S., 1988: The dynamics and thermodynamics of a warming event in a coupled tropical atmosphere/ocean model. *J. Atmos. Sci.*, **45**, 2889–2919.

Galanti, E., and E. Tziperman, 2000: ENSO's phase locking to the seasonal cycle in the fast sst, fast wave, and mixed mode regimes. *J. Atmos. Sci.*, **57**, 2936–2950.

Galanti, E., and E. Tzipermann, 2002: A mid-latitude enso teleconnection mechanism via long rossby waves. *J. Phys. Oceanogr.*. Submitted.

Galanti, E., E. Tziperman, M. Harrison, A. Rosati, R. Giering, and Z. Sirkes, 2002a: The equatorial thermocline outcropping - a seasonal control on the tropical Pacific ocean-atmosphere instability strength. *J. Climate*, **15**(19), 2721–2739.

Galanti, E., E. Tziperman, M. Harrison, A. Rosati, and Z. Sirkes, 2002b: A study of enso prediction using a hybrid-coupled model and the adjoint method for data assimilation. *Mon. Weath. Rev.*. Submitted.

Gu, D., and S. G. H. Philander, 1997: Interdecadal climate fluctuations that depend on exchanges between the tropics and extratropics. *Science*, **275**(7), 805–807.

Latif, M., and T. P. Barnett, 1994: Causes of decadal climate variability over the North Pacific and North-America. *Science*, **266**, 634–637.

Marotzke, J., R. Giering, K. Q. Zhang, D. Stammer, C. Hill, and T. Lee, 1999: Construction of the adjoint mit ocean general circulation model and application to Atlantic heat transport sensitivity. *J. Geophys. Res.*, **104**(C12), 29,529–29,547.

Neelin, J., F. Jin, and H. Syu, 2000: Variations in ENSO phase locking. *J. Climate*, **13**(14), 2570–2590.

Neelin, J. D., D. S. Battisti, A. C. Hirst, F.-F. Jin, Y. Wakata, T. Yamagata, and S. Zebiak, 1998: ENSO theory. *Special Joint issue of J. Geophys. Res. Atmospheres and J. Geophys. Res. Oceans*, **103**(C7), 14,261–14,290.

Rosati, A., K. Miyakoda, and R. Gudgel, 1997: The impact of ocean initial conditions on ENSO forecasting with a coupled model. *Mon. Weath. Rev.*, **125**, 752–772.

Suarez, M. J., and P. S. Schopf, 1988: A delayed action oscillator for ENSO. *J. Atmos. Sci.*, **45**, 3283–7.

Tziperman, E., M. A. Cane, S. E. Zebiak, Y. Xue, and B. Blumenthal, 1998: Locking of El Nino's peak time to the end of the calendar year in the delayed oscillator picture of ENSO. *J. Climate*, **11**(9), 2191–2199.

Van-Oldenborgh, G. J., G. Burgers, S. Venzke, C. Eckert, and R. Giering, 1999: Tracking down the ENSO delayed oscillator with an adjoint ogcm. *Mon. Weath. Rev.*, **127**(7), 1477–1495.

Zebiak, S. E., and M. A. Cane, 1987: A model El Niño-Southern Oscillation. *Mon. Weath. Rev.*, **115**, 2262–2278.

Note on personal contribution to papers

This thesis for the degree of Ph.D. summarizes my research efforts under the supervision of Prof. Eli Tziperman. I have been the major contributor to all manuscripts composing this thesis. Interaction and consultation with Eli in all of these works was on a regular basis.